

#### POLITECNICO DI TORINO

Master's Degree course in Automotive Engineering

Master Degree Thesis

# 0D/1D simulation of a heavy-duty engine fuelled with methane-hydrogen mixtures

Supervisor

Candidate

**Prof. Daniela Anna Misul** 

**Andrea Soffietto** 

mat.329755

Co-supervisors

Dr. Eng. Dario Di Maio

Academic year 2024/2025

#### Acknowledgements

Reaching the end of my academic journey, I would like to express my gratitude to all those who, in different ways, have contributed both to the realisation of this thesis and to my personal and professional growth.

I would like to thank my supervisor, Prof. Daniela Anna Misul, for trusting me and for giving me the opportunity to work on such an interesting thesis project. I also wish to thank my co-supervisor at CNR-STEMS, Eng. Dario Di Maio, for his constant support and guidance throughout this work.

To my family, for always believing in me, for their unconditional support, and for instilling in me the values that have guided me along this journey. Without their love, patience, and encouragement, none of this would have been possible.

To my friends, who have been a fundamental presence throughout these years. Thank you for the carefree moments, the laughter, and the support during the most demanding times. Your friendship has been a precious refuge and has reminded me of the importance of having sincere people by my side with whom I can share both joys and challenges.

To Roberta, whose love, patience, and constant encouragement have made this journey much lighter and brighter.

#### **Abstract**

Climate change is an issue that can no longer be overlooked, representing one of the most critical emergencies of our time, due to the higher amount of greenhouse gas (GHG) emissions. The transportation sector has a significant role in the production of GHG. New legislations require a reduction of greenhouse gas and pollutant emissions. Therefore, internal combustion engines must face challenges but also opportunities for innovation, especially through the adoption of alternative low-carbon fuels.

Methane is considered one of the most promising fuels for heavy-duty engines, due to its high octane number and higher thermal efficiency compared to gasoline. However, the sole adoption of methane is not sufficient to be compliant with the more stringent regulations. Hydrogen, on the other hand, is a carbon-free energy carrier capable of reducing GHG emissions. Blending hydrogen with methane is considered a promising transitional strategy. However, hydrogen enrichment introduces challenges related to abnormal combustion phenomena and higher NOx formation. This trade-off highlights the importance of an accurate simulation capable of reproducing the effect of the blend on engine performance, emissions, and combustion stability.

This thesis aims to analyse the potential benefits of adding hydrogen to a six-cylinder heavy-duty compressed natural gas SI engine. Two hydrogen blending ratios are evaluated, specifically 15% and 25%. 0D–1D numerical models were validated and optimised within the GT-Suite simulation environment. The activity has been carried out in collaboration with the Institute of Science and Technologies for Sustainable Energy and Mobility (STEMS) of the Italian National Research Council in Naples. The study is structured into two main parts: steady-state analysis and transient analysis.

In the first part, four representative engine operating points from the engine workplan were analysed. Starting from a complete six-cylinder engine model, an equivalent monocylinder model was created to simplify the analysis without losing information. A calibration and validation process was carried out to ensure validity. Subsequently, two approaches to handling the combustion were investigated: the Three Pressure Analysis (TPA) and the SI-TURB model. The TPA method estimates the apparent burn rate from intake, in-cylinder, and exhaust pressure data. The SI-TURB model, on the other hand, is a predictive approach based on turbulence and flame propagation that requires an extensive calibration through sensitivity analyses and optimisation campaigns. After validation with methane, hydrogen was inserted into the model. For this purpose, the injector system was modelled to account for both methane and hydrogen injection.

Knock tendency was also investigated through a dedicated analysis aimed at identifying the conditions under which this abnormal combustion phenomenon occurs. Specifically, variations in compression ratio, intake pressure, and spark advance were analysed.

In transient conditions, the model was run in a specified portion of the World Harmonised Transient Cycle (WHTC) to validate it under realistic driving conditions. Two modelling strategies were compared. The first employed a single representative operating point as the combustion object for the entire engine model, corresponding to the most frequent condition in that cycle segment. The second analysis was carried out using a Look-Up Table (LUT) as the combustion object, which incorporated the data obtained from the four operating points investigated in the steady-state analysis.

### **Contents**

1	Intr	oduction	9
	1.1	Greenhouse gases and pollutants	9
	1.2	Transportation sector and regulatory framework	13
	1.3	Methane as a fuel	18
	1.4	Hydrogen as a fuel	18
	1.5	Hydrogen–methane blends	19
	1.6	GT-SUITE description	19
	1.7	Research objectives	20
2	Stea	dy-state analysis	21
	2.1	Engine model description	21
	2.2	Feasibility study	24
	2.3	Burn rate determination from Measured Cylinder Pressure	29
		2.3.1 Injector change	30
		2.3.2 Three Pressure Analysis (TPA)	30
	2.4	Development of the predictive SI-TURB combustion model	36
		2.4.1 Sensitivity analysis of SI-TURB parameters	39
		2.4.2 SI-TURB model optimisation	43
	2.5	Hydrogen addition strategies	54
		2.5.1 Burn rate evaluation for HCNG mixtures with TPA analysis	60
		2.5.2 Predictive modelling of HCNG combustion with SI-TURB model	65
		2.5.3 Engine emissions comparison	70
		2.5.4 Effect of spark advance on combustion	74
	2.6	Knock analysis	78
3	Trai	nsient analysis	88
	3.1	WHTC description and model setup	88
	3.2	Methodology description and results	90
		3.2.1 Single operating point combustion modelling approach	91
		3.2.2 Look-Up Table (LUT) combustion modelling approach	94

4	Conclusions																		99
Bi	bliography																		101
A	Knock analy	sis																	104
	A.1																		105
	A.2																		106
	A.3																		108
	Λ 1																		112

### **List of Figures**

1.1	Principal GHGs [1]	9
1.2	GHGs emitters [3]	10
1.3	Tools necessary for the transformation of the EU's economy envisaged by	
	the European green deal [5]	11
1.4	Sectors and activities contributing to emissions of the five regulated air	
	pollutants in EU in 2023 [6]	12
1.5	Trend in EU emissions between 2005 and 2023 [6]	13
1.6	GHGs in EU by sector in 2022, expressed in CO <sub>2</sub> equivalent [3]	13
1.7	CO <sub>2</sub> emissions reduction in transport in the NZE scenario [7]	14
1.8	Present and future energy sources for transportation in NZE scenario [7] .	15
1.9	Present and future energy sources divided in the sector of utilisation in	
	NZE scenario [7]	16
1.10	Euro 7 tailpipe emission limit for heavy-duty vehicles of categories N2,	
	N3, M2 and M3 [9]	17
2.1	Baseline six-cylinder engine model	22
2.2	Mono-cylinder engine model	24
2.3	Map of selected engine operating points	25
2.4	CNG In-cylinder pressure – Wiebe combustion model (C1)	27
2.5	CNG In-cylinder pressure – Wiebe combustion model (C2)	27
2.6	CNG In-cylinder pressure – Wiebe combustion model (C3)	28
2.7	CNG In-cylinder pressure – Wiebe combustion model (C4)	28
2.8	CNG In-cylinder pressure - TPA combustion model (C1)	32
2.9	CNG In-cylinder pressure - TPA combustion model (C2)	32
2.10	CNG In-cylinder pressure - TPA combustion model (C3)	33
2.11	CNG In-cylinder pressure - TPA combustion model (C4)	33
2.12	CNG Burn rate - TPA combustion model (C1)	34
2.13	CNG Burn rate - TPA combustion model (C2)	34
2.14	CNG Burn rate - TPA combustion model (C3)	35
2.15	CNG Burn rate - TPA combustion model (C4)	35
2.16	CFD turbulence profiles (C1)	37
2.17	CNG In-cylinder pressure - SI-TURB combustion model - DEM sweep	40

2.18	CNG Burn rate - SI-TURB combustion model - DEM sweep	40
2.19	CNG In-cylinder pressure - SI-TURB combustion model - $C_k$ sweep	41
2.20	CNG Burn rate - SI-TURB combustion model - $C_k$ sweep	41
2.21	CNG In-cylinder pressure - SI-TURB combustion model - $C_s$ sweep	42
2.22	CNG Burn rate - SI-TURB combustion model - $C_s$ sweep	42
2.23	CNG In-cylinder pressure - SI-TURB combustion model - $C_{\lambda}$ sweep	43
2.24	CNG Burn rate - SI-TURB combustion model - $C_{\lambda}$ sweep	43
2.25	DOE analysis setup - SI-TURB combustion model	44
2.26	Advanced optimiser setup - SI-TURB combustion model	45
2.27	CNG In-cylinder pressure - Global SI-TURB combustion model (C1) $$ . $$ .	45
2.28	CNG Burn rate – Global SI-TURB combustion model (C1)	46
2.29	CNG In-cylinder pressure – Global SI-TURB combustion model (C2) $$ . $$	46
2.30	CNG Burn rate - Global SI-TURB combustion model (C2)	47
2.31	CNG In-cylinder pressure - Global SI-TURB combustion model (C3)	47
2.32	CNG Burn rate - Global SI-TURB combustion model (C3)	48
2.33	CNG In-cylinder pressure - Global SI-TURB combustion model (C4) $$ . $$ .	48
2.34	CNG Burn rate - Global SI-TURB combustion model (C4)	49
2.35	CNG In-cylinder pressure - Single case SI-TURB combustion model (C1)	50
2.36	CNG Burn rate - Single case SI-TURB combustion model (C1)	50
2.37	CNG In-cylinder pressure - Single case SI-TURB combustion model (C2)	51
2.38	CNG Burn rate - Single case SI-TURB combustion model (C2)	51
2.39	CNG In-cylinder pressure - Single case SI-TURB combustion model (C3)	52
2.40	CNG Burn rate - Single case SI-TURB combustion model (C3)	52
2.41	CNG In-cylinder pressure - Single case SI-TURB combustion model (C4)	53
2.42	CNG Burn rate - Single case SI-TURB combustion model (C4)	53
2.43	Mono-cylinder engine model with $H_2$ injector inserted $\ldots \ldots \ldots$	55
2.44	HCNG In-cylinder pressure - Wiebe combustion model (C1)	57
2.45	HCNG In-cylinder pressure - Wiebe combustion model (C2)	58
2.46	HCNG In-cylinder pressure - Wiebe combustion model (C3)	58
2.47	HCNG In-cylinder pressure - Wiebe combustion model (C4)	59
2.48	HCNG In-cylinder pressure - TPA combustion model (C1)	61
2.49	HCNG Burn rate - TPA combustion model (C1)	61
2.50	HCNG In-cylinder pressure - TPA combustion model (C2)	62
2.51	HCNG Burn rate - TPA combustion model (C2)	62
2.52	HCNG In-cylinder pressure - TPA combustion model (C3)	63
2.53	HCNG Burn rate - TPA combustion model (C3)	63
2.54	HCNG In-cylinder pressure - TPA combustion model (C4)	64
2.55	HCNG Burn rate - TPA combustion model (C4)	64
2.56	HCNG In-cylinder pressure - SI-TURB combustion model (C1)	66

2.57	HCNG Burn rate - SI-TURB combustion model (C1)	66
2.58	HCNG In-cylinder pressure - SI-TURB combustion model (C2)	67
2.59	HCNG Burn rate - SI-TURB combustion model (C2)	67
2.60	HCNG In-cylinder pressure - SI-TURB combustion model (C3)	68
2.61	HCNG Burn rate - SI-TURB combustion model (C3)	68
2.62	HCNG In-cylinder pressure - SI-TURB combustion model (C4)	69
2.63	HCNG Burn rate - SI-TURB combustion model (C4)	69
2.64	CO <sub>2</sub> normalised emissions comparison	71
2.65	CO normalised emissions comparison	71
2.66	$NO_x$ normalised emissions comparison	72
2.67	NO normalised emissions comparison	72
2.68	HC (No C basis) normalised emissions comparison	73
2.69	HC (C1 basis) normalised emissions comparison	73
2.70	HCNG15 Burn rate - Spark Advance sweep (C1)	74
2.71	HCNG15 Burn rate - Spark Advance sweep (C2)	75
2.72	HCNG15 Burn rate - Spark Advance sweep (C3)	75
2.73	HCNG15 Burn rate - Spark Advance sweep (C4)	76
2.74	HCNG15 In-cylinder pressure - Spark Advance sweep (C1)	76
2.75	HCNG15 In-cylinder pressure - Spark Advance sweep (C2)	77
2.76	HCNG15 In-cylinder pressure - Spark Advance sweep (C3)	77
2.77	HCNG15 In-cylinder pressure - Spark Advance sweep (C4)	78
3.1	WHTC speed and load profiles [20]	88
3.2	Six-cylinder engine model controller implementation	89
3.3	WHTC most frequent engine operating points: 1300 rpm – 150 Nm (0–900	
	s) and 1700 rpm – 310 Nm (900–1800 s)	91
3.4	WHTC interval of the most frequent engine operating point	92
3.5	arphi profile for the throttle controller $$	92
3.6	WHTC brake torque profiles - Single operating point combustion model	
	(C2)	93
3.7	WHTC fuel flow rate profiles - Single operating point combustion model	
	(C2)	93
3.8	WHTC Lambda profiles - Single operating point combustion model (C2) .	94
3.9	WHTC brake torque profiles - LUT with TPA combustion model	95
3.10	WHTC fuel flow rate profiles - LUT with TPA combustion model	95
3.11	WHTC lambda profiles - LUT with TPA combustion model	96
3.12	WHTC brake torque profiles - LUT with SI-TURB combustion model	96
3.13	WHTC fuel flow rate profiles - LUT with SI-TURB combustion model	97
3.14	WHTC lambda profiles - LUT with SI-TURB combustion model	97

### **List of Tables**

2.1	Engine specifications	21
2.2	CNG engine performance parameters – Wiebe combustion model	25
2.3	Effective $\lambda$ at EVO changing the CNG injector	30
2.4	CNG engine performance parameters - TPA combustion model	31
2.5	SI-TURB multiplier values global optimisation	49
2.6	SI-TURB multiplier values single case optimisation	50
2.7	CNG engine performance parameters - Single case SI-TURB combustion	
	model	54
2.8	HCNG15 injected masses	55
2.9	HCNG25 injected masses	55
2.10	HCNG $\lambda$ values with Wiebe combustion model	56
2.11	HCNG Intake pressure increase - Wiebe combustion model	57
2.12	HCNG15 engine performance parameters - Wiebe combustion model	60
2.13	HCNG25 engine performance parameters - Wiebe combustion model	60
2.14	HCNG15 engine performance parameters - TPA combustion model	65
2.15	HCNG25 engine performance parameters - TPA combustion model	65
2.16	HCNG15 engine performance parameters - SI-TURB combustion model .	70
2.17	HCNG25 engine performance parameters - SI-TURB combustion model .	70
2.18	Crank Angle at Knock Onset and Knock Probability - KNG knock model	
	- CR sweep (C3)	81
2.19	Brake Efficiency - KNG knock model - CR sweep (C3)	81
2.20	Crank Angle at Knock Onset and Knock Probability - KNG knock model	
	- SA sweep (C3)	82
2.21	Crank Angle at Knock Onset and Knock Probability - KH knock model -	
	CR sweep (C3)	83
2.22	Brake Efficiency - KNG knock model - SA sweep (C3)	83
2.23	Crank Angle at Knock Onset and Knock Probability - KNG knock model	
	- Intake Pressure sweep (C3)	84
2.24	Crank Angle at Knock Onset and Knock Probability - KH knock model -	
	Intake Pressure sweep (C3)	85
2.25	Brake Efficiency - KNG knock model - Intake Pressure sweep (C3)	85

2.26 HCNG25 Crank Angle at Knock Onset and Knock Probability - KNG knock model - Intake Pressure and SA sweep (C3)	86
3.1 CNG engine performance parameters - TPA combustion model - Six-	0.0
cylinder engine model	90
A.1.1 Crank Angle at Knock Onset and Knock Probability - KNG knock model	
- CR sweep (C5)	105
A.1.2Brake Efficiency - KNG knock model - CR sweep (C5)	105
A.2.1 Crank Angle at Knock Onset and Knock Probability - KNG knock model	
- SA sweep (C3)	106
A.2.2Crank Angle at Knock Onset and Knock Probability - KH knock model -	
SA sweep (C3)	106
A.2.3Brake Efficiency - KNG knock model - SA sweep (C3)	107
A.3.1 Crank Angle at Knock Onset and Knock Probability - KNG knock model	
- Intake Pressure sweep (C5)	108
A.3.2Crank Angle at Knock Onset and Knock Probability - KH knock model -	
Intake Pressure sweep (C5)	108
$A.3.3  Brake  Efficiency  \hbox{-}  KNG  knock  model  \hbox{-}  Intake  Pressure  sweep  (C5)  .   .   .$	109
A.3.4Crank Angle at Knock Onset and Knock Probability - KNG knock model	
- Intake Pressure sweep with CR=11.5 (C3)	109
A.3.5 Crank Angle at Knock Onset and Knock Probability - KH knock model -	
Intake Pressure sweep with CR=11.5 (C3)	110
A.3.6Brake Efficiency - KNG knock model - Intake Pressure sweep with CR=11.5	
(C3)	110
A.3.7Crank Angle at Knock Onset and Knock Probability - KNG knock model	
- Intake Pressure sweep with CR=11.5 (C5)	111
A.3.8Crank Angle at Knock Onset and Knock Probability - KH knock model -	
Intake Pressure sweep with CR=11.5 (C5)	111
A.3.9Brake Efficiency - KNG knock model - Intake Pressure sweep with CR=11.5	
(C5)	112
A.4.1HCNG15 Crank Angle at Knock Onset and Knock Probability - KNG	
knock model - Intake Pressure and SA sweep with CR=11.5 (C3)	113
A.4.2HCNG25 Crank Angle at Knock Onset and Knock Probability - KNG	
knock model - Intake Pressure and SA sweep with CR=11.5 (C5)	113
A.4.3HCNG15 Crank Angle at Knock Onset and Knock Probability - KNG	
knock model - Intake Pressure and SA sweep with CR=11.5 (C5)	114
A.4.4HCNG25 Crank Angle at Knock Onset and Knock Probability - KH knock	
model - Intake Pressure and SA sweep with CR=11.5 (C3)	114

A.4.5 HCNG15 Crank Angle at Knock Onset and Knock Probability - KH knock
model - Intake Pressure and SA sweep with CR=11.5 (C3) 115
A.4.6HCNG25 Crank Angle at Knock Onset and Knock Probability - KH knock
model - Intake Pressure and SA sweep with CR=11.5 (C5) 115
A.4.7HCNG15 Crank Angle at Knock Onset and Knock Probability - KH knock
model - Intake Pressure and SA sweep with CR=11.5 (C5) 116

### Chapter 1

#### Introduction

#### 1.1 Greenhouse gases and pollutants

Climate change is an issue that can no longer be overlooked, representing one of the most critical and pressing global emergencies of our time. This phenomenon is evidenced by the increase in average global temperature, the accelerated melting of glaciers and the higher frequency and intensity of extreme and unpredictable meteorological events. Climate change has caused many damages and increasingly irreversible losses in ecosystems. According to the Sixth Report of the Intergovernmental Panel on Climate Change (IPCC AR6, 2021), the principal responsible of these changes is human activity, which has significantly increased the concentration of greenhouse gases (GHGs) in the atmosphere.

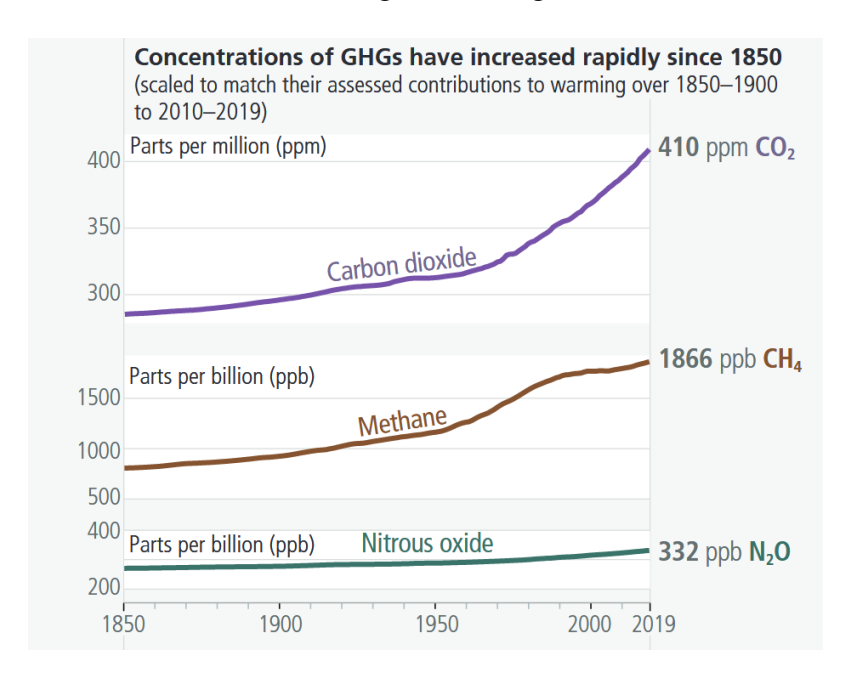


Figure 1.1: Principal GHGs [1]

As the Figure 1.1 shows, the most relevant GHGs are carbon dioxide  $(CO_2)$ , which has the dominant contribution, followed by methane  $(CH_4)$  and nitrous dioxide  $(N_2O)$ . As a direct

consequence of increasing GHG concentrations, the global average surface temperature in 2020 was 1.1°C higher compared to the late 19th century, with the highest increase occurring in the last two decades, particularly between 2012 and 2016 [1]. The increase of temperature is not uniform all over the Earth, with a pronounced increase on land compared to the oceans.

Greenhouse gases are naturally occurring atmospheric components that absorb and emit infrared radiations, thereby trapping heat within the atmosphere and maintaining temperatures suitable for life. However, the increase in their concentration reduces the amount of infrared radiations that can escape from the atmosphere, increasing the heat retained and consequently the temperature. Each greenhouse gas differs in its radiative efficiency (the amount of heat it can trap) and its atmospheric lifetime, which are quantified using the Global Warming Potential (GWP). It represents the amount of heat trapped by a given mass of gas relative to the same mass of carbon dioxide, over a standardised time, typically 100 years. By definition, the GWP of the (CO<sub>2</sub>) is equal to 1, while for the (CH<sub>4</sub>) it is of 21 and for the (N<sub>2</sub>O) it is 210. This implies that, per unit of mass, nitrous oxide has a warming effect 210 times greater than carbon dioxide, and methane has an effect 21 times greater.

In 2023, the carbon dioxide (CO<sub>2</sub>) emissions exceeded 36.8 gigatons [2]. In this context, as shown in Figure 1.2, the European Union ranks as the fourth largest greenhouse gas emitter globally, accounting for over 7% of the total emissions.

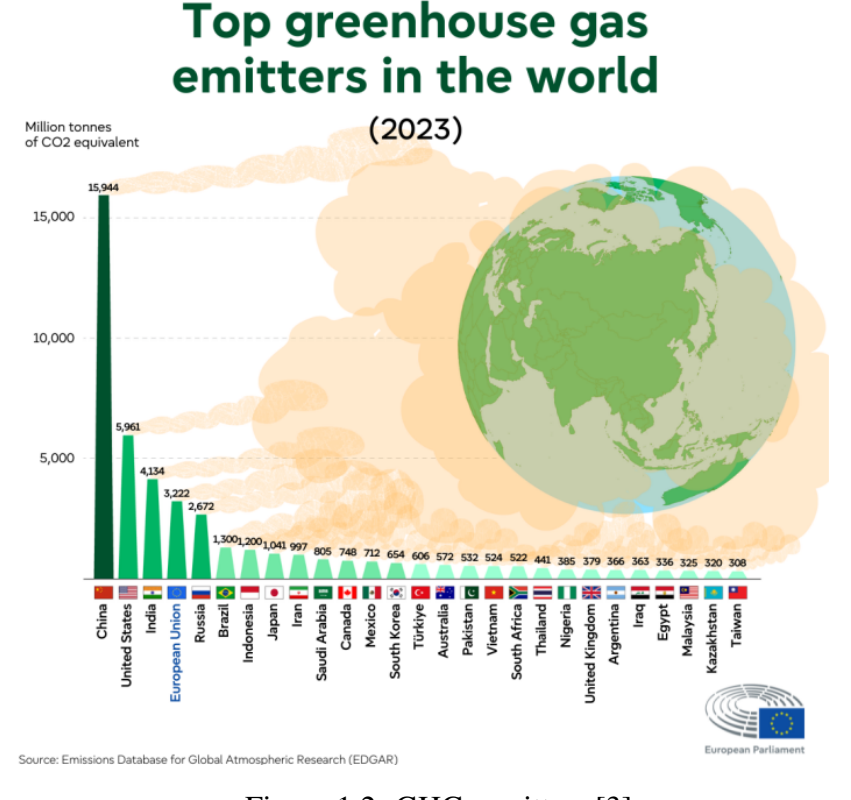


Figure 1.2: GHGs emitters [3]

In 2015, the Paris Agreement was signed to limit the global temperature increase to 1.5°C above pre-industrial levels. This target is crucial because the Intergovernmental Panel on Climate Change (IPCC) has indicated that exceeding the 1.5 °C threshold would increase the risk of severe climate changes, such as severe droughts, heatwaves and rainfall [4]. Considering the previous percentage, the EU has a relatively limited impact on total global emissions. Nevertheless, it has assumed a leading role at the international level in promoting sustainability and pursuing carbon neutrality objectives. To address this challenge, in 2019, the European Commission launched the European Green Deal to improve people's well-being while making Europe the first climate-neutral continent in the world and protecting the natural ecosystems. Figure 1.3 shows the tools necessary to achieve this goal.

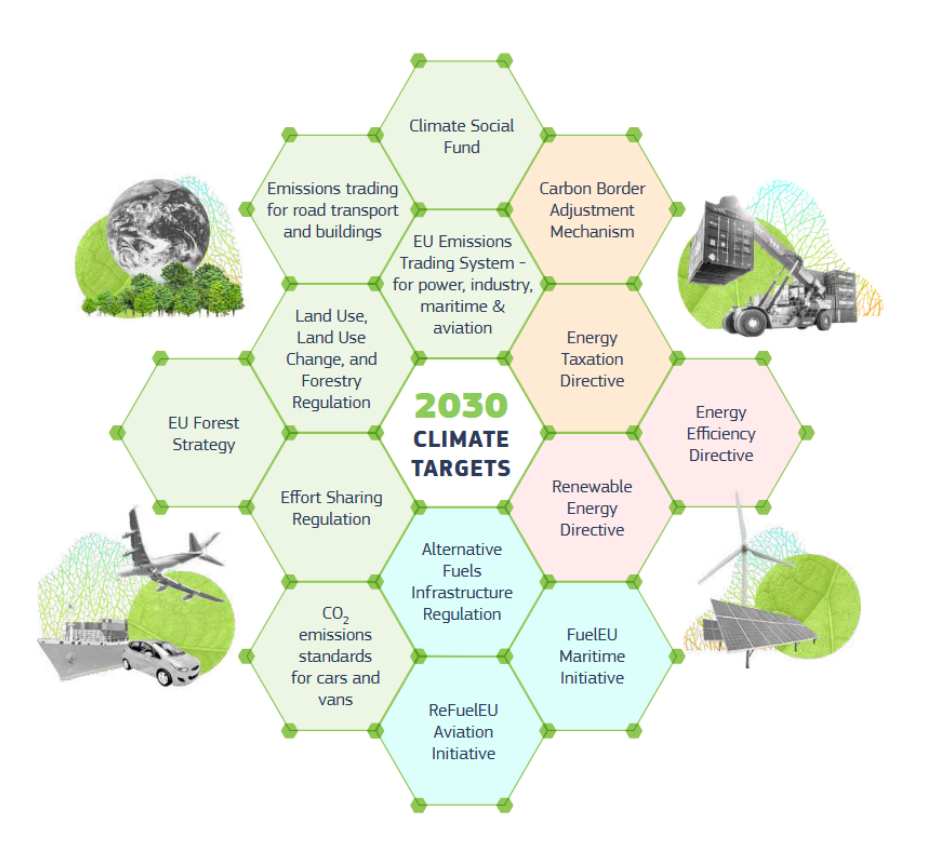


Figure 1.3: Tools necessary for the transformation of the EU's economy envisaged by the European green deal [5]

This plan is articulated in several initiatives, including the Fit for 55 package, which sets an intermediate target of reducing net greenhouse gas emissions by 55% by 2030 compared to the 1990 levels.

Beyond greenhouse gases, environmental pollutants represent another category of substances harmful to both the environment and human health. Unlike GHGs, air pollutants have a direct impact on air quality, public health and local ecosystems. These substances can originate from natural sources, such as volcanic activities or forest fires, as well as from anthropogenic activities including energy production, transportation, agriculture and industrial processes.

The pollutants are generally classified into two principal categories:

- Primary pollutant: These are directly emitted into the atmosphere. Examples include particulate matter (PM), nitrogen oxides (NO<sub>x</sub>), sulfur dioxide (SO<sub>2</sub>), ammonia (NH<sub>3</sub>), carbon monoxide (CO) and non-methane organic volatile components (NMVOCs).
- Secondary pollutants: These are not directly emitted, but they originate in the atmosphere through chemical reactions between primary pollutants. An example is the ozone (O<sub>3</sub>).

As shown in Figure 1.4, the sources of different pollutants vary depending on the species, but they share the characteristic that they originate from human activity.

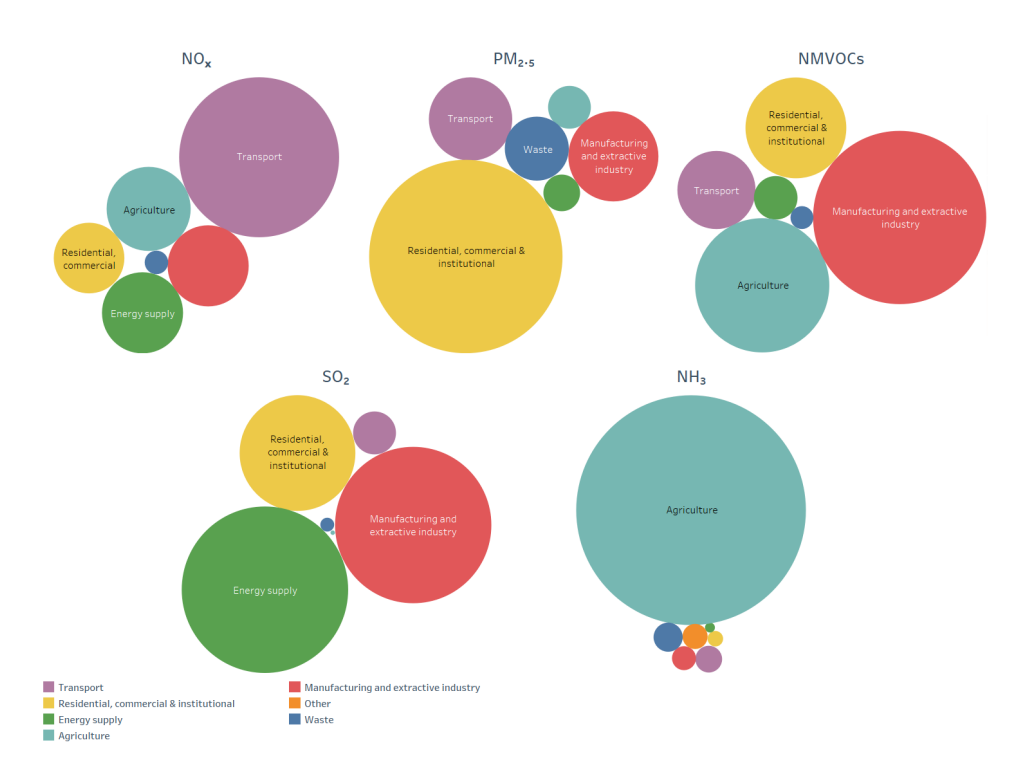


Figure 1.4: Sectors and activities contributing to emissions of the five regulated air pollutants in EU in 2023 [6]

There was a slight decline in the total number of air pollutant emissions in Europe in 2023, maintaining the downward trend observed since 2005, as depicted in Figure 1.5. The percentages displayed in the graph refer to their value compared to the 2005 ones. This demonstrates the absolute decoupling of emissions from economic activity between 2005 and 2023. This indicates that air pollutant emissions are decreasing or remain almost stable while the Gross Domestic Product (GDP)increases. The greatest decoupling is observed for the sulfur dioxide (SO<sub>2</sub>), followed by nitrogen oxides (NO<sub>x</sub>) and carbon monoxide (CO).

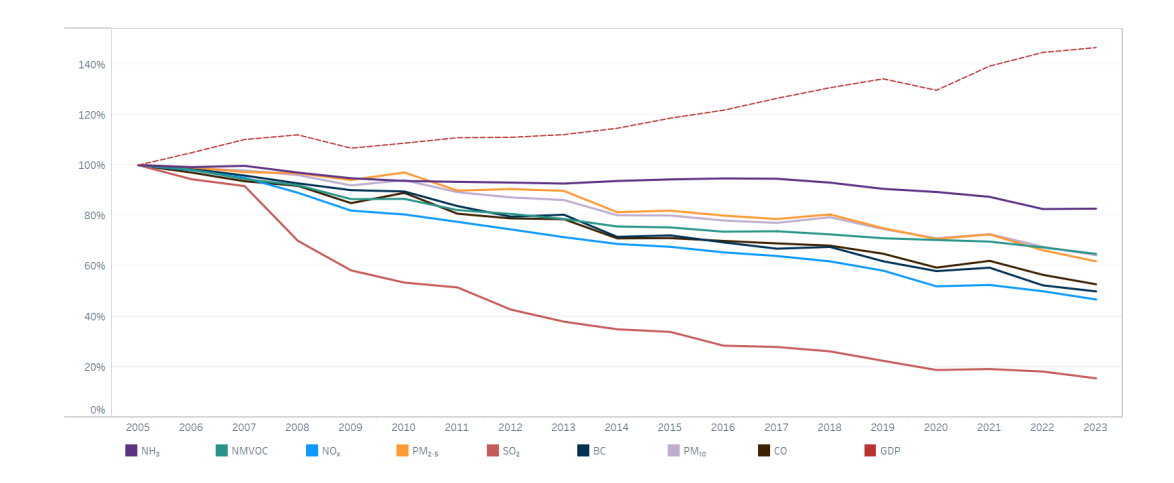


Figure 1.5: Trend in EU emissions between 2005 and 2023 [6]

Current policy implementations aim to reduce pollutant concentration to be compliant with the guidelines by 2030. However, the distribution of the air pollutant is not uniform across regions, but higher concentrations are generally found in urban areas, where human activities such as transportation and industrial processes are more prevalent.

#### 1.2 Transportation sector and regulatory framework

The transportation sector plays a significant role in greenhouse gas emissions, accounting for 23.8% of total European  $CO_2$  emissions, as shown in Figure 1.6.

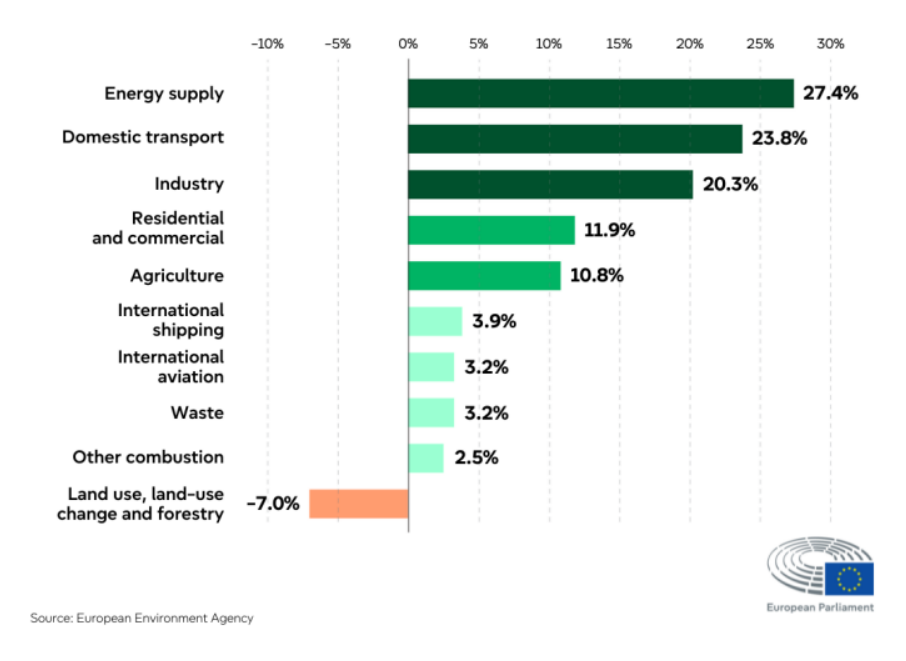


Figure 1.6: GHGs in EU by sector in 2022, expressed in CO<sub>2</sub> equivalent [3]

This sector is also a significant source of pollutants, with varying contributions depending on the pollutant species. As depicted in Figure 1.4, the transportation sector is the main source for the nitrogen oxides (NO<sub>x</sub>) and has a substantial impact on the emissions of particulate matter (PM) and non-methane organic volatile components (NMVOCs).

A major contribution to achieving the Green Deal objectives is expected from the reduction of emissions in the transport sector. Specifically, CO<sub>2</sub> emissions from passenger cars must be reduced by 55% by 2030, with all new cars required to be zero emissions by 2035. For vans, the targets are a 50% reduction by 2030 and zero emissions by 2035. In the case of heavy-duty vehicles, emissions must be reduced by 45% by 2030 and 65% by 2035. Starting in 2026, road transportation will be covered by the Emissions Trading System (ETS), introducing a cost for carbon emissions and thereby incentivising the adoption of cleaner fuels and investment in suitable technology. By 2050, the transport sector is expected to reduce its emissions by 90% to align with climate neutrality targets. This effort is also essential to be comply with the Net Zero Emissions by 2050 (NZE) scenario developed by the International Energy Agency (IEA), which outlines a normative pathway for the global energy sector to achieve net zero CO<sub>2</sub> emissions by 2050. Since each transportation sector is different, specific emission reduction targets will be needed, as shown in Figure 1.7

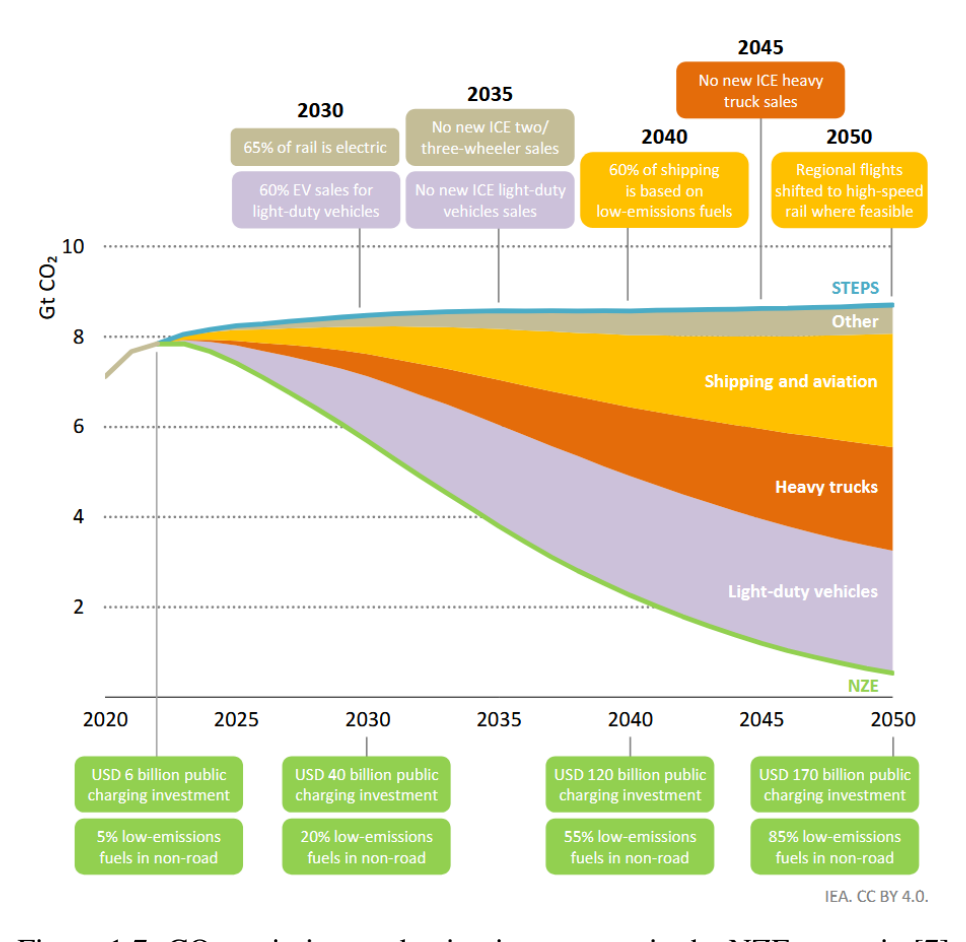


Figure 1.7: CO<sub>2</sub> emissions reduction in transport in the NZE scenario [7]

The decarbonization of the transportation sector can be structured into two main phases:

- 1. Switch to electricity, particularly through the adoption of battery electric vehicles (BEVs) and hydrogen fuel cell electric vehicles for road transportation.
- 2. Switch to use blend or direct low-emissions fuels such as biofuels, hydrogen and hydrogen based fuels, especially in heavy-duty vehicles.

Although the first phase appears to be an optimal solution, the advantages and disadvantages of electrification must be evaluated considering vehicle usage and conducting a life cycle assessment (LCA), including energy production, battery usage, reuse and recycling process. Taking these factors into account, high-efficiency internal combustion engine (ICE) powertrains are expected to continue to play a relevant role in the transition towards climate neutrality. Figure 1.8 shows the projected share of energy sources in the NZE scenario.

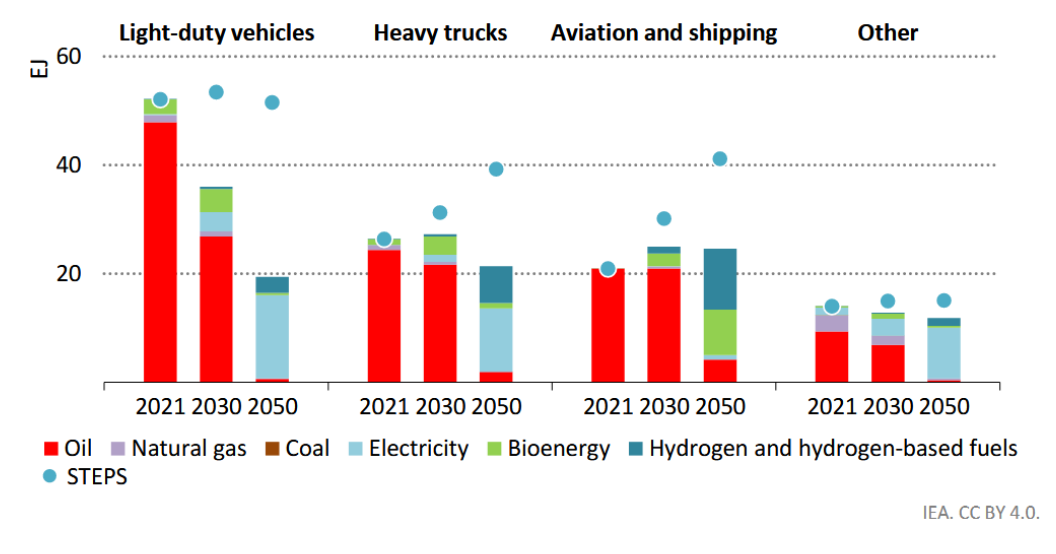


Figure 1.8: Present and future energy sources for transportation in NZE scenario [7]

As illustrated, while the future of light-duty vehicles, such as passengers cars, relies primarily on a shift from oil-based energy sources to electricity, the situation is different for heavy-duty vehicles, aviation and shipping. In the truck sector, the transition involves a reduction of oil dependency in favour electricity, hydrogen and hydrogen-based fuels. This is due to the different operational requirements of heavy-duty vehicles compared to passenger cars. Consequently, oil and low-emission fuels are expected to remain relevant, particularly for heavy-duty and shipping. Further technological development of internal combustion engines is therefore necessary to reduce both greenhouse gas and pollutant emissions, in order to comply with increasingly stringent environmental regulations. Further technological development of ICEs is therefore necessary to reduce both greenhouse gas and pollutant emissions, to comply with increasingly stringent environmental regulations.

In this context, hydrogen can be a key enabler for achieving the EU climate and energy targets, potentially reducing emissions in industry and particularly in the transportation sectors, as illustrated in Figure 1.9. Hydrogen is expected to be a solution to reach the emission reduction objective by 2030 and 2035 [8].

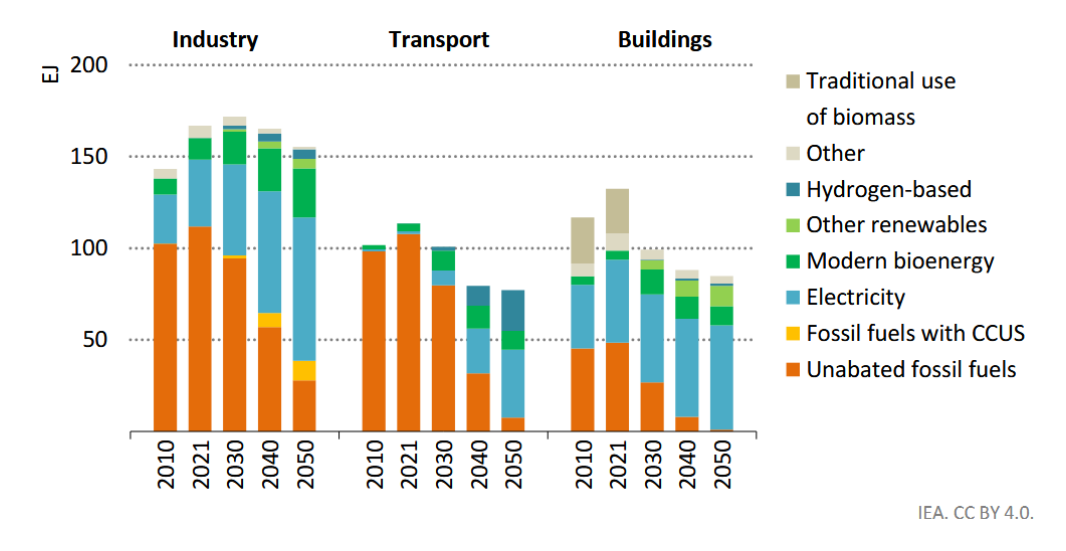


Figure 1.9: Present and future energy sources divided in the sector of utilisation in NZE scenario [7]

At the normative level, with regard to the pollutants (CO, NO<sub>x</sub>, PM and HC), European legislation for heavy-duty vehicles is divided into two categories: on-road and off-road vehicles. On-road vehicles are currently regulated in Europe by the Euro VI legislation, which came into effect in 2013 for new type approvals and in 2014 for all registrations. However, the Euro VII legislation was formulated in 2024 and will come into force starting from 2027. The Euro 7 regulation sets emission limits for both passenger transport vehicles (categories M1, M2 and M3) and goods transport vehicles (categories N1, N2 and N3). Within the regulation, heavy-duty vehicles are vehicles of categories M2, M3 and N2, N3. The distinction among passenger transport categories is based on the number of occupants and the maximum allowed mass, while for goods categories the classification is solely based on vehicle mass. Unlike previous standards, Euro 7 goes beyond tailpipe emission limits and introduces regulations for brake systems and tyres, concentrating particularly on particulate emissions and abrasion. Under Euro VI, different emission limits were applied for the two certification tests, the World Harmonized Stationary Cycle (WHSC) and the World Harmonized Transient Cycle (WHTC). With Euro 7, these limits are harmonized. Both tests are carried out on engine test benches:

- The WHSC is a steady-state test, in which the emissions are summed up on thirteen modes, which are a combination of speed and load.
- The WHTC is a transient cycle carried out over 1800 seconds, witch include urban, extra-urban and highway segments. The load profile is normalised relative to the

rated engine power to be comparable across different engines.

Figure 1.10 shows the emission limits introduced by Euro VII compared to the Euro VI ones.

	WHS	C (only Cl en	gines)	wнтс	(CI and SI er	iglnes)	On-ro	oad emission:	s limit
	Euro VI (mg/kWh)	Euro 7 (mg/kWh)	Change compared to Euro VI	Euro VI (mg/kWh)	Euro 7 (mg/kWh)	Change compared to Euro VI	Euro VI (mg/kWh)	Euro 7 (mg/kWh)	Change compared to Euro VI
NO <sub>x</sub>	400	200	-50%	460	200	-56%	690	260	-62%
PM	10	8	-20%	10	8	-20%	_	_	_
PN <sub>10</sub> <sup>a</sup>	8x10 <sup>11</sup>	6x10 <sup>11</sup>	No change	6x10 <sup>11</sup>	6x10 <sup>11</sup>	No change	9.8x10 <sup>11</sup>	9x10 <sup>11</sup>	-8%
со	1500	1500	No change	4,000	1,500	-62%	6,000	1,950	-68%
NMOG	_	80	-38% <sup>c</sup>	160 <sup>b</sup>	80	-50%	240	105	-56%
тнс	130	-	-	160°	-	-	-	-	-
NH <sub>3</sub>	_	60	New	_	60	New	_	85	_
CH <sub>4</sub>	-	500	New	500 <sup>b</sup>	500	No change	750	650	-13%
N <sub>2</sub> O	_	200	New	_	200	New	_	260	_

Notes: WHSC: World Harmonized Stationary Cycle; WHTC: World Harmonized Transient Cycle; CI: Compression ignition; SI: Spark ignition; Particle number limit in #/kWh; Donly for gas engines; Only for diesel engines; Control of Compared to Euro VI THC

Figure 1.10: Euro 7 tailpipe emission limit for heavy-duty vehicles of categories N2, N3, M2 and M3 [9]

As illustrated, tailpipe emission limits become more stringent:

- NO<sub>x</sub> emissions are reduced by 50% under WHSC and by 56% under WHTC
- Particulate matter limits are lowered by 20%
- CO emissions during the WHTC must be reduced by 62%.
- Euro VI total hydrocarbon (THC) limit has been replaced with two separate limits: one for non-methane organic gases (NMOG) and one for methane (CH<sub>4</sub>).
- New limits have been introduced for ammonia (NH<sub>3</sub>) and nitrous oxide (N<sub>2</sub>O).

To verify emissions under real driving conditions (RDE), Euro 7 maintains the general framework present under Euro 6, but introduces stricter compliance criteria. The conformity factor is reduced from 1.5 to 1 for all pollutant species, and the power threshold for assessing the validity of the windows used in the evaluation is lowered to 6%, enabling the inclusion of more low-load and low-speed operation. As under Euro 6, the emission limits during RDE tests are higher than those of the type-approval cycles to consider the test-to-test variability.

Another important update concerns the vehicle lifetime requirements. Euro 7 extends the minimum compliance period compared to Euro 6. Moreover, for all vehicles with tailpipe emissions, Euro 7 imposes the installation of On-board emissions monitoring (OBEM) systems capable of monitoring continuously the levels of NO<sub>x</sub>, PM, and in the case of heavy-duty vehicles, also NH<sub>3</sub> levels [9].

#### 1.3 Methane as a fuel

Compressed natural gas (CNG) is produced by compressing conventional natural gas, which is composed mainly of methane CH<sub>4</sub> and other alkanes, to less than 1% of its volume at standard atmospheric pressure. Methane is becoming an increasingly popular fuel for engines due to its chemical and environmental properties. CNG engines are distinguished principally for the high octane number of natural gas, generally between 120 and 130, allowing engines to work with a higher compression ratio of up to 16:1. This results in thermal efficiency close to 35%, about 10% higher than conventional gasoline engines. The low molecular weight of natural gas helps create a more homogeneous air-fuel mixture, improving combustion quality. Another advantage is the lower brake specific fuel consumption (BSFC), typically 12-20% less than gasoline engines, and a thermal efficiency that is 5-12% higher, thanks to CNG's higher heating value and its slow, lean combustion. However, a drawback of this type of fuel is that CNG engines generally produce 15-20% less brake power, mainly due to slower combustion and reduced volumetric efficiency, since the gaseous fuel occupies space that would otherwise be filled with air needed for combustion. From an environmental point of view, CNG is a cleaner fuel. Its high hydrogen-to-carbon ratio reduces the CO<sub>2</sub> emissions by about 20% compared to gasoline under similar operating conditions. Emissions of nitrogen oxides (NO<sub>x</sub>) and particulate matter (PM) are also lower compared to conventional engines [10].

#### 1.4 Hydrogen as a fuel

Since hydrogen is a carbon-free fuel, it offers several advantages: a high flame speed, wide flammability limits, and a very short quenching distance, all characteristics that contribute to stable combustion and more efficient combustion even with lean mixture. Hydrogen combustion produces negligible amounts of CO, CO<sub>2</sub> and unburned hydrocarbon. However, NO<sub>x</sub> emissions can increase due to the higher combustion temperatures. This is one of the three primary conditions necessary for nitrogen oxides formation. The other two are to have enough time for the reactions to occur and a high concentration of oxygen. Since hydrogen combustion can be under leaner conditions, the oxygen concentration inside the cylinder is higher. Therefore, when all three conditions are satisfied, an ideal environment for NO<sub>x</sub> formation is established. The impact on power output is variable: in some cases, increases are observed due to improved combustion efficiency, while in others, reductions occur because the lower volumetric density of hydrogen limits the fuel mass that can be inspired [11].

#### 1.5 Hydrogen-methane blends

Hydrogen enrichment in methane-air mixtures has emerged as a promising strategy to improve the efficiency and reduce pollutant emissions in internal combustion engines. Recent studies have investigated the impact of varying hydrogen concentrations, up to 50% in mass, on flame dynamics, combustion temperature, and pollutant formations. It has been observed that hydrogen addition makes the mixture leaner, enhancing flame propagation, shifting peak temperature zones closer to the inlet, and improving combustion stability. This results in a reduction in the outlet temperature of up to 37%. Furthermore, a significant reduction in CO and CO<sub>2</sub> (up to 99.9% and 88% respectively) has been achieved due to both the lower carbon content of the fuel blend and more complete combustion process. However, as said in section 1.4, as hydrogen content increases, NO<sub>x</sub> emissions tend to rise due to higher flame temperature. Nevertheless, maintaining the H<sub>2</sub> concentration below 30% by mass helps contain nitrogen oxides formation within acceptable limits [12].

Under stoichiometric conditions, hydrogen addition does not lead to a significant improvement in thermal efficiency. This is primarily due to increased heat losses related to higher flame speeds and enhanced heat transfer, especially near the combustion chamber walls. In contrast, under lean burn conditions, hydrogen extends the lean flammability limits, allowing for more efficient combustion and reduced NO<sub>x</sub> emissions [13]. From a flame stability perspective, experimental investigations have shown that hydrogen enrichment increases the lean blowout limits. It is the threshold below which the flame extinguishes under lean conditions. This enhancement in flame stability enables more robust operation at low equivalence ratios. However, the increased reactivity and laminar flame speed also elevate the risk of flashback, a phenomenon in which the flame propagates upstream into the intake system. This can damage components not designed to tolerate high temperatures and create dangerous situations [14].

#### 1.6 GT-SUITE description

GT-SUITE, which includes the GT-Power Engine Library, is a simulation platform used by engine manufacturers and suppliers for modelling, analysis, and optimisation of internal combustion engines and complete vehicle systems. It supports the entire development process, from project initiation to detailed analysis [15]. The software relies on a one-dimensional (1-D) fluid dynamics solver that numerically resolves the conservation equations of mass, momentum, and energy using the finite difference method. This allows accurate transient simulations of thermal and fluid dynamics phenomena. Models are built by combining predefined templates of physical components (e.g. cylinders, valves, engine blocks, turbochargers) with geometrical elements such as pipes and junc-

tions, along with appropriate boundary conditions. In this work, a digital twin of a CNG heavy-duty engine is implemented in GT-SUITE and two applications are employed for model setup and result analysis:

- **GT-ISE**: Graphical interface used for the construction, configuration, and modification of the model.
- GT-POST: Post-processing environment used to execute the simulations and visualize the results.

A digital twin is intended as a virtual representation of a physical system, to replicate accurately its behaviour under operating conditions. This methodology allows engineers to perform tests and performance evaluations directly on the digital model, avoiding the necessity of prototypes or real engine testing. In this way, it is possible to reduce both development time and cost, while ensuring great control, easy optimisation and fast design iterations. The main challenge in using such a model is the calibration process, which is essential to ensure that the virtual system reflects the behaviour of the physical one, generating in this way reliable and consistent results.

#### 1.7 Research objectives

The aim of this thesis is the study and optimisation of the behaviour of a heavy-duty engine fuelled with methane-hydrogen mixtures, through numerical simulations performed in the GT-SUITE environment. The first phase focuses on the calibration of the engine model to ensure accuracy and consistency with experimental data, thereby providing a solid basis for the subsequent analyses. Advanced methodologies, such as the nonpredictive Three-Pressure Analysis and the predictive SI-TURB model, are then developed and optimised to achieve a more accurate characterisation of the combustion process and heat release rate. The impact of hydrogen introduction on engine performance and emissions is also investigated, with particular attention to the overall efficiency and pollutant formation. In addition, hydrogen enrichment can increase the knock tendency due to its higher laminar flame speed, which accelerates combustion and leads to higher in-cylinder temperatures and pressures, as well as the increased chemical reactivity of the mixture. This study aims to evaluate the influence of specific operating conditions on combustion stability. Finally, a transient analysis is performed to verify the reliability of the calibrated model under dynamic operating conditions. This study represents a preparatory step towards the complete utilisation of hydrogen as a fuel, supporting the adoption of alternative fuels aimed at reducing greenhouse gas emissions and air pollutants in future powertrain applications.

### Chapter 2

### Steady-state analysis

This section aims to explain how the engine model is built and the methodology adopted to simulate the combustion of a methane (CNG) and hydrogen (H<sub>2</sub>) mixture at different dilution levels. The objective is to reproduce engine performance as closely as possible to the real operating conditions, while reducing pollutant emissions and promoting a cleaner combustion process.

#### 2.1 Engine model description

The present study was conducted on a heavy-duty, turbocharged, spark-ignition engine fueled with CNG. The real engine is analysed by the Institute of Science and Technologies for Sustainable Energy and Mobility (STEMS) of the Italian National Research Council in Naples. During the thesis activity, the author had the opportunity to spend a training period at the institute, directly observing the data acquisition process, the experimental setup, the test benches and the engine used for the analyses. This experience allowed to better understand the experimental procedures and provided valuable technical and personal insights complementary to the numerical activities carried out. Key specifications of the engine are summarised in Table 2.1:

Туре	Turbocharged, CNG, SI
Cylinders arrangement	6L
Engine displacement	5.9 [L]
Valves per cylinder	4
Injection system	Multi-Point Injection (MPI)
Turbocharger control	Wastegate valve

Table 2.1: Engine specifications

The baseline engine model (Figure 2.1), built in the GT-POWER environment, is composed of several objects connected by links, which can be customised to reproduce the

characteristics of the real engine. Among these objects, the injectors, cylinders and throttle valve are the most interesting and critical for engine operation and are the components on which the majority of the work has been focused.

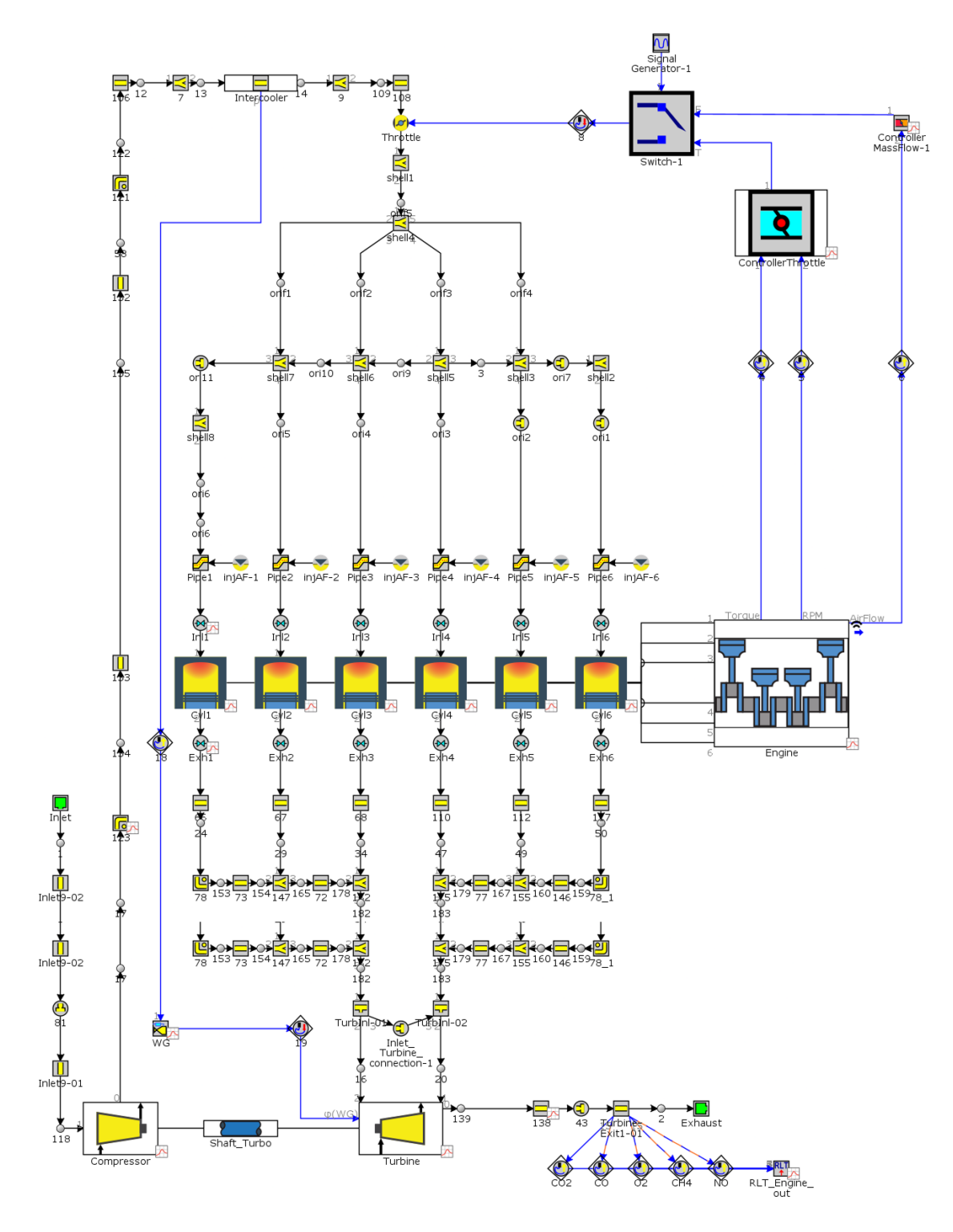


Figure 2.1: Baseline six-cylinder engine model

Injectors are modelled using the "InjAF-RatioConn" objects, which inject fuel at a specified fuel-to-air ratio into a pipe or flow split. In this study, the injectors are controlled via lambda ( $\lambda$ ), defined as the ratio between the actual air-to-fuel ratio and the stoichiometric one.

$$\lambda = \frac{\left(\frac{m_{air}}{m_{fuel}}\right)_{actual}}{\left(\frac{m_{air}}{m_{fuel}}\right)_{stoichiometric}}$$
(2.1)

This component automatically adjusts the correct amount of fuel injected required to maintain the imposed  $\lambda$  value, which in this study is always set to one, depending on the engine operating conditions. The cylinder block is divided into several sections, each dedicated to defining a specific part of the cylinder object. One important section is the "Combustion Objective", which is the in-cylinder combustion model used in the simulation. For the first calibration of the engine model, a Wiebe combustion function is used. This function describes how the mass fraction burned (MFB) evolves during combustion as a function of the crank angle:

$$x_b(\alpha) = 1 - \exp\left[-a\left(\frac{\alpha - \alpha_0}{\Delta\alpha}\right)^{m+1}\right]$$
 (2.2)

where  $\alpha_0$  is the start of combustion,  $\Delta \alpha$  is the combustion duration, m is the shape factor controlling the slope of the curve, and a is the combustion efficiency parameter.

The throttle regulates the amount of air introduced into the intake manifold to reach the desired target torque. The throttle controller adjusts the throttle opening using a closed-loop control from the engine crank train object, based on the required load or the airmass flow. The controller operates according to the fuel-air equivalence ratio  $\phi$ , which is defined as the inverse of  $\lambda$ . The strategy by which the controller switches between the two different controllers will be explained in detail in the chapter on transient analyses 3.1.

$$\phi = \frac{1}{\lambda} = \frac{\left(\frac{m_{fuel}}{m_{air}}\right)_{actual}}{\left(\frac{m_{fuel}}{m_{air}}\right)_{stoichiometric}}$$
(2.3)

For the steady-state analysis, the six-model engine described above was not utilised. Instead, an equivalent mono-cylinder model was developed (Figure 2.2).

This approach simplifies the analysis without losing fundamental information on the combustion and thermodynamic cycle. A mono-cylinder engine does not account for complexities linked to interaction between cylinders, the balancing of manifold flows or igni-

tion sequence. When the objective is to study steady-state combustion, efficiency or the variation of certain parameters, this level of modelling is sufficient.

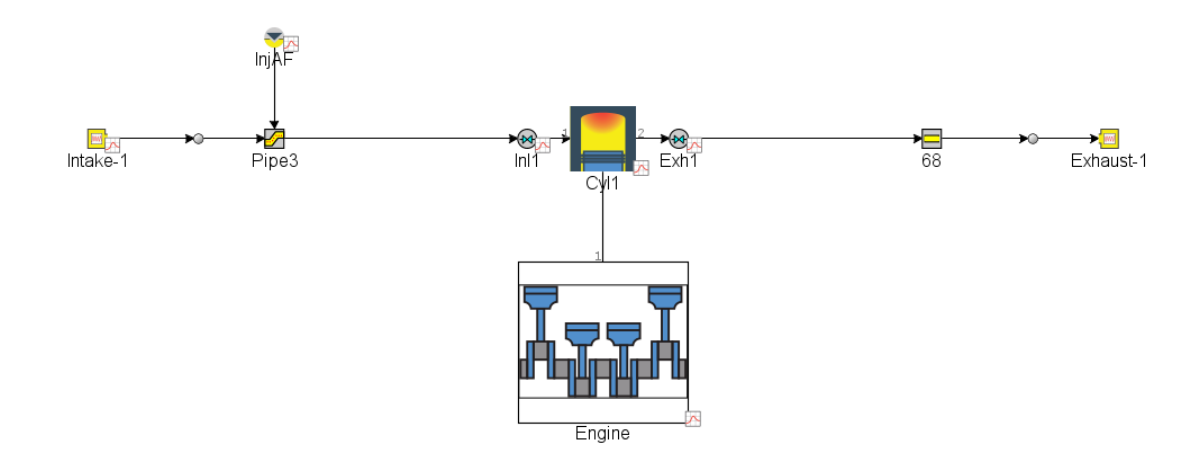


Figure 2.2: Mono-cylinder engine model

The mono-cylinder model includes only the injector, the cylinder and the engine from the complete engine model. It is necessary to introduce the blocks of the intake and the exhaust, to impose the boundary conditions for temperature, pressure and combustion composition.

#### 2.2 Feasibility study

This part aims to check if the engine model is correctly built by comparing some engine performance parameters from the simulation with the real ones. The steady-state analysis relies on four representative operating points: 1100 rpm x 290 Nm, 1400 rpm x 185 Nm, 1400 rpm x 560 Nm and 2100 rpm x 340 Nm. For simplicity, up to now, these operating points are called:

- 1100 rpm × 290 Nm: first operating condition, labelled C1.
- 1400 rpm × 185 Nm: second operating condition, labelled C2.
- 1400 rpm × 560 Nm: third operating condition, labelled C3.
- 2100 rpm × 340 Nm: fourth operating condition, labelled C4.

These points were chosen to cover the engine map well while keeping the computations manageable. They also capture the main engine conditions that are important for combustion calibration and emissions.

As it is possible to see in Figure 2.3, C1 represents low speed and mid load, C2 is mid speed and low load, C3 is mid speed and high load near peak torque, and C4 is higher

speed with medium load. This selection ensures that the main combustion behaviours and thermal states of the engine are included.

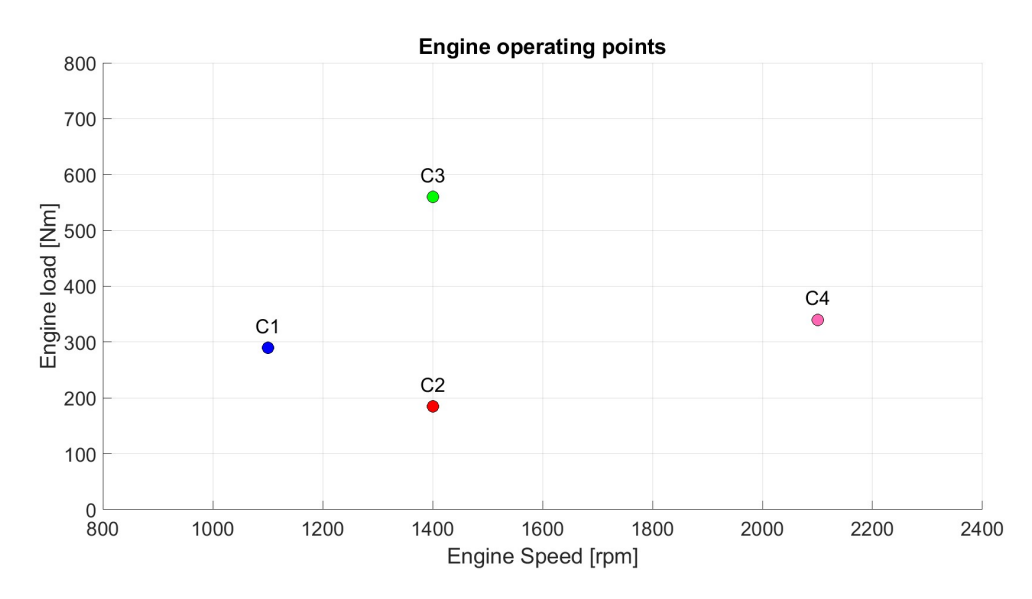


Figure 2.3: Map of selected engine operating points

Using these distinct points also allows the model to interpolate parameters reliably across the engine map without overfitting to a single condition. Finally, the points reflect conditions that occur frequently or have a strong impact on the target duty cycle, so optimising these points improves fuel consumption and emissions in real use.

In each case, several performance parameters were imposed. Among them, the most important are the initial boost pressure, the pressure and temperature at the intake manifold, the engine speed, and the parameters relative to the Wiebe function, including the crank angle at 50% mass fraction burned, the combustion duration between 10-90% of the burn, and the Wiebe exponent. This model implements a reasonable burn rate if measured cylinder pressure is not available.

To perform a consistent comparison between the real engine and the simulated one, several performance parameters are considered, such as BMEP, IMEP, and Brake Torque. In the Table 2.2, the acronym Exp refers to data obtained from the real engine, while Sim refers to data from the simulated model.

Parameters	Brake Torque [Nm]		IMEP [bar]		BMEP [bar]	
	Exp	Sim	Exp	Sim	Exp	Sim
C1	290.38	290.04	7.69	7.96	6.08	6.19
C2	184.72	185.16	5.40	5.40	3.87	3.95
C3	559.08	560.22	13.35	14.15	11.71	11.96
C4	340.50	340.56	8.57	9.29	7.13	7.27

Table 2.2: CNG engine performance parameters – Wiebe combustion model

The parameters considered above represent:

- Brake Torque: represents the effective torque delivered at the crankshaft.
- **IMEP**: the indicated mean effective pressure represents the average pressure inside the cylinder, obtained from the in-cylinder pressure trace. It is a useful parameter to evaluate the ideal combustion quality and efficiency before mechanical losses.
- **BMEP**: the brake mean effective pressure is a normalised measure of the torque per unit of engine displacement. It is a useful parameter to compare engines of different sizes. It can be calculated by subtracting the mechanical and friction losses (FMEP) from the IMEP.

These parameters have been used for comparing the real engine and the simulated one, as they provide a comprehensive evaluation of engine performance. The brake torque describes the engine's capacity to generate work, while BMEP and IMEP enable a normalised analysis and comparison, independent of the engine displacement.

Looking at the values included in Table 2.2, it is possible to notice that the engine model is well calibrated to replicate the real engine. Regarding the brake torque, all of the operating points satisfy the required real torque, while some differences are present for the other parameters. The IMEP for the first two operating points matches the real engine, whereas for the high-speed and high-load points, the model predicts slightly higher values. This can be attributed to the combustion profile created by the Wiebe function. At higher loads, the burn rate or peak pressure may be overestimated, resulting in an increased IMEP. For all operating points, the BMEP is higher in the simulation. This indicates that the model burns more fuel to produce the same torque, probably due to simplified loss modelling, differences in the combustion shape, and underestimated mechanical losses. The torque is maintained equal because the model is calibrated to reproduce the real engine's output.

To execute a complete comparison, the in-cylinder pressure profiles of the two engines were also compared, as shown in the Figures 2.4-2.7.

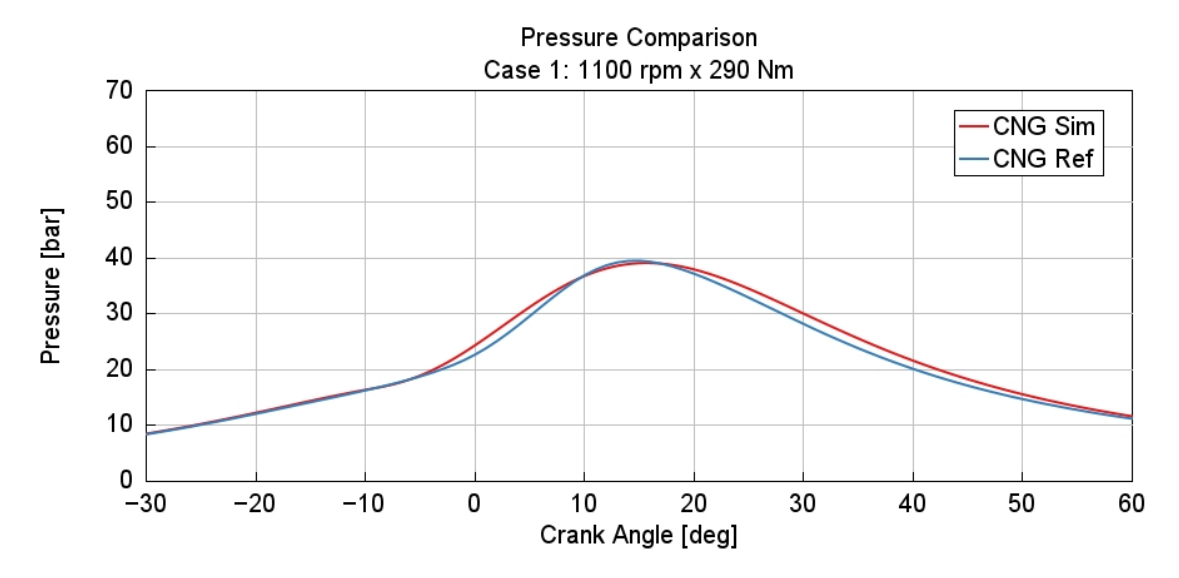


Figure 2.4: CNG In-cylinder pressure – Wiebe combustion model (C1)

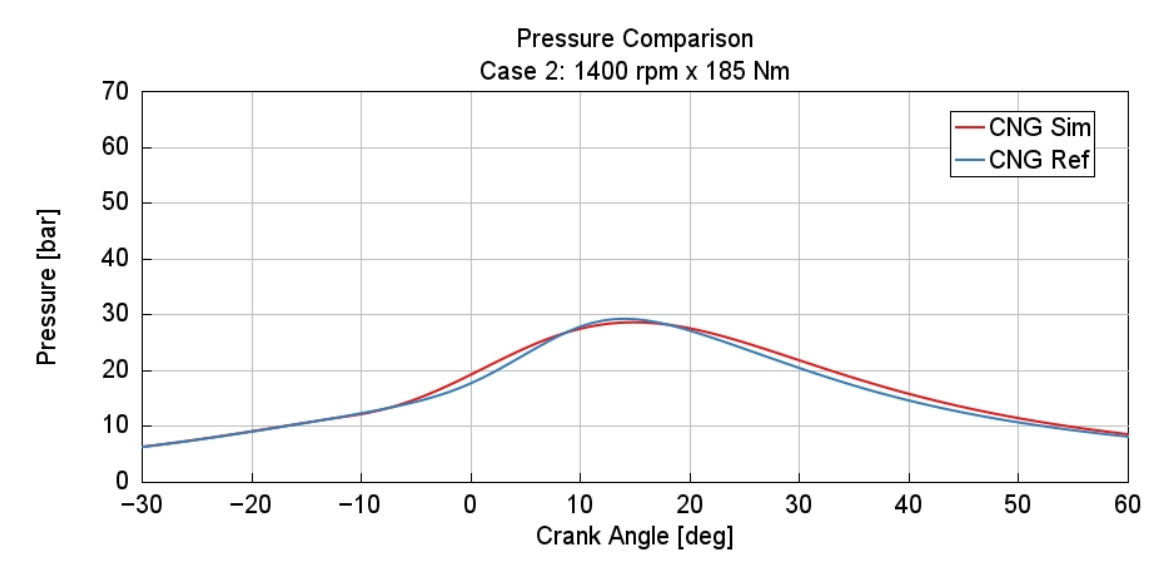


Figure 2.5: CNG In-cylinder pressure – Wiebe combustion model (C2)

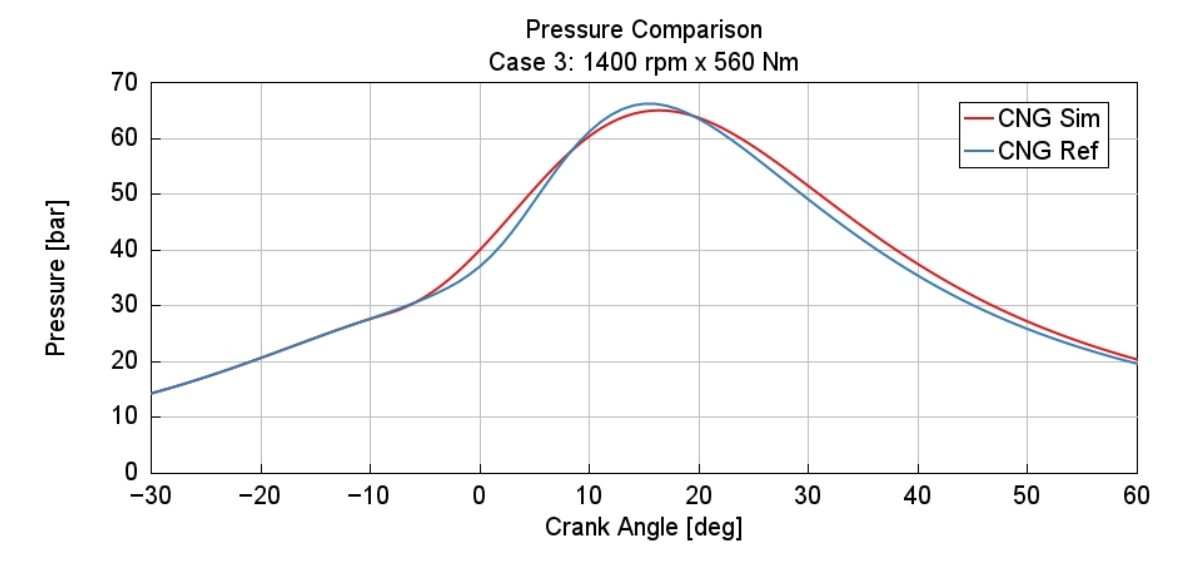


Figure 2.6: CNG In-cylinder pressure – Wiebe combustion model (C3)

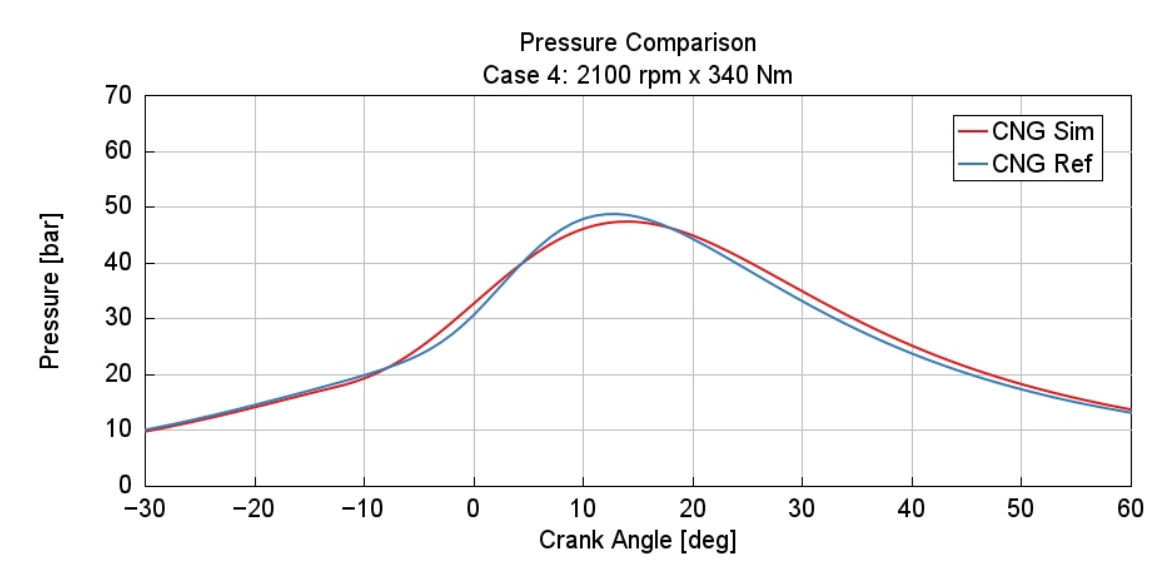


Figure 2.7: CNG In-cylinder pressure – Wiebe combustion model (C4)

The considerations drawn for pressure comparison graphs, are general and not specific for a single operating condition since the curves exhibit a similar shape, although with different absolute values, and a consistent overall trend.

From the comparison between the two in-cylinder pressure traces, it is noticeable that the red curve, corresponding to the experimental data, shows a slightly higher and earlier peak pressure compared to the simulated one. The rightward shift of the blue peak indicates a combustion delay. Furthermore, in the rising phase, the simulated curve presents a less steep slope, indicating a more gradual energy release. In contrast, during the descending phase, the two curves align more closely, with an almost complete overlap towards the end of the cycle. This analysis highlights that the model is capable of qualitatively reproducing the real combustion trend, though with some discrepancies in terms of timing and peak pressure. Based on both the engine performance parameter analysis and the

pressure comparison, the developed and calibrated model can be considered adequate for representing the engine behaviour under the analysed conditions. The deviations observed can be regarded as acceptable, especially considering that this is the first version of the engine model. As explained in the following sections, the model will be further refined to improve its accuracy and achieve a closer representation of the real engine.

## 2.3 Burn rate determination from Measured Cylinder Pressure

The calculation of the burn rate from measured in-cylinder pressure is a reverse procedure, since the roles of inputs and outputs are opposite to those in conventional combustion simulations. In this case, the in-cylinder pressure trace is the input, and the burn rate profile is the resulting output. Within GT-SUITE, two methodologies are available to estimate the apparent burn rate from measured pressure data: the Closed Volume Analysis (CPOA) and the Three Pressure Analysis (TPA). Both methods produce the same type of outputs, but they differ in the way additional input data, beyond the measured cylinder pressure, is obtained.

The CPOA method is a stand-alone calculation that requires only the measured in-cylinder pressure, together with some basic cycle-averaged quantities and cylinder geometry. A highly simplified model is used, including only the engine cylinder and cranktrain. The simulation runs two consecutive cycles (by repeating the first one) to ensure proper convergence of the results. For this reason, valves and ports are not necessary. However, it is crucial to properly set the initial conditions, as they represent the trapped conditions at the Intake Valve Closing (IVC). The main advantages of this method are its low computational cost and the limited input requirements (only in-cylinder pressure). On the downside, it relies on the estimation of the trapping ratio and residual fraction, parameters that are generally difficult or even impossible to measure experimentally.

The TPA method, on the other hand, requires three measured pressures: intake, incylinder and exhaust. In this case, there is no need to impose the residual fraction and trapping ratio as external inputs, since these quantities are internally calculated by the model. The required simulation model is slightly more complex, as it must include at least valves and ports. The calculation proceeds over multiple cycles until convergence is reached, ensuring consistent trapping conditions. The benefit of this approach is that all the trapped quantities are predicted directly, provided that the flow characteristics of the model are accurately defined. The disadvantages are the need for additional experimental data and higher computational cost due to the iterative nature of the convergence process. Since the experimental trapping ratio and residual fraction of the tested engine are unknown, the Three Pressure Analysis was selected for burn rate determination.

As highlighted in the GT-POWER manual [16], when a TPA model is derived from a full engine model, injector templates must be adapted. In particular, if the original injectors were controlled by the A/F ratio, they must be replaced by injectors regulated through direct fuel mass or mass flow rate imposition. They must have the same delivery rate, pulse width, and timing as the original configuration. An accurate definition of the port injection profile is crucial, since any deviation can significantly affect the pressure wave dynamics.

#### 2.3.1 Injector change

Before performing the Three Pressure Analysis, the injector type implemented into the model was modified. The original configuration used "InjAF-RatioConn" injectors, which regulate the injected fuel mass by controlling the fuel-to-air ratio and automatically adjusting the fuel quantity. Two alternative injector types were tested:

- **InjRateConn**, where the injected fuel mass flow rate is directly imposed.
- InjPulseConn, where the total injected mass per cycle is imposed.

The required fuel mass and flow rate were extracted from the GT-POST results of the initial simulations with the "InjAF-RatioConn" injectors. The analysis demonstrates that engine performance parameters and the in-cylinder pressure comparison remain consistent with those obtained using the previous injector model. Moreover, the effective lambda at Exhaust Valve Opening (EVO), reported in Table 2.3, remains within the stoichiometric conditions for both injector types at all operating points.

	InjAF-RatioConn	InjRateConn	InjPulseConn
C1	1.0035	1.0046	1.0036
C2	1.0022	1.0030	1.0021
C3	1.0039	1.0052	1.0032
C4	1.0017	1.0041	1.0038

Table 2.3: Effective  $\lambda$  at EVO changing the CNG injector

These results demonstrate that replacing the injector, while keeping the injected fuel mass constant, does not affect the overall model behaviour. The "InjPulseConn" injector was selected for all future steady-state analyses.

#### 2.3.2 Three Pressure Analysis (TPA)

The analysis performed with the TPA procedure, aimed at calculating the burn rate at different engine operating points, was necessary to obtain the real burn rate that governs the combustion process. Up to this point, combustion has been modelled using the Wiebe

function, which, as previously mentioned, reproduces the experimental parameters and pressure traces fairly well, although some discrepancies are still present. By applying this procedure, it is instead possible to determine a burn rate specific to each engine operating condition, thereby improving both the accuracy and reliability of the model. This analysis is also fundamental for the predictive analyses described in the following sections.

As previously explained, three pressure measurements are required for the TPA analysis. Two of them are port pressures (intake and exhaust), and the third is in-cylinder pressure. In addition to these, further experimental data must be provided, including:

- **Intake port temperature**: the average temperature at the same location where intake port pressure is measured;
- **EGR fraction**: the average air mass flow rate and EGR flow rate to determine EGR fraction at intake port. This parameters is not necessary in this case, as the engine does not employ EGR;
- Fuel injected data: injected mass, profile, and timing;
- Spark timing.

Once the model has been correctly defined, the simulations are carried out and the results provide the performance parameters summarised in Table 2.4. As in the previous case, the parameters chosen for comparison with the experimental data are those that are more representative for a consistent evaluation.

Parameters	Brake Torque [Nm]		IMEP	P [bar] BMEI		P [bar]	λ [-]	
	Exp	Sim	Exp	Sim	Exp	Sim	Exp	Sim
C1	290.38	290.80	7.69	7.41	6.08	6.21	1	1.001
C2	184.72	185.16	5.40	5.18	3.87	3.95	1	1.001
C3	559.08	560.04	13.35	13.79	11.71	11.96	1	1.003
C4	340.50	340.11	8.57	9.09	7.13	7.26	1	1.005

Table 2.4: CNG engine performance parameters - TPA combustion model

As can be noticed, all parameters are closer to the experimental values, confirming that the engine model is correctly set up and reliable. When comparing these results with those obtained using the Wiebe function as a combustion object, no particular differences in the performance parameters can be identified. It is also reported the value of  $\lambda$  to confirm that stoichiometric conditions are preserved even when modifying the injector configuration. The most significant improvement achieved through this analysis emerges from the in-cylinder pressure comparison between experimental and simulated data.

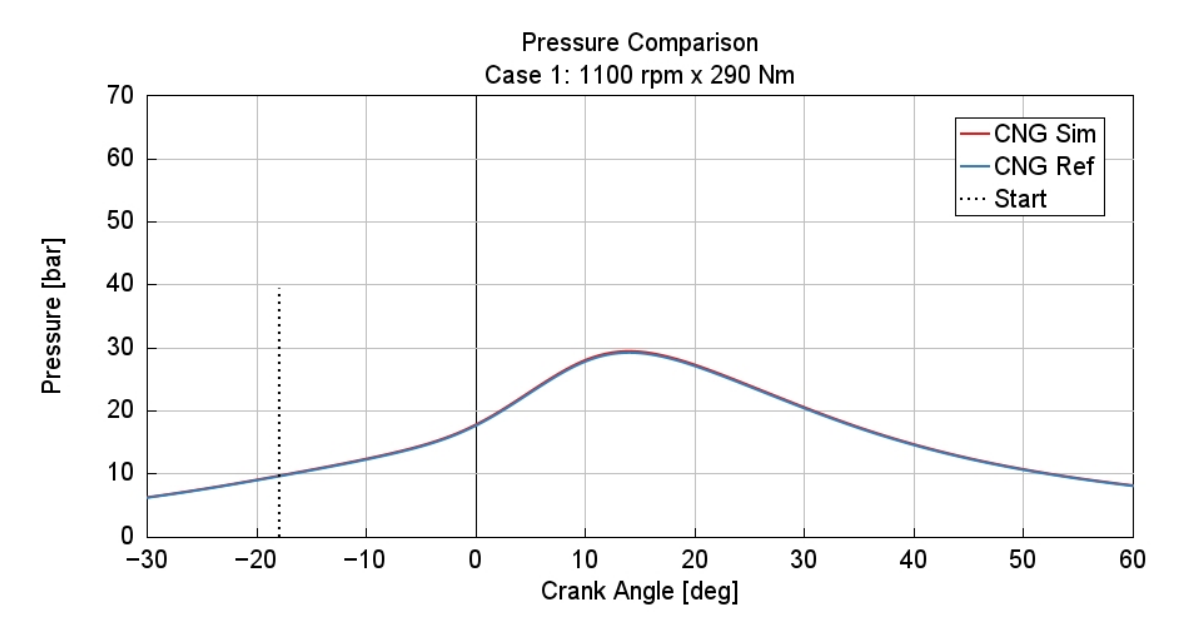


Figure 2.8: CNG In-cylinder pressure - TPA combustion model (C1)

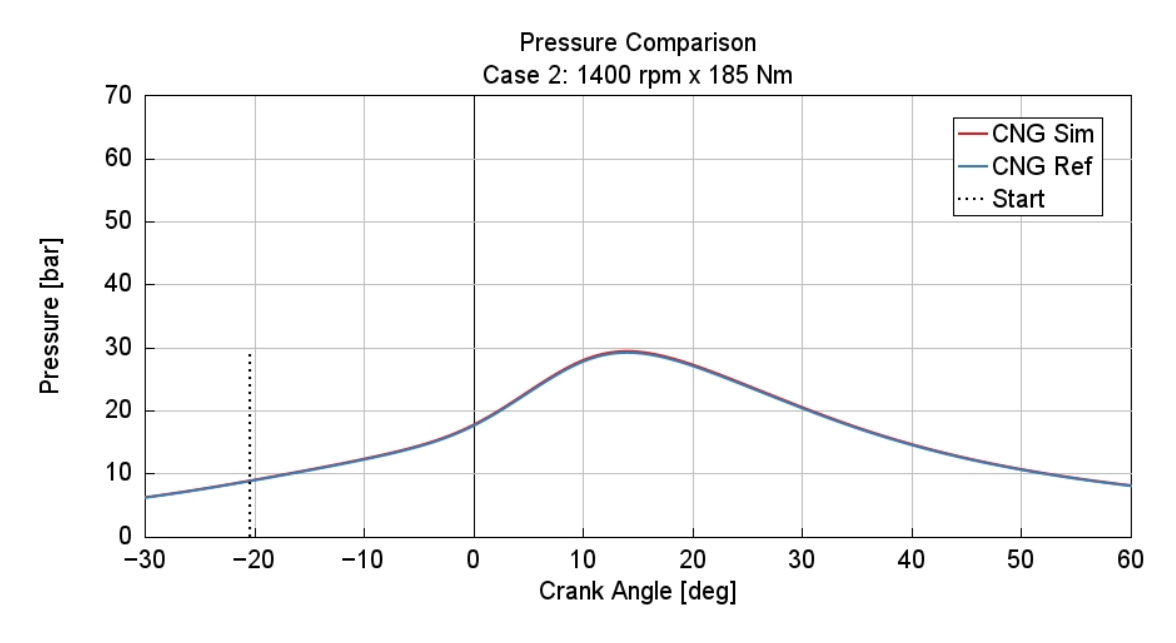


Figure 2.9: CNG In-cylinder pressure - TPA combustion model (C2)

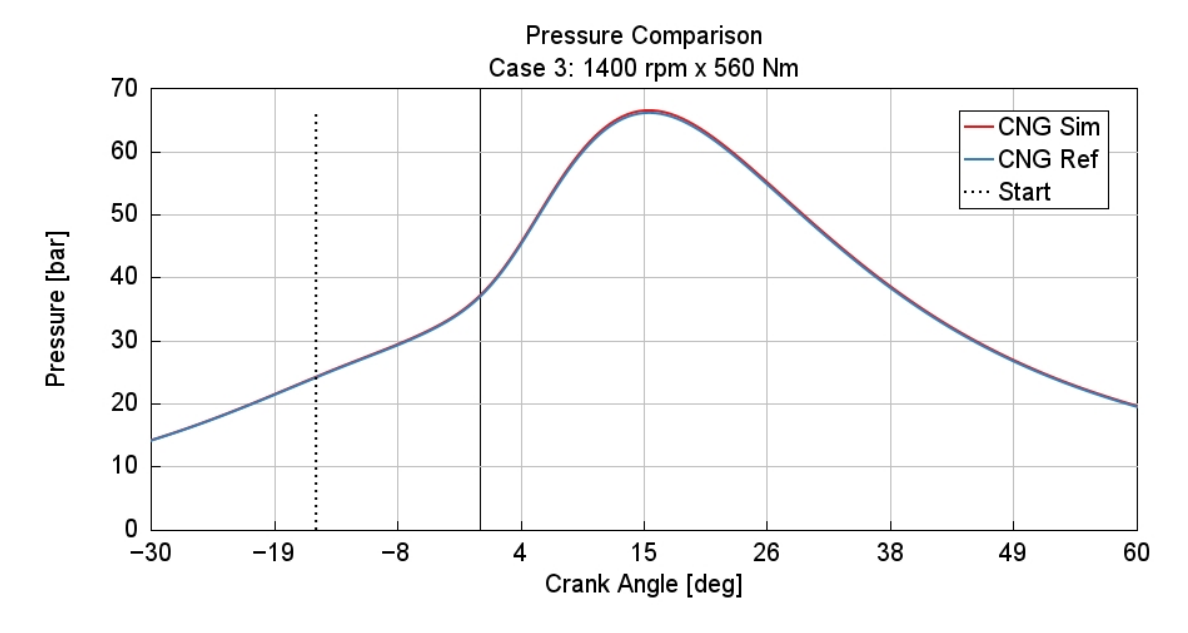


Figure 2.10: CNG In-cylinder pressure - TPA combustion model (C3)

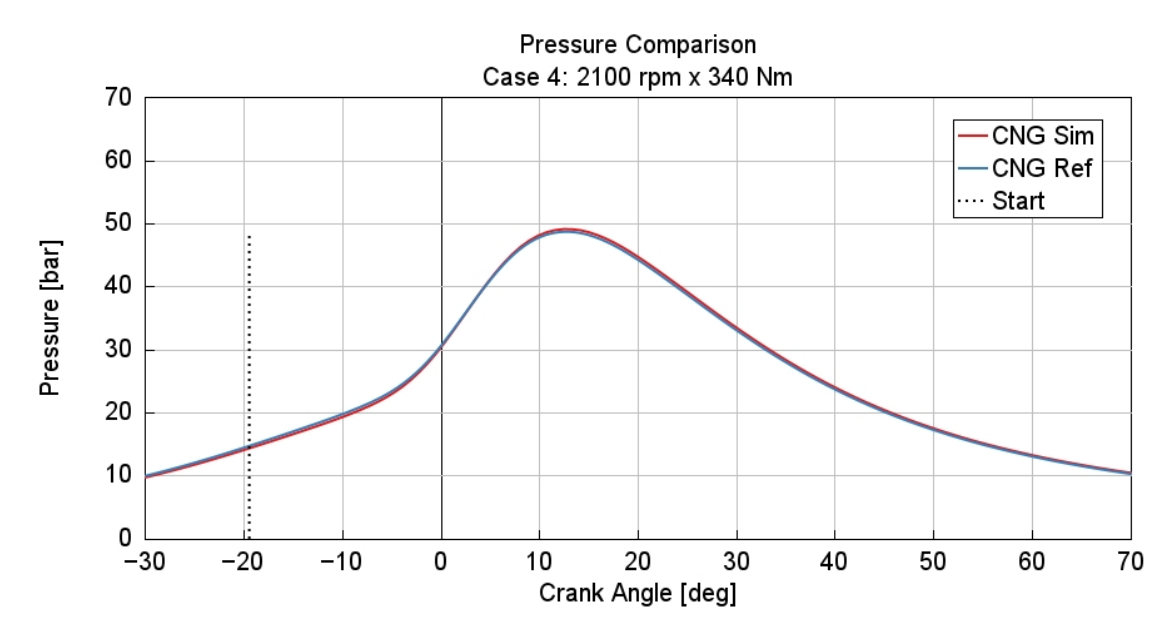


Figure 2.11: CNG In-cylinder pressure - TPA combustion model (C4)

As shown in the pressure traces, Figures 2.8-2.11, using a burn rate derived from experimental pressures for each operating point allows the simulated pressure curve to almost perfectly overlap the experimental one. The accurate matching of the peak pressure magnitude and phasing indicates a correct estimation of both the start and the development of the combustion process. This confirms that the simulation model is properly defined and provides reliable results.

However, the most important result of the TPA analysis lies in the burn rate profiles reported in Figures 2.12-2.15.

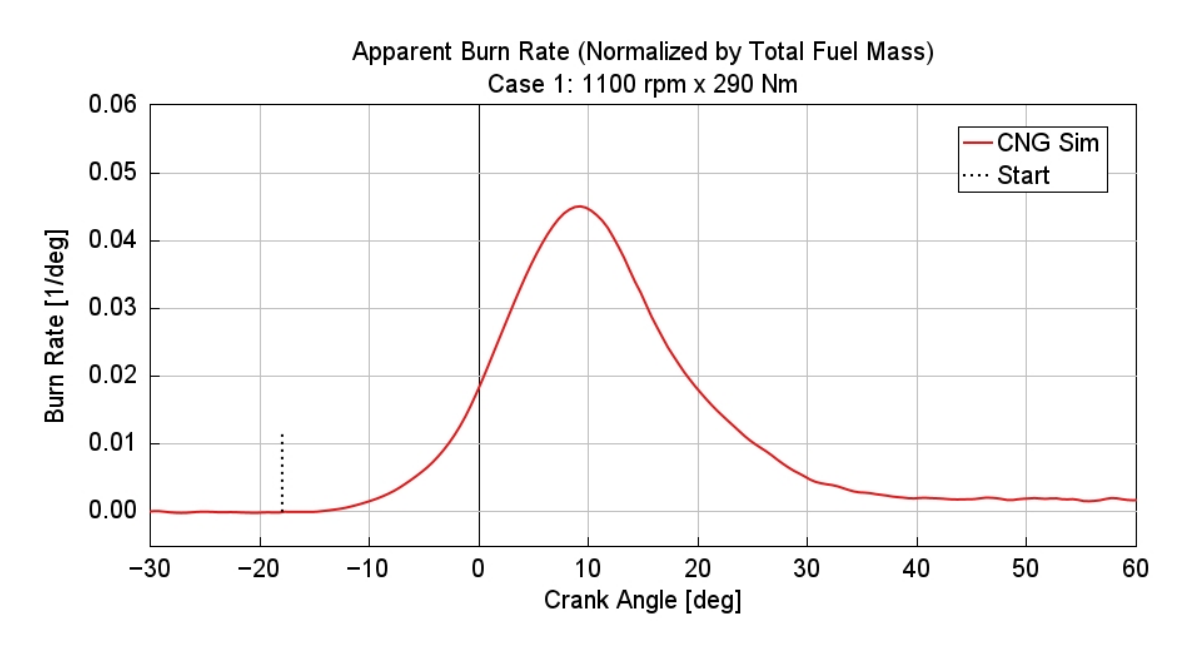


Figure 2.12: CNG Burn rate - TPA combustion model (C1)

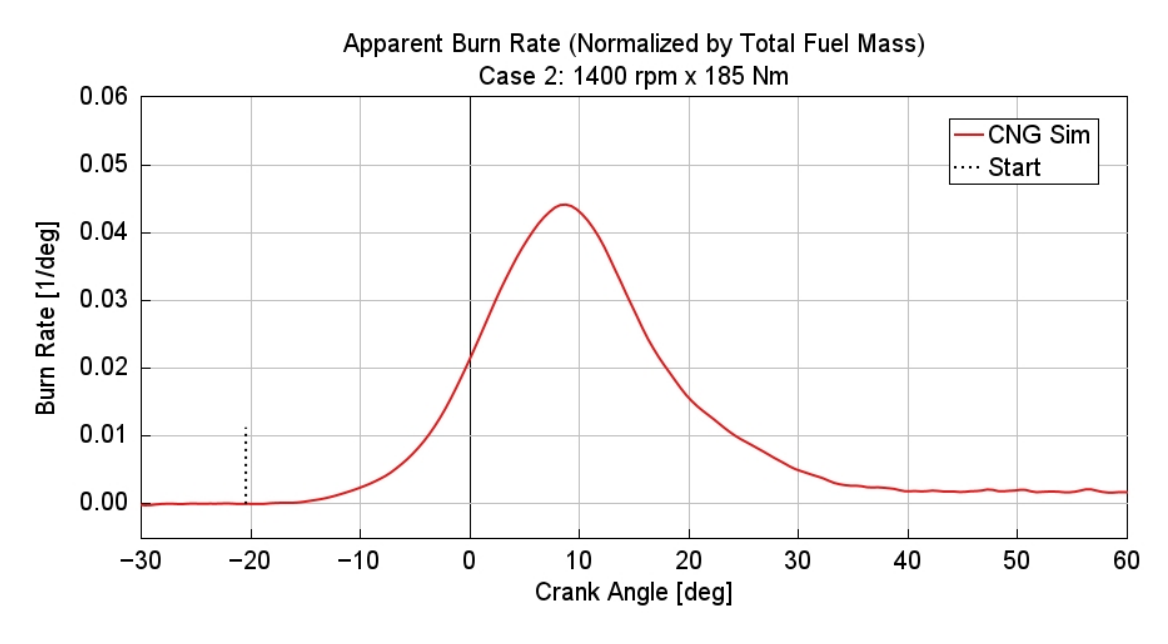


Figure 2.13: CNG Burn rate - TPA combustion model (C2)

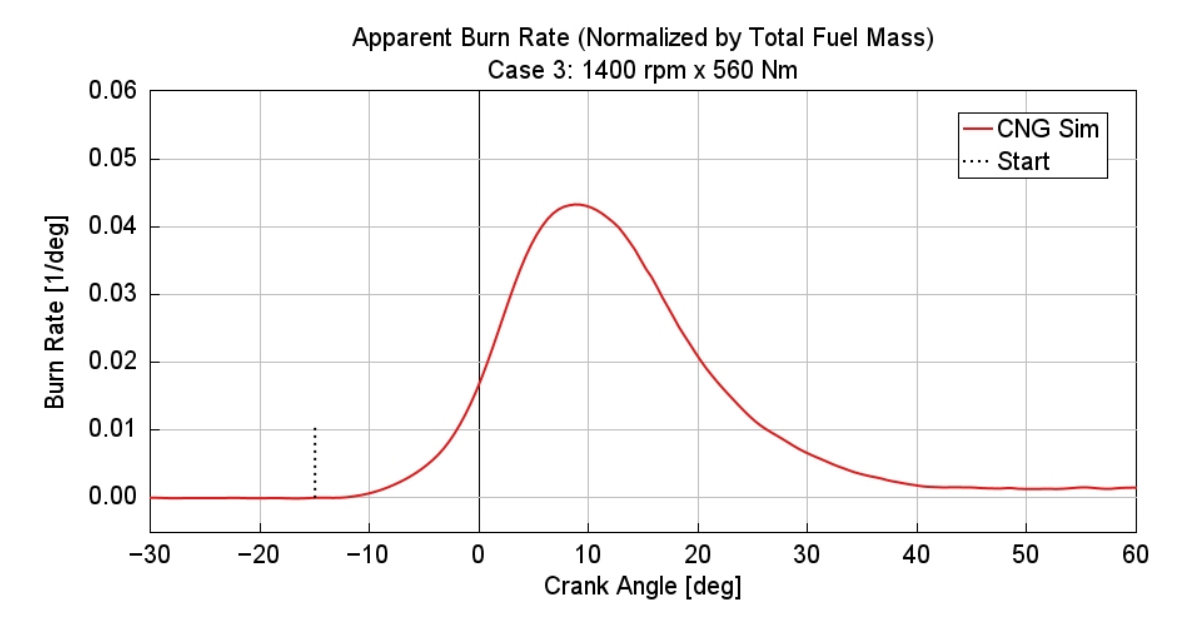


Figure 2.14: CNG Burn rate - TPA combustion model (C3)

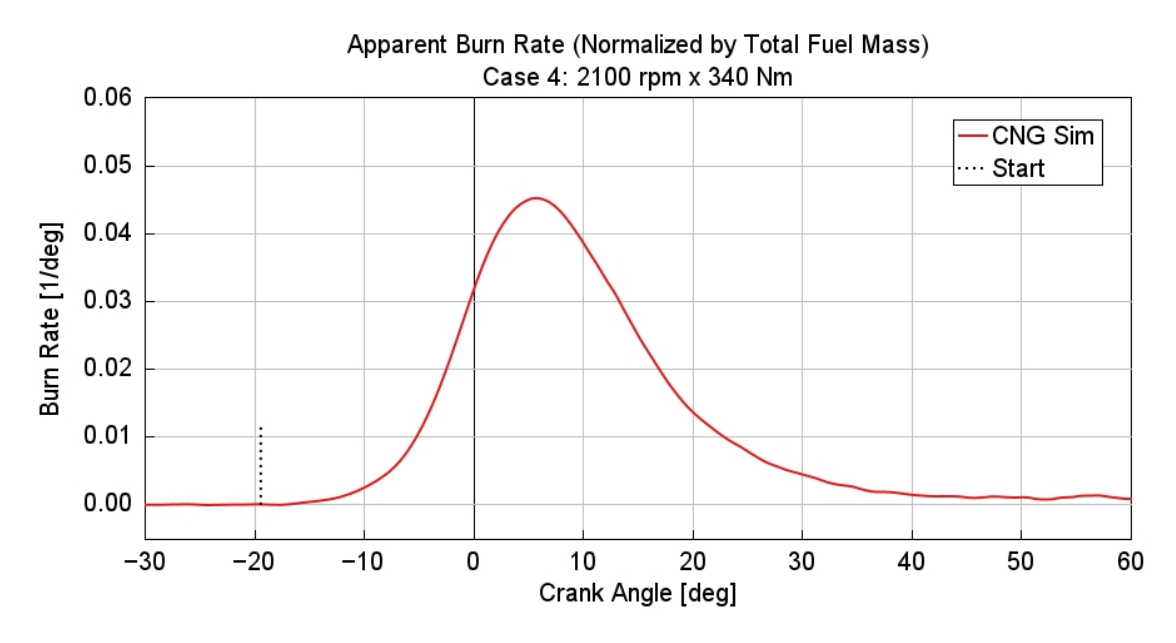


Figure 2.15: CNG Burn rate - TPA combustion model (C4)

These plots clearly show that the calculated burn rate reproduces a realistic and coherent combustion evolution, consistent with experimental observations. Overall, the results validate the TPA approach as a reliable tool for the parametrisation of the burn rate, which will be imposed as a combustion object for all future analysis to ensure a realistic model of the real engine.

# 2.4 Development of the predictive SI-TURB combustion model

The predictive combustion model aims to reproduce the fundamental physical phenomena of the combustion process to predict the burn rate. The objective is to identify a set of model constants that provides the best possible agreement with different engine operating points. The SI-TURB calibration process is structured in five main phases:

- Model creation and validation. At the beginning, a non-predictive combustion model (usually a Wiebe function) is implemented. This step is essential to obtain reliable inputs for CFD simulations of the in-cylinder turbulence. The non-predictive model represents the starting point of the calibration process, and therefore requires a high level of fidelity. This validated engine model with imposed combustion is then used as the basis for building the predictive one by replacing the combustion object and introducing the turbulence model.
- Turbulence parameters calibration. The four turbulence parameters are calibrated by matching the turbulent kinetic energy, the normalised turbulent length scale, and the tumble number obtained in GT-POWER with those provided by CFD simulations. This step can be performed using the previously described Three Pressure Analysis (TPA).
- Evaluation of initial in-cylinder conditions. This task is performed either with a mono-cylinder model combined with TPA or using the outputs of the detailed engine model with imposed combustion.
- Combustion calibration. At this step, the combustion constants are tuned. The calibration can be performed using either a Design of Experiments (DOE) approach or the Advanced Optimisation tool. Both methods are used to refine the model constants that govern the combustion process.
- Full engine simulation. Finally, the complete engine model is run with the SI-TURB predictive combustion model. At this point, the predictive capability of the model can be assessed, taking into account the cylinder's geometry, spark plug locations and timing, air motion, and fuel properties.

With regard to model requirements, the predictive SI-TURB approach relies on measurement data, turbulence measurements from 3D CFD simulations, and a geometrical description of the combustion chamber. A minimum of 25 operating points, spread across the entire normal operating range, is required to ensure proper calibration.

The turbulence profiles required for calibration are: tumble, turbulence length scale, swirl, and turbulence strength.

For this project, the 3D-CFD data were already available at the CNR-STEMS institute.

Figures 2.16 report the evolution of these quantities. For simplicity, only the turbulence profiles corresponding to operating point **C1** are shown.

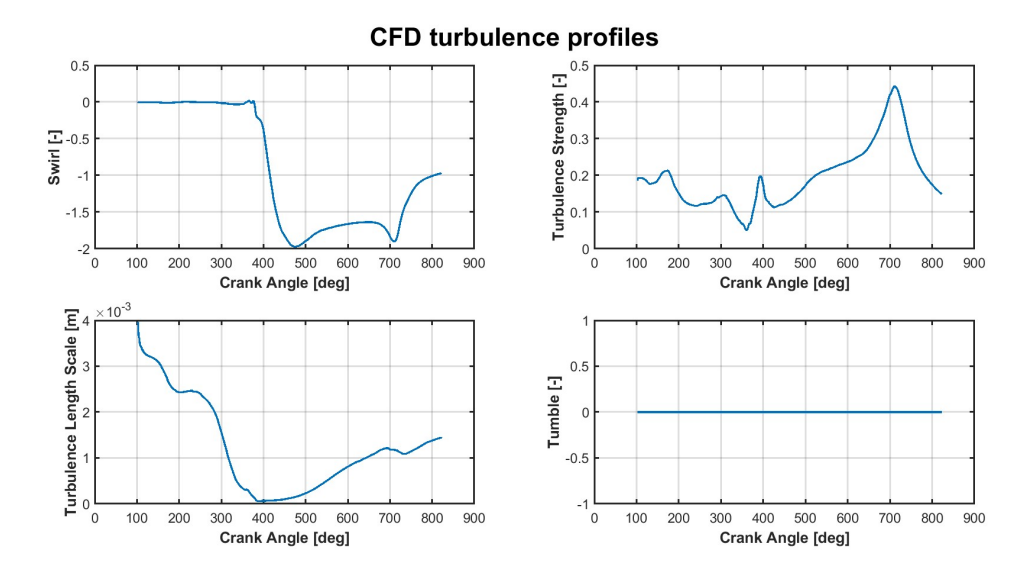


Figure 2.16: CFD turbulence profiles (C1)

As can be observed, the tumble profile remains close to zero, while the turbulence strength has been normalised with respect to the average piston speed and is therefore dimensionless.

As previously discussed, the combustion development within SI-TURB is governed by the variation of four model constants, which are:

- **Dilution effect multiplier (DEM)**. Scales the effect of dilution (residual and EGR) on the laminar speed.
- Flame kernel growth multiplier  $(C_k)$ . Adjust the calculated growth rate of the flame kernel. This variable influences the ignition delay: larger values reduce the delay, advancing the transition from laminar to turbulent combustion.
- Turbulent flame speed multiplier ( $C_s$ ). Scales the calculated turbulent flame speed. It influences the overall duration of the combustion: larger values increase the speed of combustion.
- Taylor length scale multiplier  $(C_{\lambda})$ . Modifies the calculated Taylor microscale of turbulence. The Taylor microscale modified the time constant of combustion of the fuel/air mixture entrained into the flame zone by changing the thickness of the plume.

These four model parameters describe all the physics behind the combustion process in GT-POWER. The combustion process can be represented through the entrainment of the unburned mixture into the flame front and its subsequent conversion into burned gases. The model relies on two variables: the laminar flame speed  $S_L$ , which characterizes the chemical reactivity of the fresh mixture, and the turbulent flame speed  $S_T$ , which accounts for the influence of turbulence on flame propagation. The flame laminar speed  $S_L$  is modeled as:

$$S_L = \left(B_m \phi^{\eta} e^{-\zeta(\phi - \phi_m)^2}\right) \left(\frac{T_u}{T_0}\right)^{\alpha} \left(\frac{p}{p_0}\right)^{\beta} f(\text{Dilution})$$
 (2.4)

where:

- $B_m$  = maximum laminar flame speed,
- $\phi$  = in-cylinder equivalence ratio,
- $\phi_m$  = equivalence ratio at which  $S_L$  is maximum,
- $\eta$  = equivalence ratio exponent,
- $\zeta$  = laminar speed exponent,
- $T_u$  = temperature of the unburned mixture,
- p = in-cylinder pressure,
- $T_0$ ,  $p_0$  = reference values for temperature and pressure.

The enhancement of the flame propagation due to turbulence is expressed through the turbulent flame speed:

$$S_T = C_s u' \left( 1 - \frac{1}{1 + \frac{C_k R_f^2}{L_t^2}} \right)$$
 (2.5)

where:

- u' is the turbulent velocity fluctuation,
- $R_f$  the flame radius,
- $L_t$  the turbulent length scale,

Once both laminar and turbulent contributions are defined, the governing equations of the entrainment model can be written as:

$$\frac{dM_e}{dt} = \rho_u A_e (S_T + S_L) \tag{2.6}$$

$$\frac{dM_b}{dt} = \frac{M_e - M_b}{\tau} \tag{2.7}$$

where:

- $M_e$  = mass entrained into the flame front,
- $M_b$  = mass already burned,
- $\rho_u$  = density of the unburned mixture,
- $A_e$  = flame surface area,
- $\tau$  = characteristic time constant.

The first equation describes the entrainment of the fresh mixture, while the second governs the rate at which entrained mass is converted into burned mass. The characteristic time  $\tau$  is derived from the turbulence theory and can be expressed as:

$$\tau = \frac{\lambda}{S_L} \tag{2.8}$$

with the Taylor microscale  $\lambda$  defined as:

$$\lambda = \frac{C_{\lambda} L_{t}}{\sqrt{Re_{t}}}, \qquad Re_{t} = \frac{\rho_{u} u' L_{t}}{\mu}$$
 (2.9)

where  $\mu$  is the dynamic viscosity of the mixture. In this formulation, the entrainment model captures the combined effect of chemical kinetics, turbulence, and dilution on the overall combustion rate.

## 2.4.1 Sensitivity analysis of SI-TURB parameters

All these multipliers can be varied within an interval ranging from 0.5 to 3. Before performing the optimisation phase to identify the most suitable set of values, a sensitivity analysis is carried out. In this step, the value of one multiplier at a time is varied while the others are kept equal to unity, in order to evaluate its individual effect on the combustion process.

As shown in the Figures 2.17-2.18, when the lowest possible value (0.5) is applied, the dilution effect is underestimated and consequently the laminar flame speed becomes higher. This leads to a faster combustion process, which can be observed in the anticipated and

significantly increased peak pressure. The burn rate curve further confirms this behaviour, showing a steeper slope, an anticipated phasing, and a peak value that is almost doubled. Increasing the multiplier, the dilution effect becomes more pronounced. Consequently, the peak pressure decreases and the combustion phasing shifts toward higher crank angles. This behaviour is due to the stronger dilution, which slows down the combustion process, although the results still do not converge to the reference values. For very high values (above 2.5), the opposite trend is observed. In this condition, the dilution effect is excessive, leading to a strong reduction in the available oxygen within the chamber. As a result, the laminar flame speed decreases significantly and the combustion is severely penalised. The pressure and burn rate traces no longer show the typical rise caused by heat release, suggesting an almost absent or extremely incomplete combustion. This behaviour can be recognised in the pink curves, which practically follow the motored pressure trace.

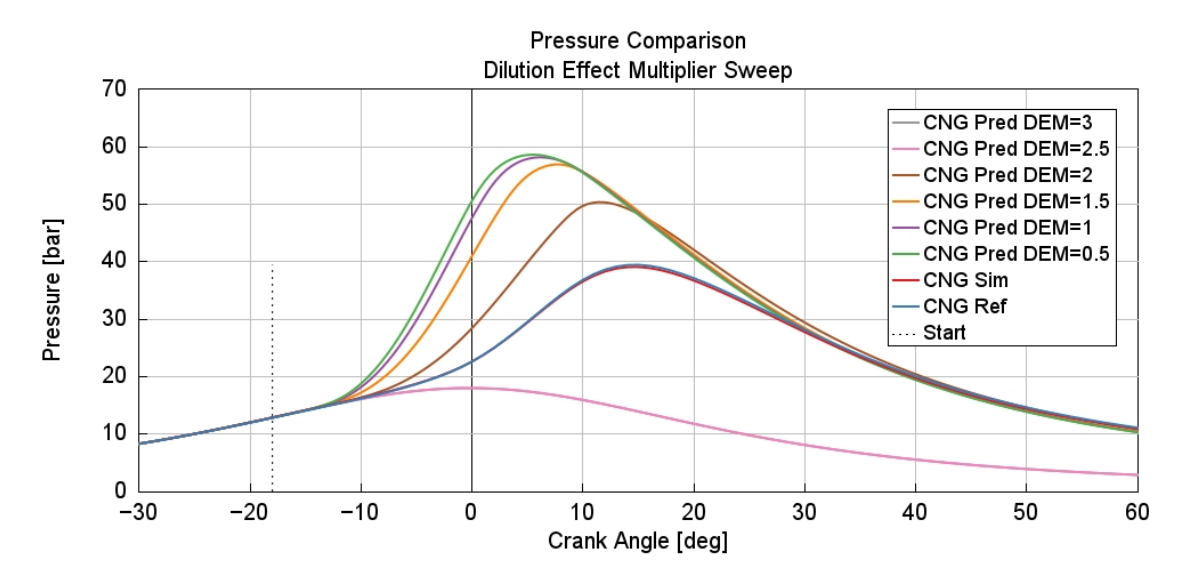


Figure 2.17: CNG In-cylinder pressure - SI-TURB combustion model - DEM sweep

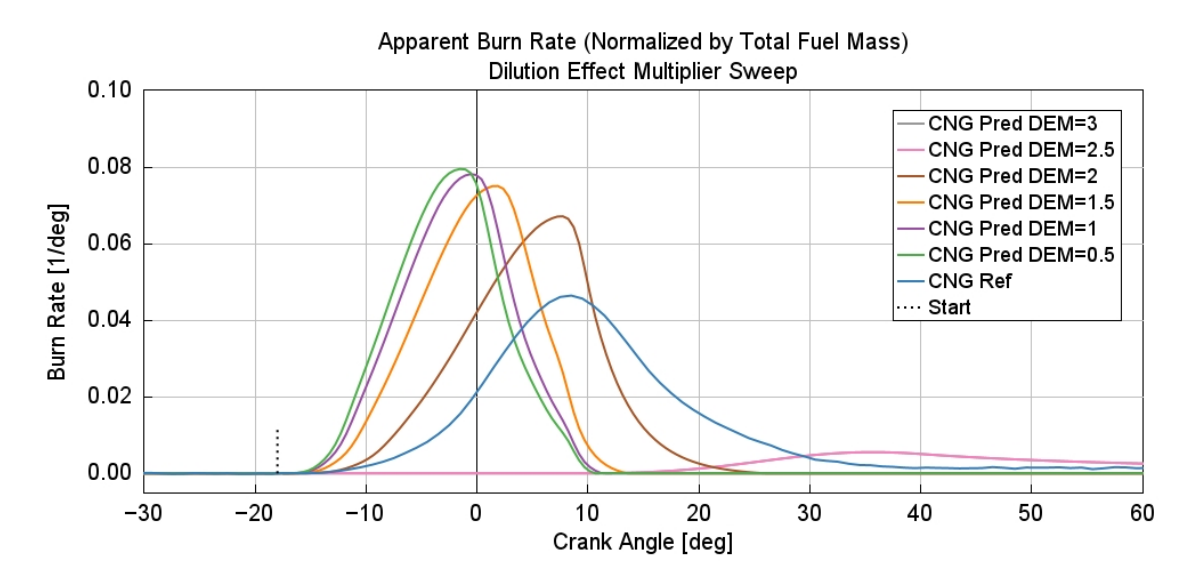


Figure 2.18: CNG Burn rate - SI-TURB combustion model - DEM sweep

Looking at Figures 2.19-2.20, a consistent trend can be observed for all the values of the flame kernel multiplier. The in-cylinder pressure shows a peak value that is both higher and more advanced, and the same effect is reflected in the burn rate curve. Unlike the behaviour observed with the previous multiplier, in this case, no significant differences are noticeable when varying the value of the multiplier.

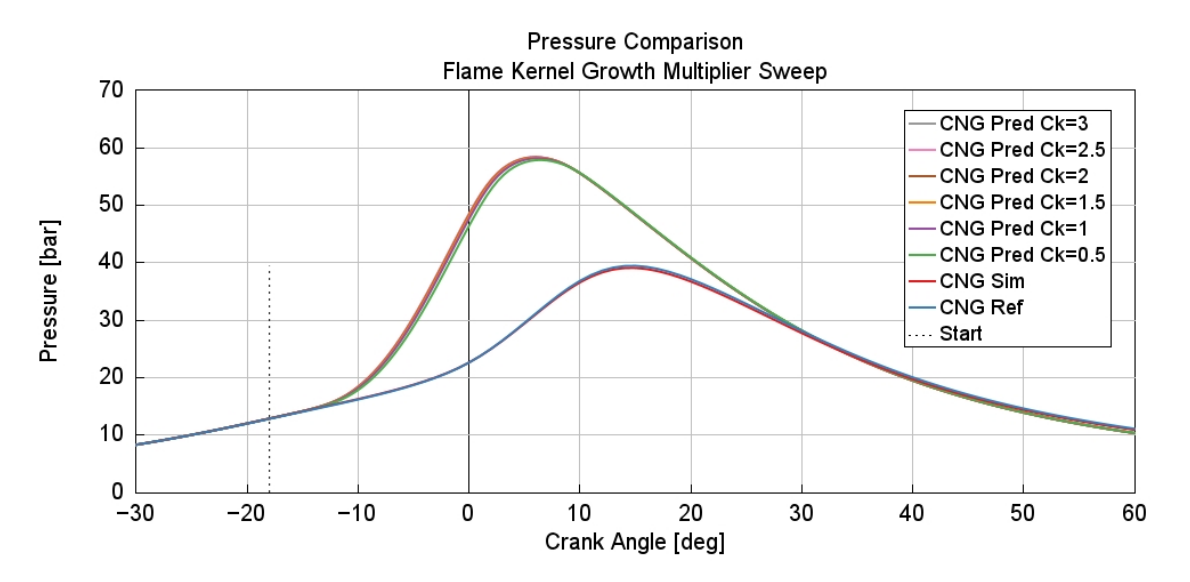


Figure 2.19: CNG In-cylinder pressure - SI-TURB combustion model -  $C_k$  sweep

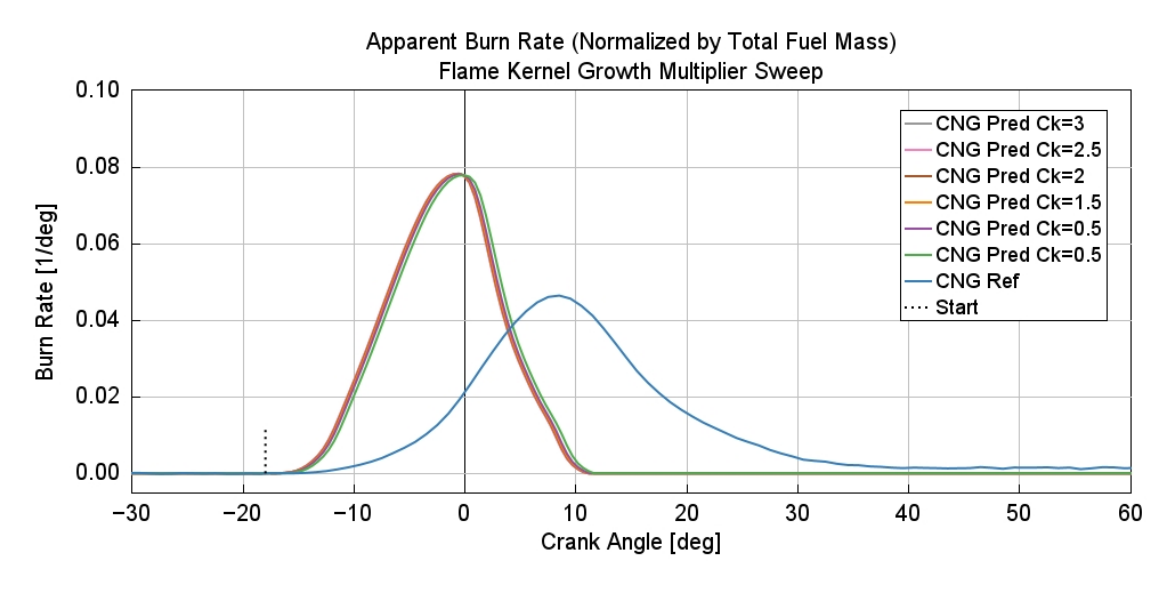


Figure 2.20: CNG Burn rate - SI-TURB combustion model -  $C_k$  sweep

As can be observed from Graphs 2.21-2.22, increasing the turbulent flame speed multiplier leads to a higher flame propagation velocity. This results in a progressive rise and an earlier occurrence of the in-cylinder pressure peak. A similar behaviour can be noticed in the burn rate curve, which becomes sharper and more pronounced, with steeper slopes during the ascending and descending phases. This phenomenon is because, as the flame speed increases, combustion is completed more rapidly, concentrating the neat release

within a shorter crank angle interval. Consequently, the maximum pressure is reached earlier and with a higher intensity.

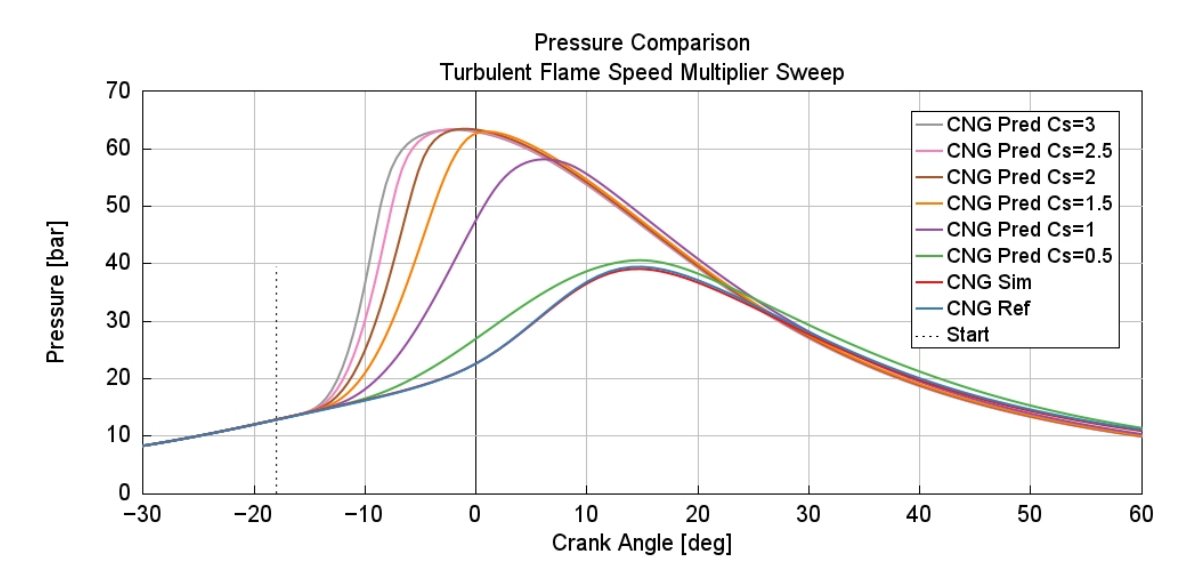


Figure 2.21: CNG In-cylinder pressure - SI-TURB combustion model -  $C_s$  sweep

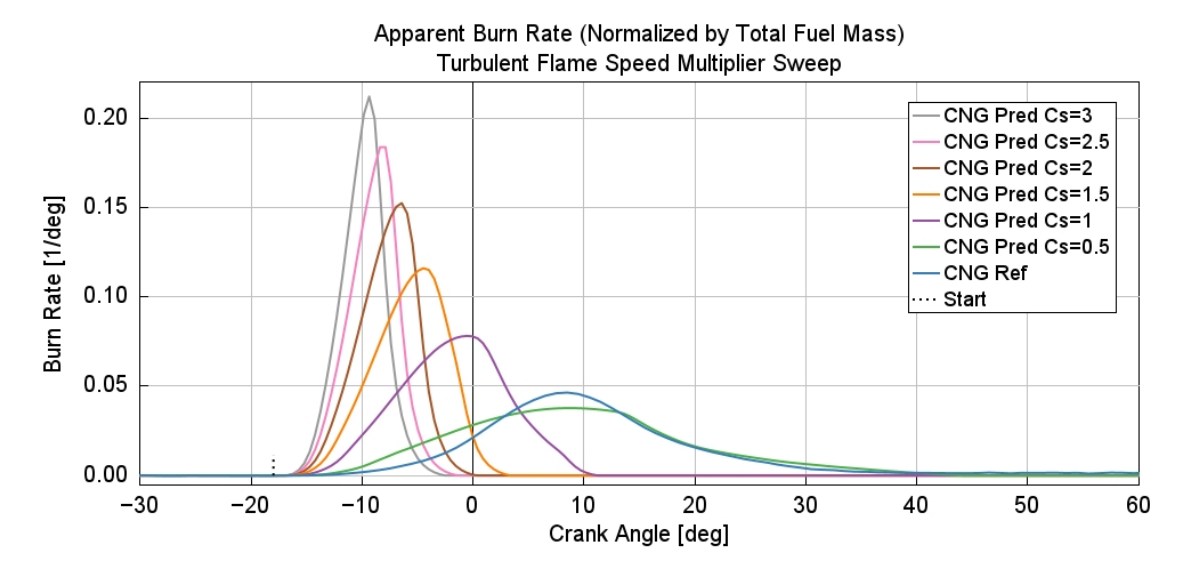


Figure 2.22: CNG Burn rate - SI-TURB combustion model -  $C_s$  sweep

Looking at the Graphs 2.23-2.24, relative to the Taylor length scale multiplier sweep, the effect of this parameter can be clearly observed. When a low value is imposed, in-cylinder pressure reaches a higher and more advanced peak, while the burn rate curve also appears anticipated and with a higher maximum value. This behaviour is explained by the fact that a smaller Taylor length scale corresponds to more intense small scale turbulence, which increases the wrinkling of the flame front. As a result, the effective combustion surface is enlarged, leading to a faster energy release. Conversely, when the Taylor length scale multiplier is increased, the influence of turbulence is reduced. The combustion process slows down, the burn rate curve exhibits lower and less advanced peaks, and the

in-cylinder pressure reaches a lower maximum value, shifted towards later crank angles.

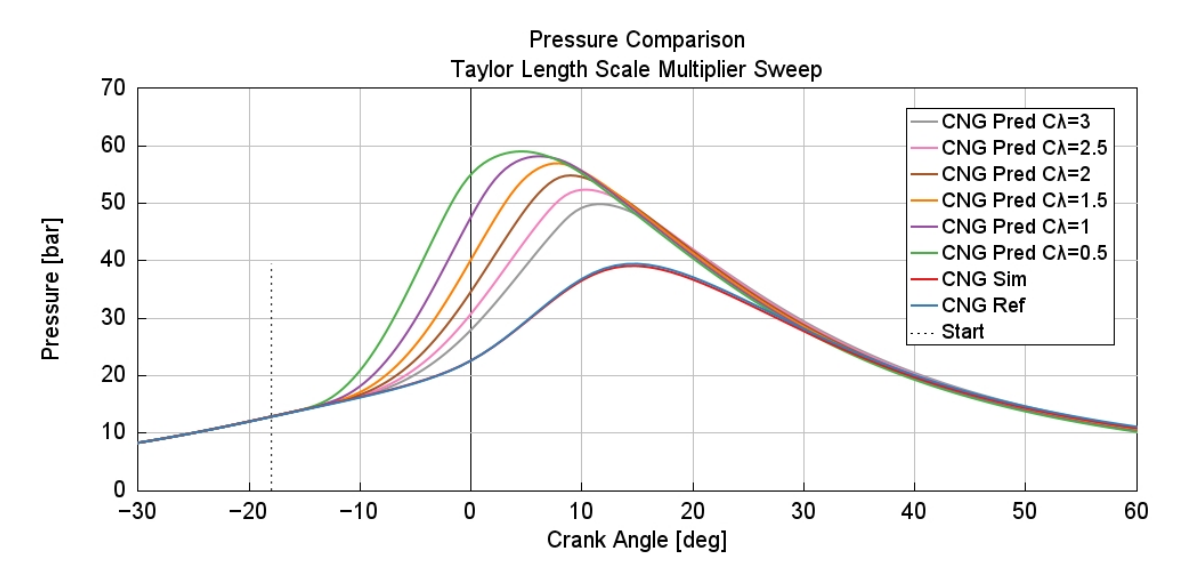


Figure 2.23: CNG In-cylinder pressure - SI-TURB combustion model -  $C_{\lambda}$  sweep

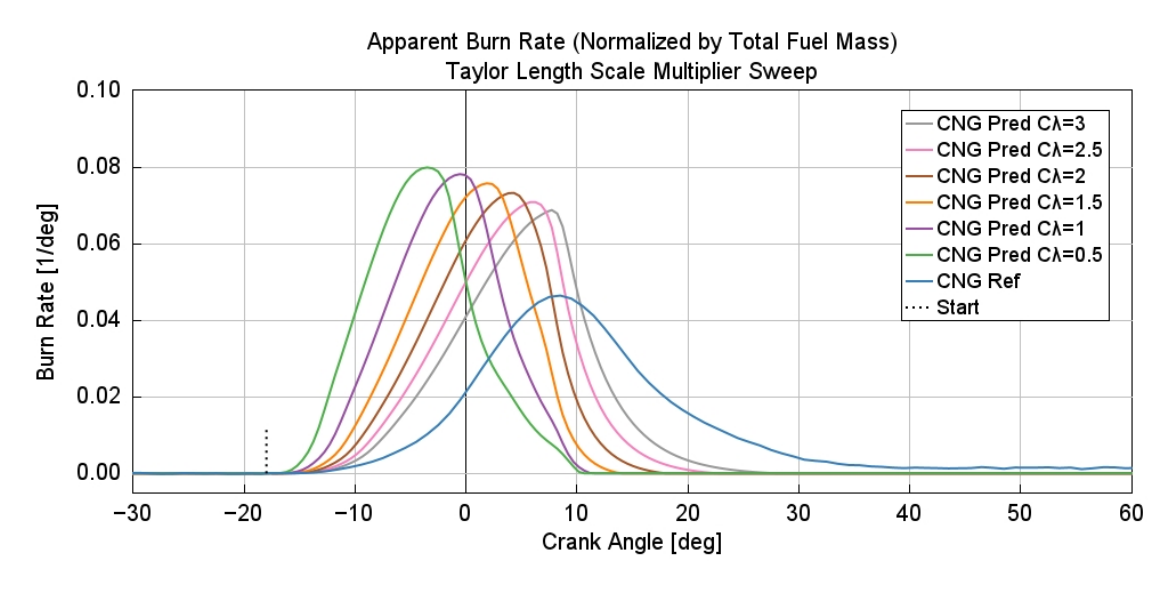


Figure 2.24: CNG Burn rate - SI-TURB combustion model -  $C_{\lambda}$  sweep

## 2.4.2 SI-TURB model optimisation

After completing the sensitivity analysis, the tuning of the four multipliers can be carried out to reproduce the real burn rate of the model. The optimisation process was investigated through both the Design of Experiment (DOE) approach and the Advanced Optimisation method, which are both available within the software.

#### Design of Experiment (DOE) analysis

The Design of Experiment (DOE) technique is a method that allows a systematic evaluation of the influence of multiple input parameters varied simultaneously, avoiding varying

one factor at a time. For the implementation of this analysis, it was necessary to define both the minimum and the maximum value that each multiplier can assume, as well as the number of levels into which the interval is divided, as shown in Figure 2.25.

Design of Experiments								
Parameter	Unit	Description	Min	Max	# of Levels			
Dilution_Exp_Mult (DOE)		Dilution Effect Multiplier	0.5	3.0	5			
Flame_Kernel_Mult (DOE)		Flame Kernel Growth Multiplier	0.5	3.0	5			
Turb_Flame_Speed_Mult (		Turbulent Flame Speed Multiplier	0.5	3.0	5			
Taylor_Length_Scale_Mult		Taylor Length Scale Multiplier	0.5	3.0	5			

Figure 2.25: DOE analysis setup - SI-TURB combustion model

By doing this, the software automatically calculates a constant increment between each value, ensuring that the interval is properly divided into a specific number of levels. In this case, with an interval ranging from 0.5 to 3 and five imposed levels, each step corresponds to an increment of 0.625. Although the number of levels can be further increased, this would significantly raise the computational effort and lead to excessively long analysis times. This procedure generates a map in which all possible combinations of multiplier values are included, resulting in 625 cases being analysed within a single run. In this way, multiple independent simulations are avoided. However, this method remains quite coarse, since multipliers are limited to discrete level values, and therefore not all possible combinations are investigated. Moreover, the time required to explore the entire design space is very high. For these reasons, this approach was not further developed, and optimisation analysis was instead preferred to identify the most appropriate parameter set.

#### **Advanced Optimization analysis**

The advanced optimisation technique is a method that allows the identification, at the end of the simulation, of the best solution for a given problem. In this case, the objective is to determine the values of the four multipliers in order to obtain a predicted burn rate profile that closely matches the real one. The optimisation process is therefore set to minimise the "Improved burn rate RMS error (Meas vs Pred)". The RMS error is a statistical index that quantifies the average deviation between the simulated and the experimental values. Since the optimisation target is the minimisation of this error applied to the burn rate, the simulation is forced to reproduce a profile that remains as close as possible to the measured one.

As shown in Figure 2.26, the analysis requires the definition of both the population size and the number of generations. The total number of designs evaluated by the optimiser corresponds to the product of these two values. Furthermore, the parameters to be varied must be specified, together with their allowed variation range.

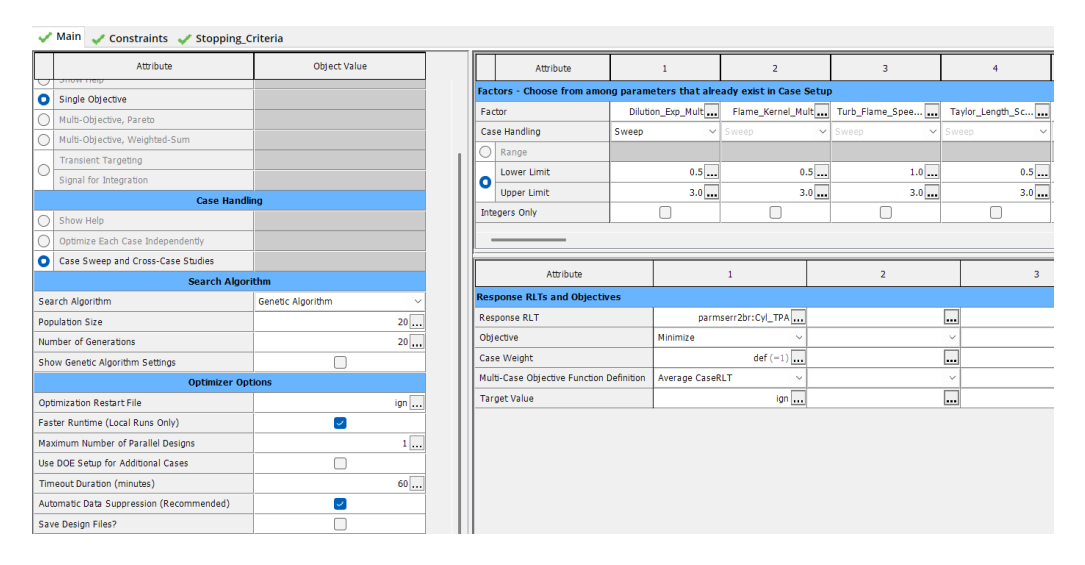


Figure 2.26: Advanced optimiser setup - SI-TURB combustion model

The optimisation process was carried out in two stages. The first aimed at identifying a single set of parameters applicable to all operating points, while the second focused on performing the optimisation for each operating point individually. This latter approach resulted in four different parameter sets, each one specifically tuned for its corresponding operating condition.

The first optimisation phase proved to be highly demanding and difficult to complete. Identifying a single set of parameter values that could be applied to all the analysed engine operating points, was not simple. Approximately 20 different optimisation simulations were carried out, modifying both the population size and the number of generations each time to obtain increasingly accurate results. The simulation presented below, including the figures and the resulting multiplier values, is the one that provided the best overall approximation across all operating points.

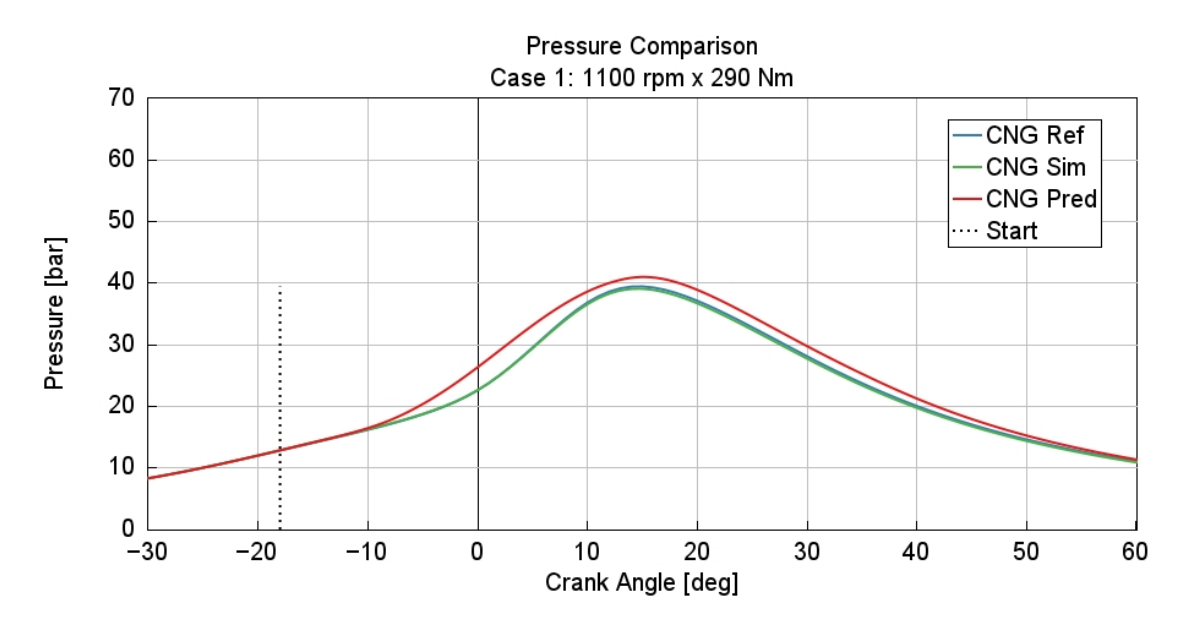


Figure 2.27: CNG In-cylinder pressure - Global SI-TURB combustion model (C1)

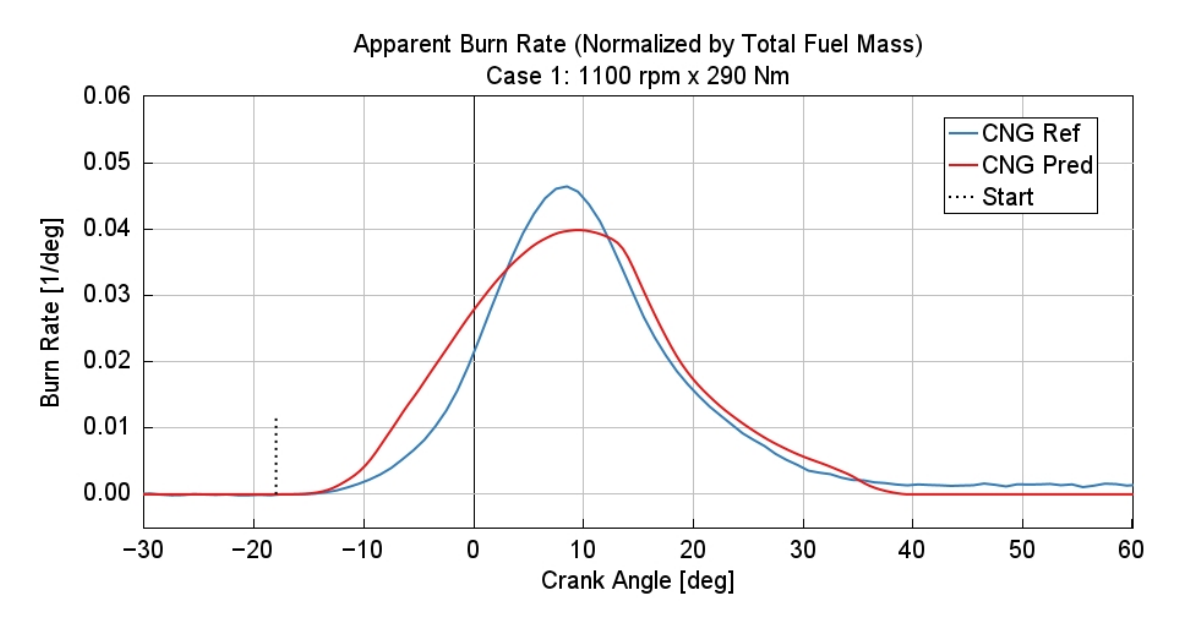


Figure 2.28: CNG Burn rate – Global SI-TURB combustion model (C1)

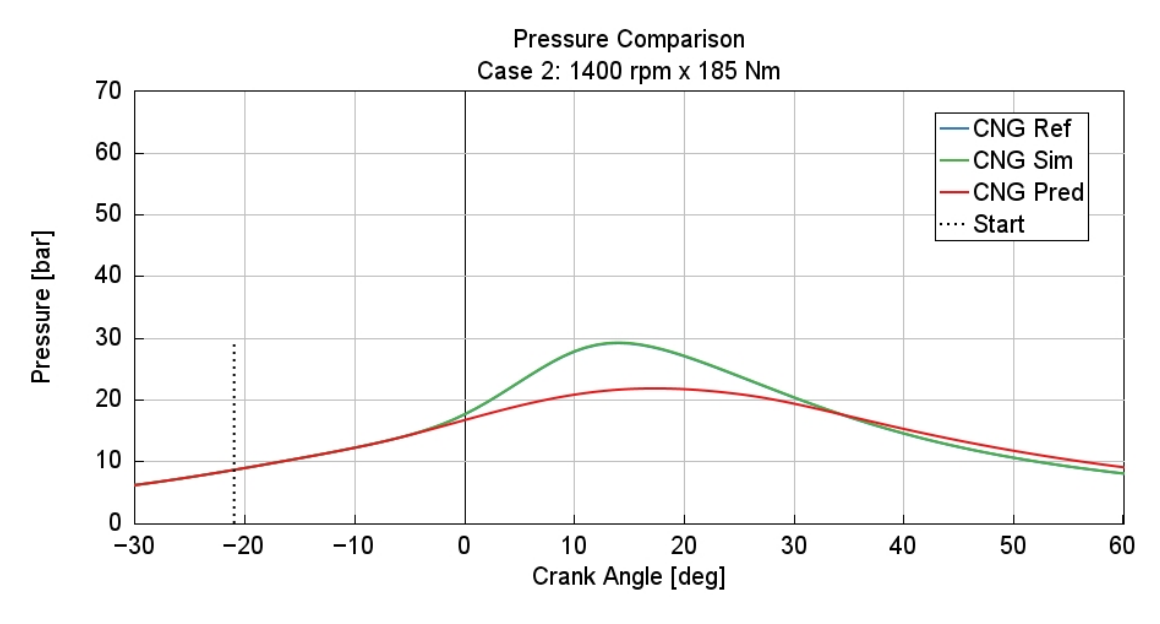


Figure 2.29: CNG In-cylinder pressure – Global SI-TURB combustion model (C2)

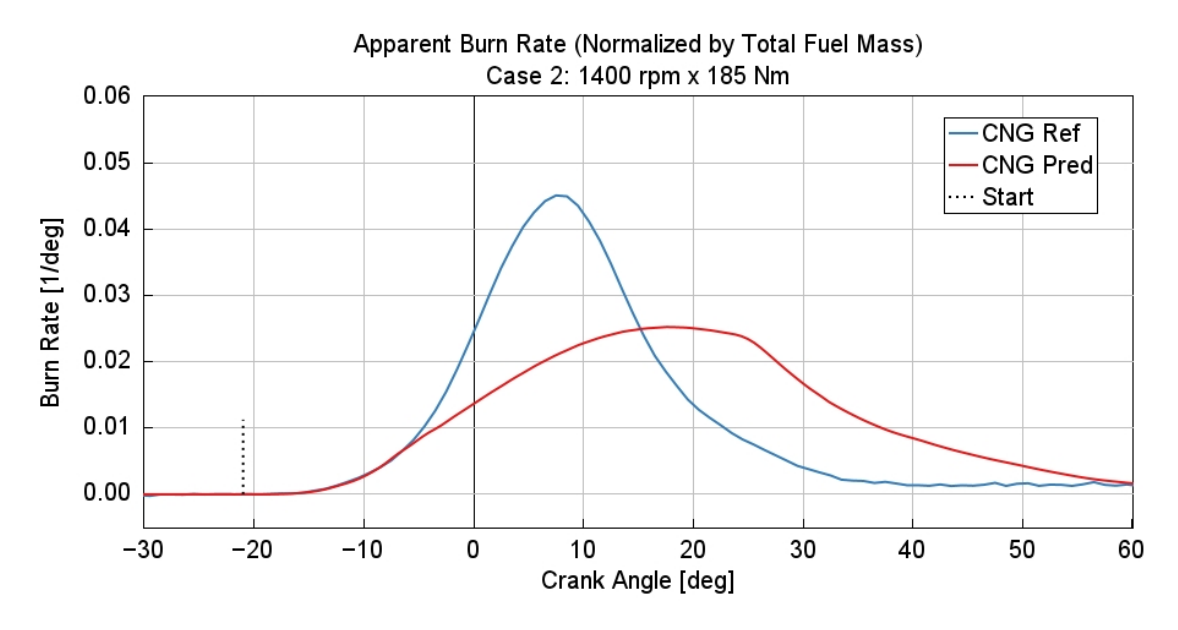


Figure 2.30: CNG Burn rate - Global SI-TURB combustion model (C2)

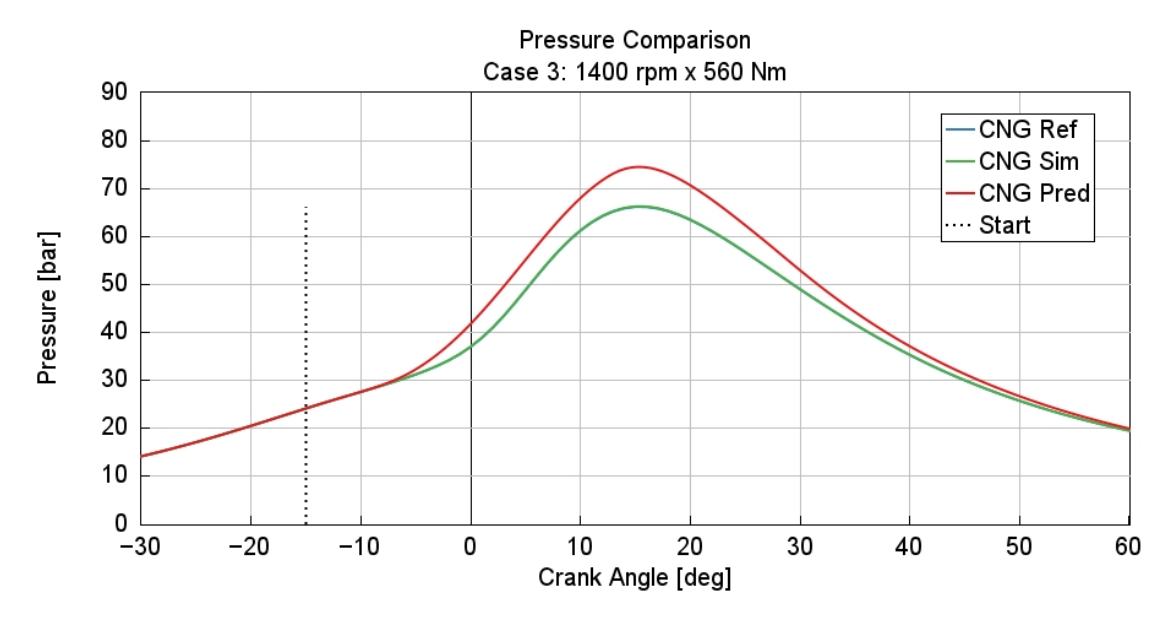


Figure 2.31: CNG In-cylinder pressure - Global SI-TURB combustion model (C3)

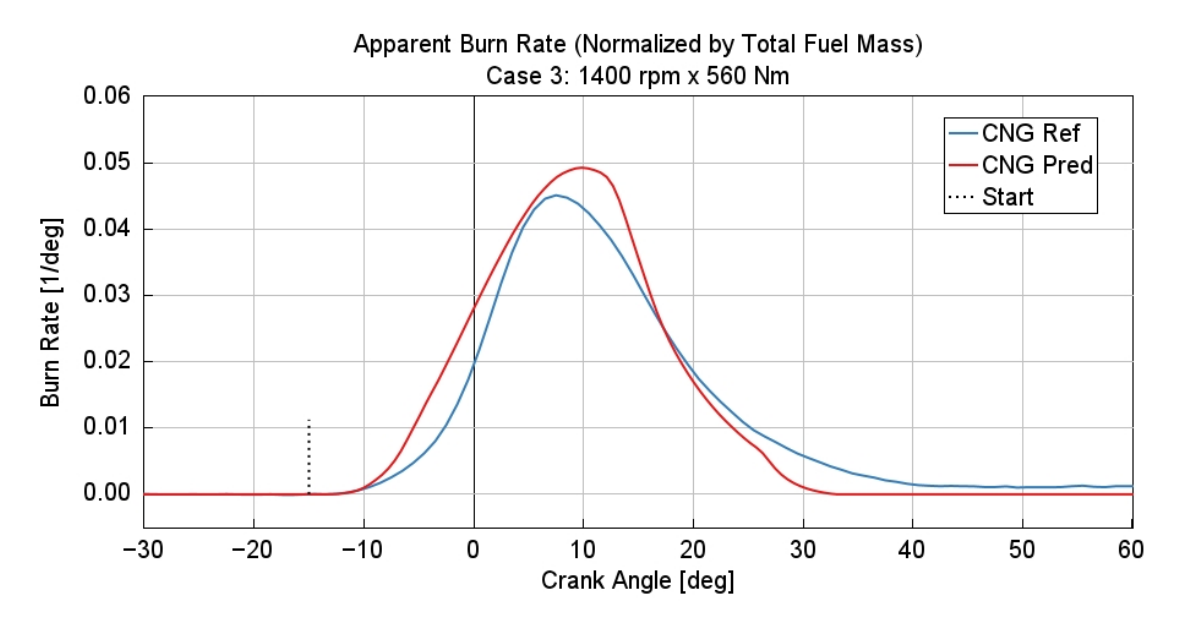


Figure 2.32: CNG Burn rate - Global SI-TURB combustion model (C3)

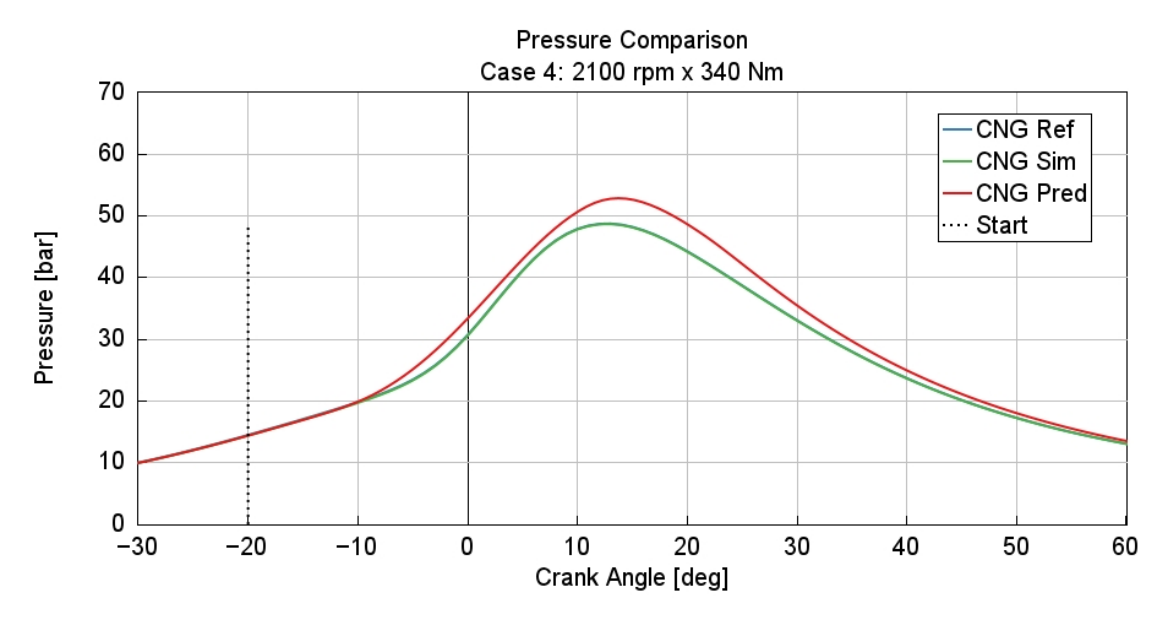


Figure 2.33: CNG In-cylinder pressure - Global SI-TURB combustion model (C4)

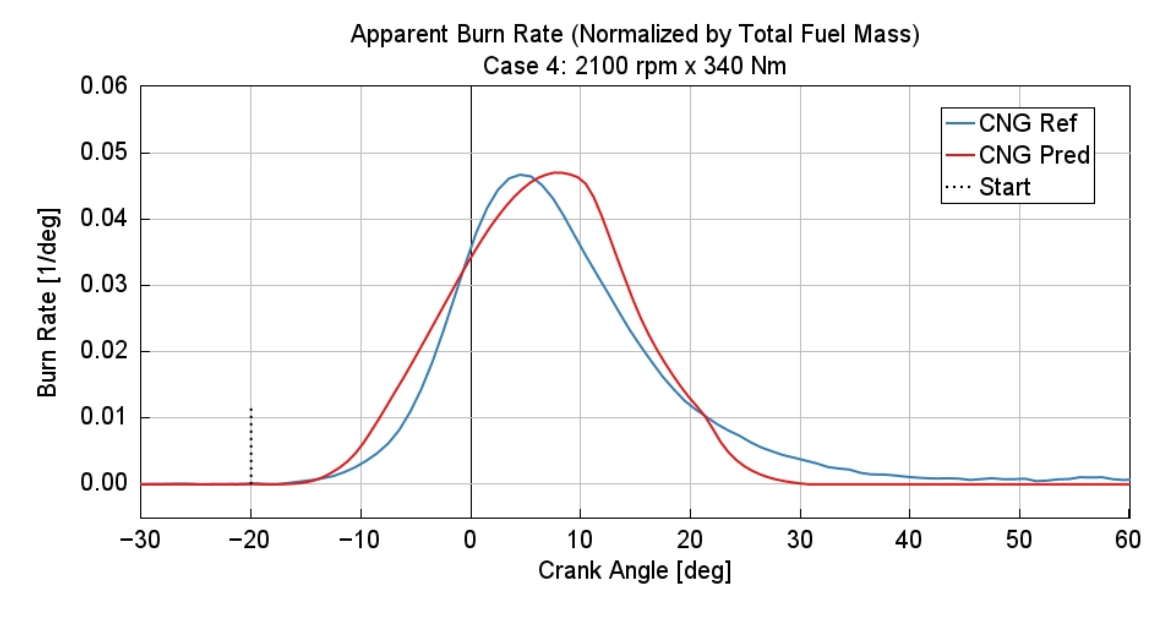


Figure 2.34: CNG Burn rate - Global SI-TURB combustion model (C4)

The set of parameters obtained is reported in Table 2.5.

	DEM [-]	C <sub>k</sub> [-]	C <sub>s</sub> [-]	$C_{\lambda}$
Parameters	0.5489953	0.6165787	0.5124251	1.2741382

Table 2.5: SI-TURB multiplier values global optimisation

As can be observed, performing this type of analysis with only four operating points resulted in poor outcomes. The predicted burn rate does not reproduce the reference profile satisfactorily for any of the operating points. For cases C1, C3, and C4, the predicted burn rate trends and peak values are inaccurate and deviate significantly from the reference, though still within a recognisable range. In contrast, for case C2, the predicted burn rate is completely inconsistent, failing to match the reference profile at any point. This difference is also evident in the corresponding in-cylinder pressure trace, which shows a markedly different behaviour.

To obtain a single parameter set that can be applied across multiple engine operating conditions, the optimisation must be performed on a significantly larger dataset, covering at least 25 operating points. This would allow the calibration to account for a wider range of conditions, improving the robustness and general validity of the optimised parameters. Since the first optimisation approach did not provide satisfactory results, a second phase was carried out. In this phase, each operating point was optimised individually, obtaining a specific set of multipliers for every operating condition, as reported in Table 2.6.

	DEM [-]	C <sub>k</sub> [-]	$C_s$ [-]	$C_{\lambda}$
C1	2.0295782	1.8639591	1.2983342	2.2651818
C2	2.2003129	2.1532888	2.2062242	1.3991231
C3	2.6834200	1.4104100	1.5935240	2.7490460
C4	2.2115500	1.5961670	1.3831430	2.2771890

Table 2.6: SI-TURB multiplier values single case optimisation

The corresponding results are illustrated in the figures below.

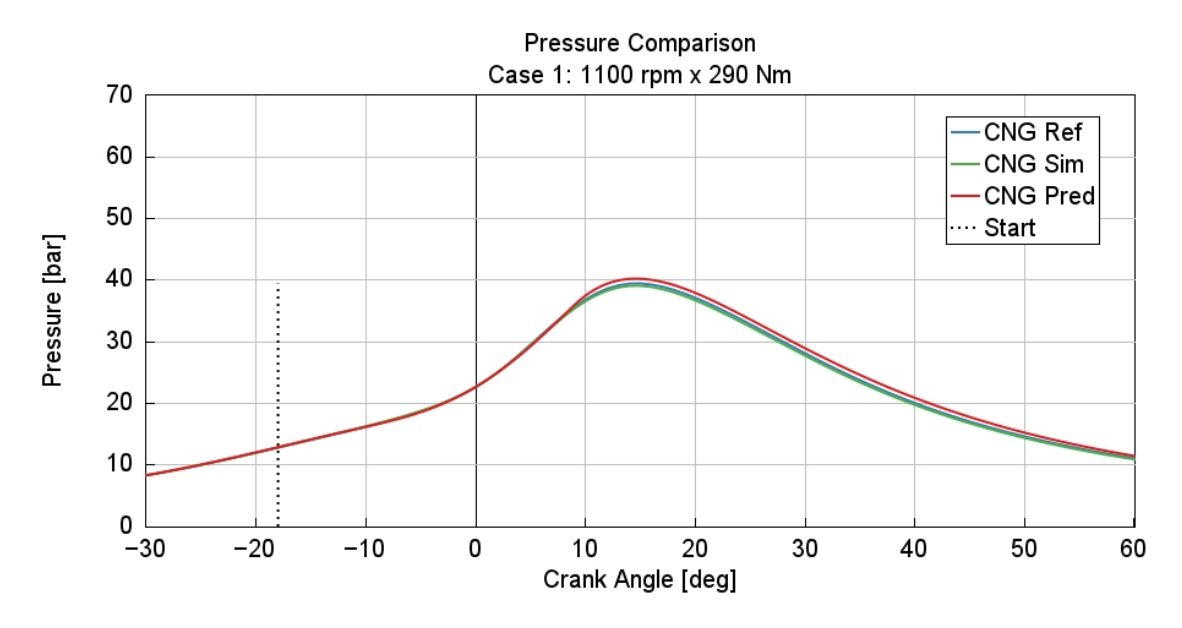


Figure 2.35: CNG In-cylinder pressure - Single case SI-TURB combustion model (C1)

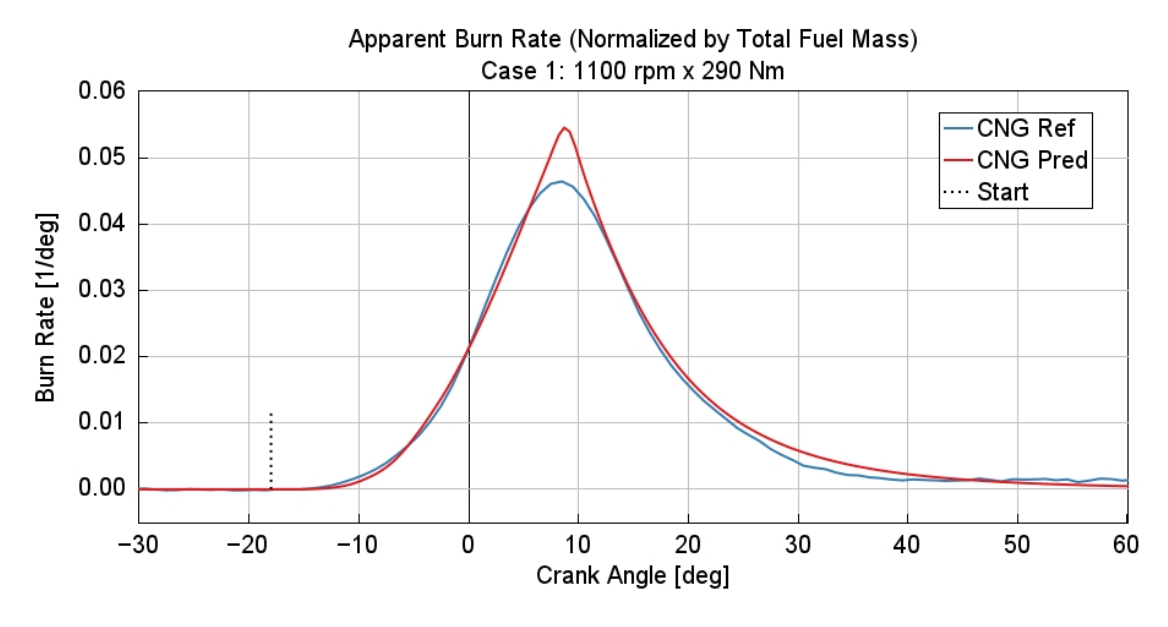


Figure 2.36: CNG Burn rate - Single case SI-TURB combustion model (C1)

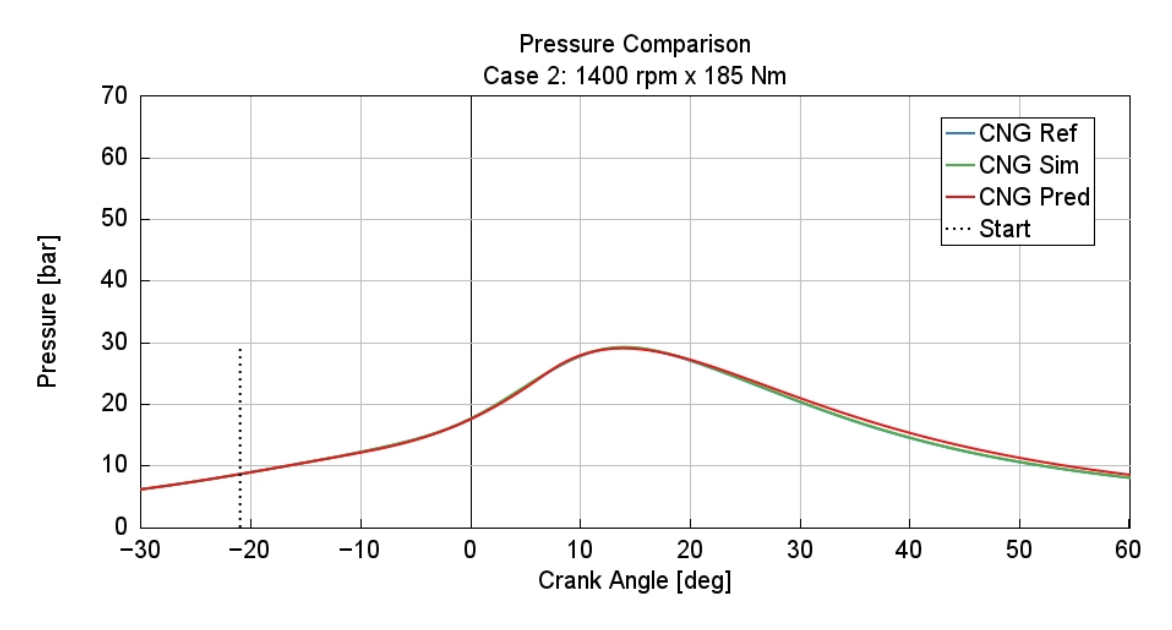


Figure 2.37: CNG In-cylinder pressure - Single case SI-TURB combustion model (C2)

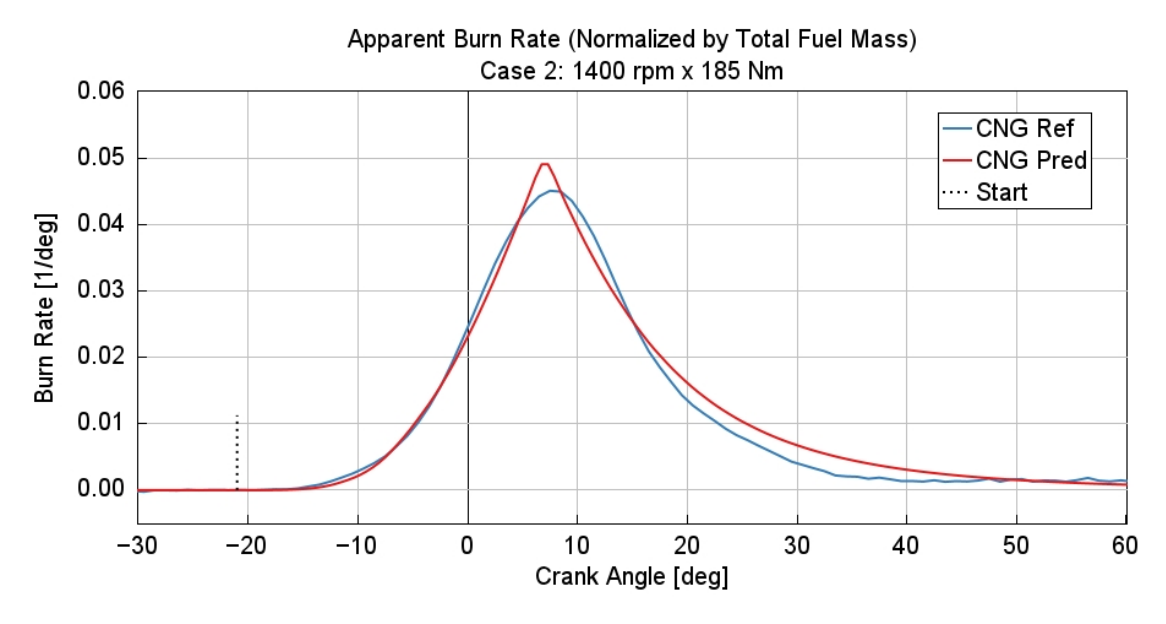


Figure 2.38: CNG Burn rate - Single case SI-TURB combustion model (C2)

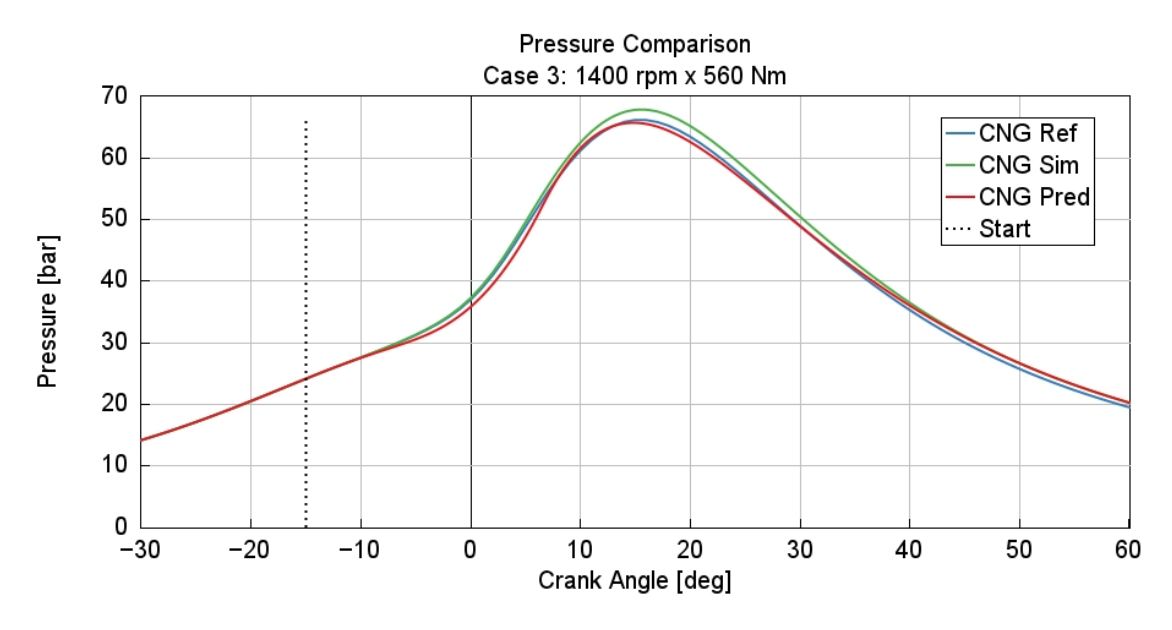


Figure 2.39: CNG In-cylinder pressure - Single case SI-TURB combustion model (C3)

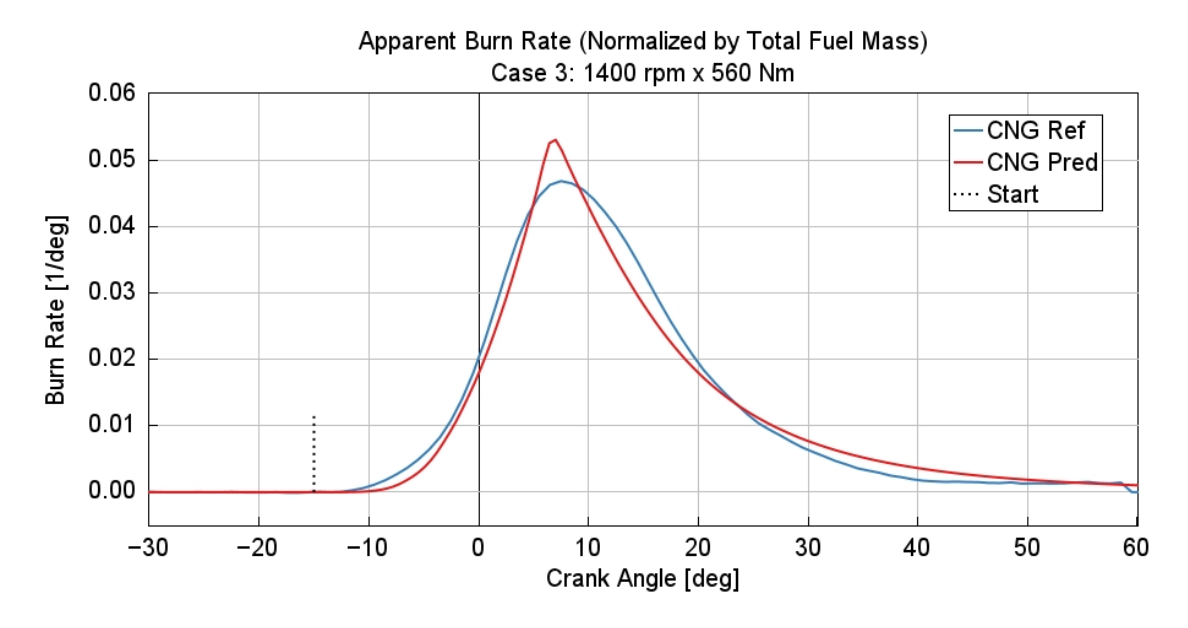


Figure 2.40: CNG Burn rate - Single case SI-TURB combustion model (C3)

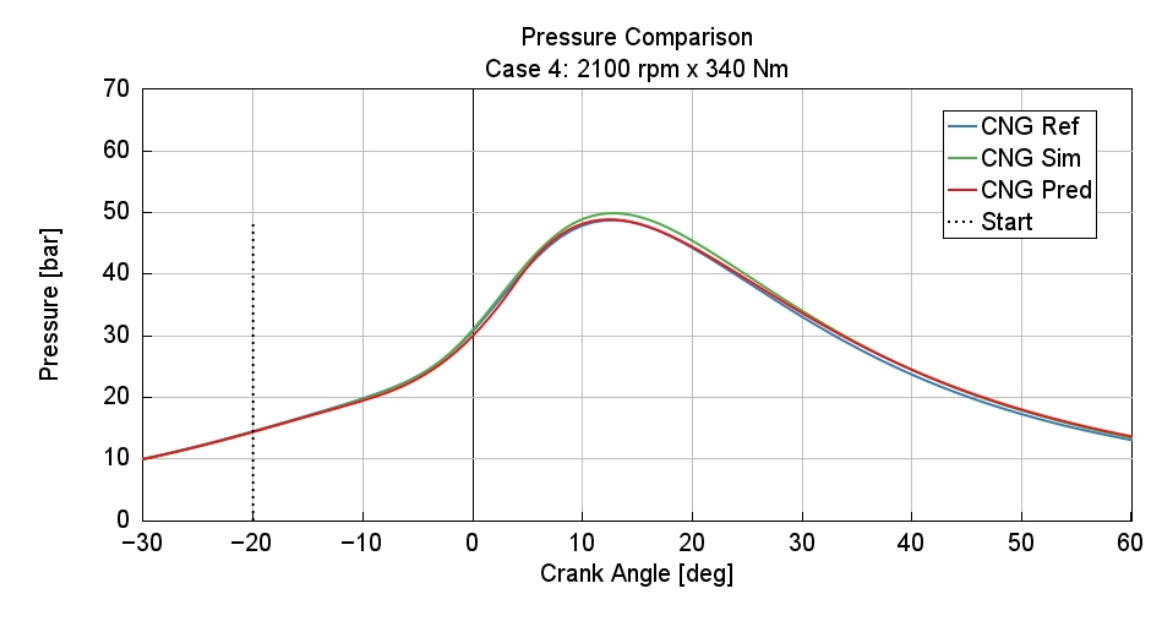


Figure 2.41: CNG In-cylinder pressure - Single case SI-TURB combustion model (C4)

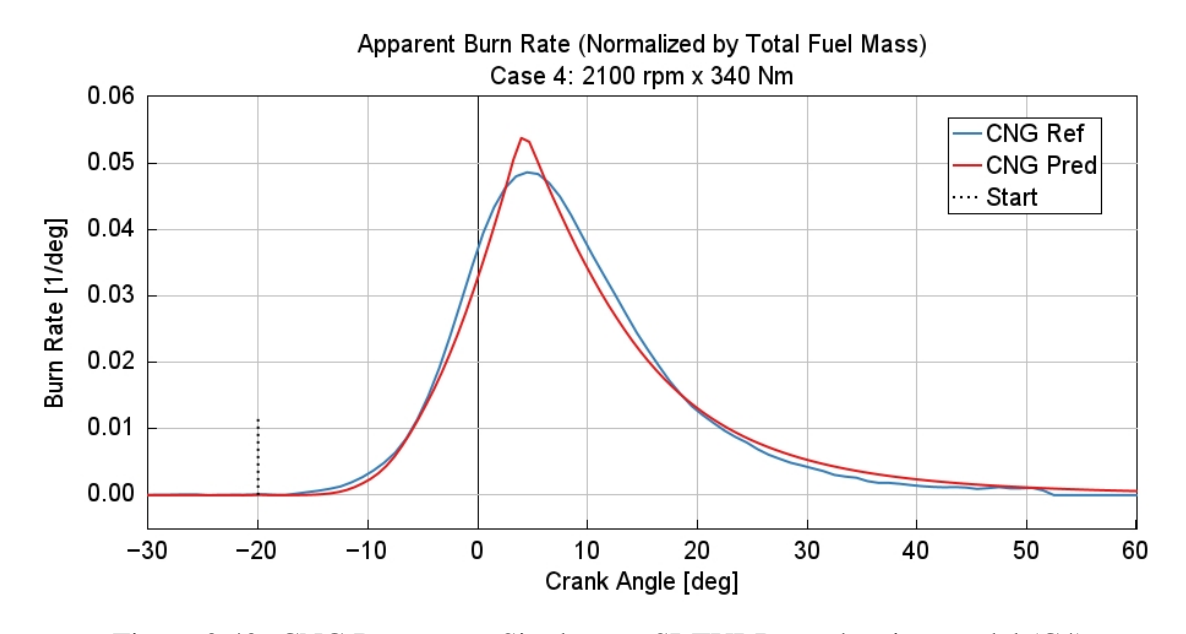


Figure 2.42: CNG Burn rate - Single case SI-TURB combustion model (C4)

As can be observed from Figures 2.35-2.42, this approach allowed the predicted burn rate profiles to reproduce the experimental ones with good accuracy. Although the peak values are slightly higher than the experimental references, the overall trends are consistent, and the results can be considered acceptable. Similarly, the in-cylinder pressure traces closely reproduce the experimental pressure curves, further confirming the reliability of the obtained results.

The engine performance parameters are collected in Table 2.7

Parameters	Brake T	orque [Nm]	IMEP	[bar]	BMEP [bar]		
Farameters	Exp	Sim	Exp	Sim	Exp	Sim	
C1	290.38	290.44	7.69	7.66	6.08	6.20	
C2	184.72	188.10	5.40	5.37	3.87	4.02	
C3	559.08	560.27	13.35	14.30	11.71	11.97	
C4	340.50	340.40	8.57	9.46	7.13	7.27	

Table 2.7: CNG engine performance parameters - Single case SI-TURB combustion model

By comparing the two different optimisation techniques, it was concluded that the second approach is more effective. Therefore, this method was adopted, with different multiplier values assigned to each operating condition.

Finally, once the optimal values for the dilution effect, flame kernel growth, turbulent flame speed, and Taylor length scale multipliers were identified, they were implemented in the mono-cylinder engine models as combustion parameters, thereby defining the burn rate behaviour.

# 2.5 Hydrogen addition strategies

After the methane engine model was properly calibrated, using the Three Pressure Analysis to determine the real burn rate and developing a predictive model able to adapt to different engine operating conditions, hydrogen was introduced into the model as an additional fuel, together with the methane. While the configuration with only methane was referred to as CNG, the blended configuration is here referred to as HCNG, followed by the dilution percentage used.

Hydrogen is injected at a specified dilution level with respect to methane. In this work, analyses were carried out at 15% and 25% molar dilution ratios. Since both fuels are considered ideal gases, the molar dilution can also be interpreted as a volumetric dilution, because the volume of an ideal gas is directly proportional to the number of moles.

The molar dilution is calculated using the following formulas:

$$n_{CH_4} = \frac{m_{CH_4}}{M_{CH_4}}$$
 $n_{H_2} = n_{CH_4} \cdot Dilution$ 
 $m_{H_2} = n_{H_2} \cdot M_{H_2}$ 
 $m_{CH_4new} = m_{CH_4} - m_{H_2}$ 

(2.10)

where  $n_{CH_4}$  and  $n_{H_2}$  are the number of moles,  $m_{CH_4}$  and  $m_{H_2}$  are the injected mass per cycle,  $M_{CH_4}$  and  $M_{H_2}$  are the molar masses (16.02 g/mol for methane and 2.02 g/mol for

hydrogen), and Dil is the desired dilution fraction. The initial methane mass per cycle was obtained from the previous CNG simulations.

The results of the dilution calculation for 15% and 25% are reported in the following tables.

	15% dilution								
	m <sub>CH4</sub> [g/cycle]	$n_{CH_4}$ [mol]	$n_{H_2}$ [mol]	$m_{H_2}$ [g/cycle]	m <sub>CH<sub>4</sub>,new</sub> [g/cycle]				
C1	0.041742	0.002620	0.000390	0.000789	0.040953				
C2	0.030810	0.001920	0.000288	0.000582	0.030228				
C3	0.072035	0.004491	0.000674	0.001361	0.070674				
C4	0.047720	0.002975	0.000446	0.000901	0.046819				

Table 2.8: HCNG15 injected masses

	25% dilution								
	m <sub>CH4</sub> [g/cycle]	$n_{CH_4}$ [mol]	$n_{H_2}$ [mol]	$m_{H_2}$ [g/cycle]	$m_{CH_4,new}$ [g/cycle]				
C1	0.041742	0.002620	0.000650	0.001314	0.040427				
C2	0.030810	0.001920	0.000480	0.000970	0.029840				
C3	0.072035	0.004491	0.001123	0.002268	0.069767				
C4	0.047720	0.002975	0.000744	0.0001502	0.046218				

Table 2.9: HCNG25 injected masses

To enable hydrogen injection, the base engine model was modified by adding an additional injector dedicated to hydrogen and by replacing the previous injectors with the "InjPulseConn" type, as shown in Figure 2.43. The fuel masses calculated in Tables 2.8-2.9 were then inserted in the corresponding injectors according to the selected dilution level.

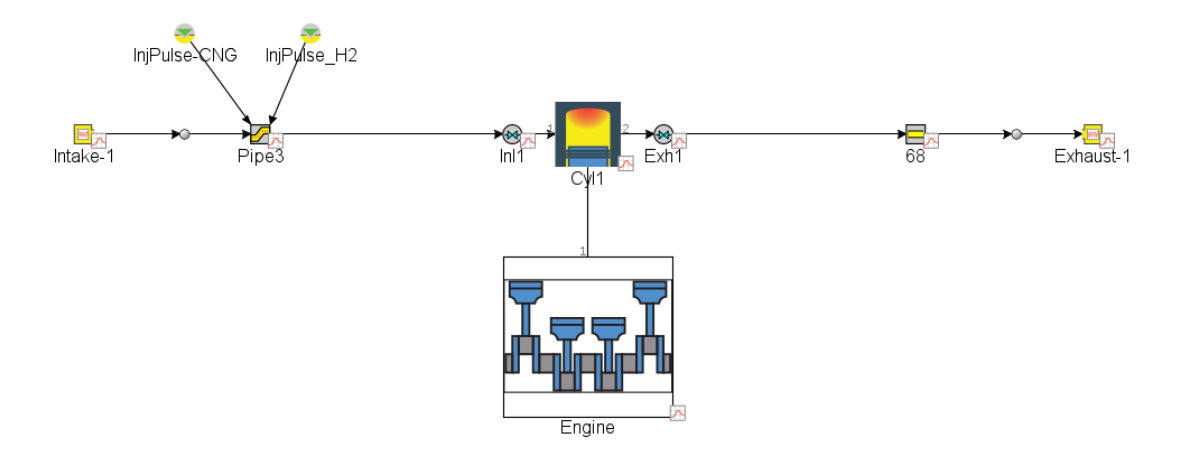


Figure 2.43: Mono-cylinder engine model with H<sub>2</sub> injector inserted

As discussed in the previous chapter 2.2, the first set of analyses was performed using the Wiebe function as the burn rate model, to compare the behaviour with respect to the CNG

case, where the same combustion formulation was applied.

The results obtained from this analysis were not acceptable, since the lambda value for each engine operating condition shifted toward a rich mixture for both dilution levels, as reported in Table 2.10.

<b>Operating points</b>	HCNG15	HCNG25
C1	0.9976	0.9752
C2	0.9681	0.9471
C3	0.9696	0.9497
C4	0.9855	0.9623

Table 2.10: HCNG  $\lambda$  values with Wiebe combustion model

This behaviour occurs due to the change in the stoichiometry of the resulting fuel blend. For a generic hydrocarbon fuel  $C_xH_y$ , the stoichiometric combustion reaction is:

$$C_x H_y + \left(x + \frac{y}{4}\right) O_2 \rightarrow xCO_2 + \frac{y}{2} H_2 O$$
 (2.11)

Considering that 1 kmol of  $O_2$  is accompanied by 3.76 kmol of  $N_2$  in air, the stoichiometric air–fuel ratio ( $AFR_{\text{stoich}}$ ) can be expressed as:

$$AFR_{\text{stoich}} = \frac{\left(x + \frac{y}{4}\right) \cdot (M_{O_2} + 3.76M_{N_2})}{M_{\text{fuel}}}$$
(2.12)

where  $M_{\text{fuel}}$  is the molar mass of the fuel.

Applying the above formula to the individual fuels, the following  $AFR_{\text{stoich}}$  values are obtained:

- $AFR_{stoich.CH_4} = 17.2$
- $AFR_{stoich,H_2} = 34.3$

From these values, it is evident that hydrogen requires more air than methane to achieve stoichiometric combustion under equal mass conditions.

For a blended fuel mixture, where each component has a molar fraction  $w_i$ , the equivalent stoichiometric air–fuel ratio ( $AFR_{\text{stoich,mix}}$ ) is computed using a weighted harmonic mean:

$$\frac{1}{AFR_{\text{stoich,mix}}} = \sum_{i} \frac{w_i}{AFR_{\text{stoich},i}}$$
 (2.13)

Once  $AFR_{\text{stoich,mix}}$  is determined, the lambda value can be calculated using Eq. 2.9, where the denominator corresponds to the stoichiometric value previously obtained. When hydrogen is added,  $AFR_{\text{stoich,mix}}$  increases. If the supplied air mass remains constant, the denominator increases, leading to a reduction in the lambda value. This means that the mixture becomes richer.

To solve this issue, the amount of air available for combustion was increased by raising the intake pressure. This increases the trapped air mass per cycle, thereby raising  $AFR_{\text{actual}}$  and consequently also the lambda up to the stoichiometric condition.

This adjustment was performed through a parametric sweep, in which lambda values were monitored as the intake pressure was progressively varied. The pressure value was increased incrementally with a step size of 0.5% relative to the initial reference condition. Up to now, for all the future analyses in steady-state condition for the HCNG mixtures, the intake pressure values are the ones reported in the Table 2.11.

		HCNG15		HCNG25			
<b>Operating points</b>	P <sub>int</sub> [bar]	P <sub>int,mod</sub> [bar]	Increment [%]	P <sub>int</sub> [bar]	P <sub>int,mod</sub> [bar]	Increment [%]	
C1	0.799971	0.803971	0.5	0.799971	0.823971	3	
C2	0.599093	0.617066	3	0.599093	0.629048	5	
C3	1.333479	1.373483	3	1.333479	1.400153	5	
C4	0.932486	0.951135	2	0.932486	0.969785	4	

Table 2.11: HCNG Intake pressure increase - Wiebe combustion model

The results of the analysis conducted with the Wiebe function as a combustion object, increasing the intake pressure, are observable in the Figures 2.44-2.47.

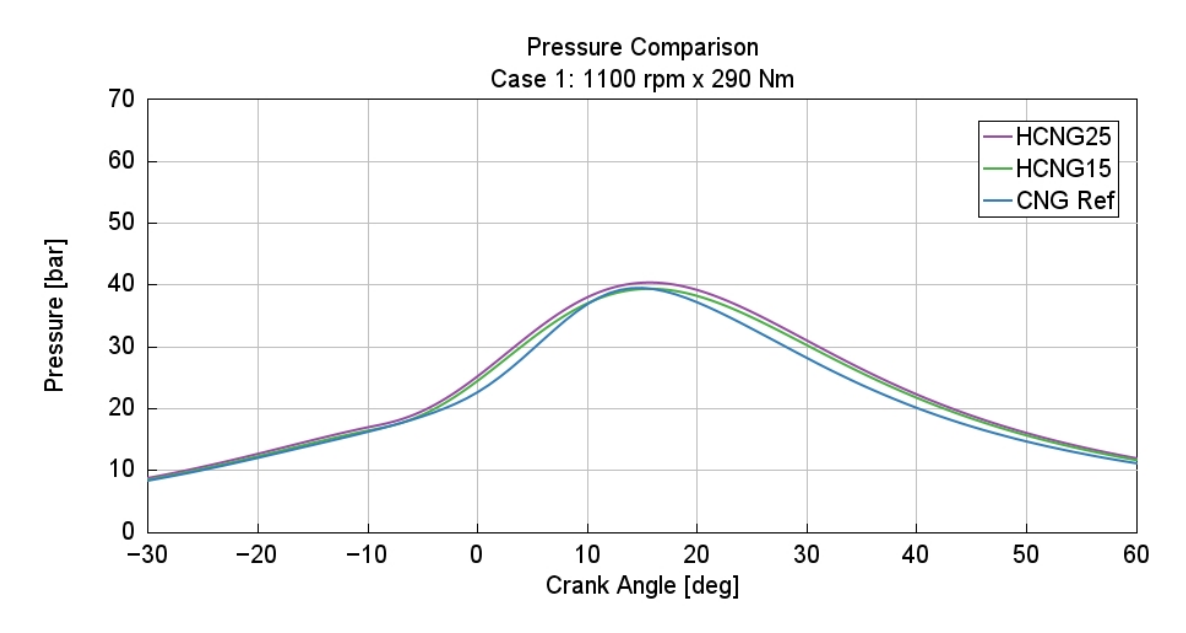


Figure 2.44: HCNG In-cylinder pressure - Wiebe combustion model (C1)

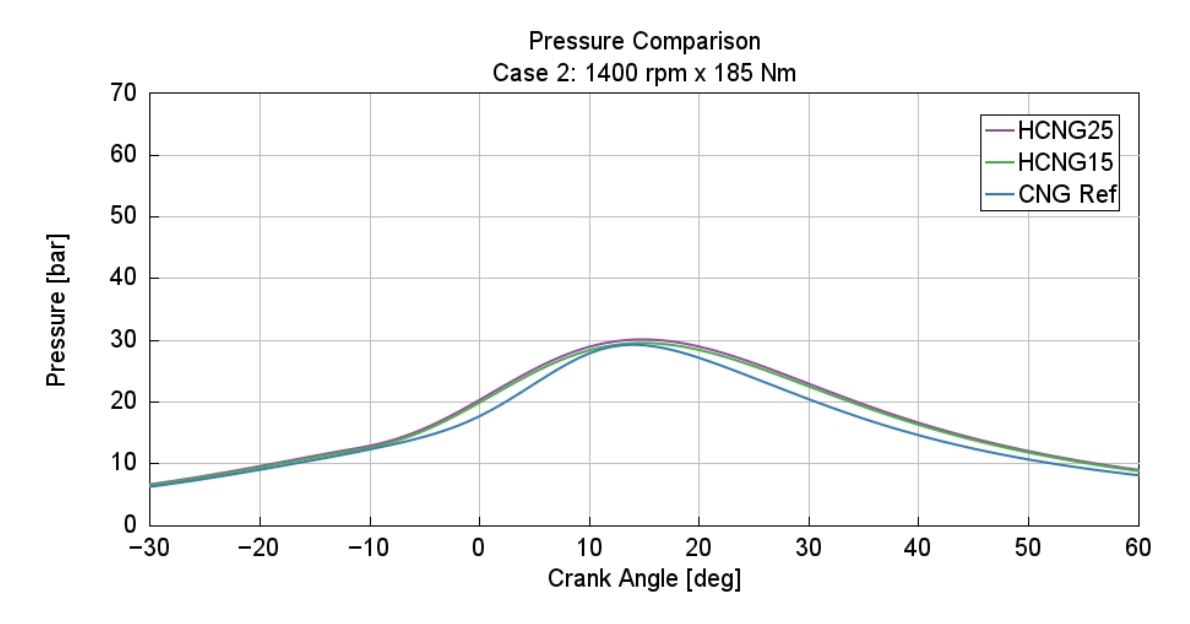


Figure 2.45: HCNG In-cylinder pressure - Wiebe combustion model (C2)

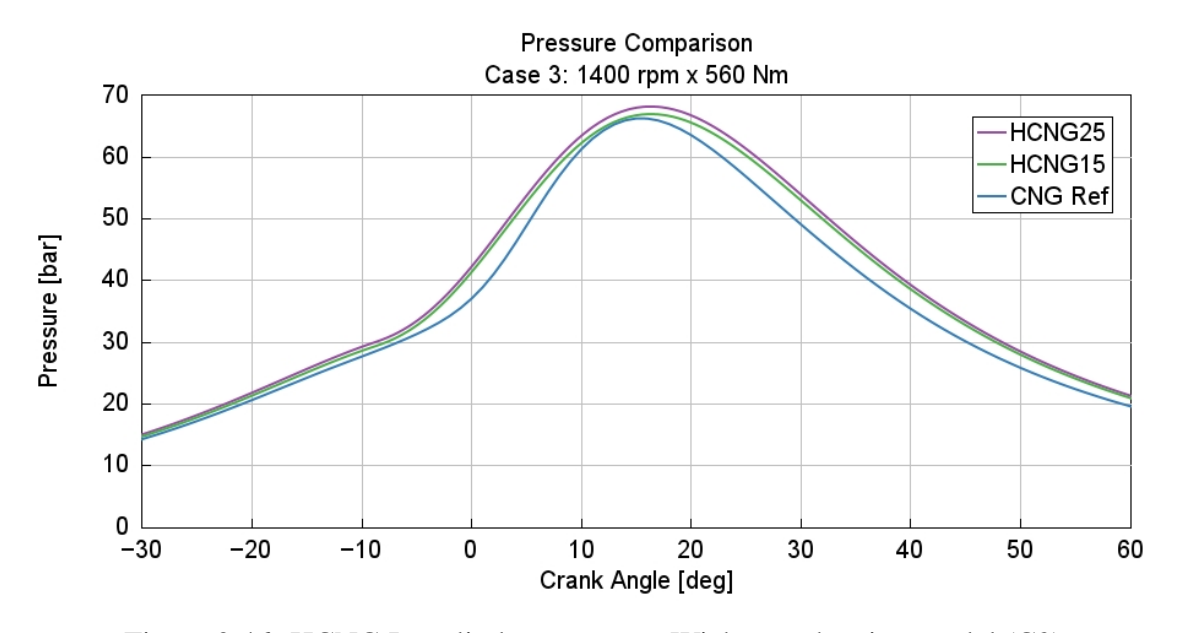


Figure 2.46: HCNG In-cylinder pressure - Wiebe combustion model (C3)

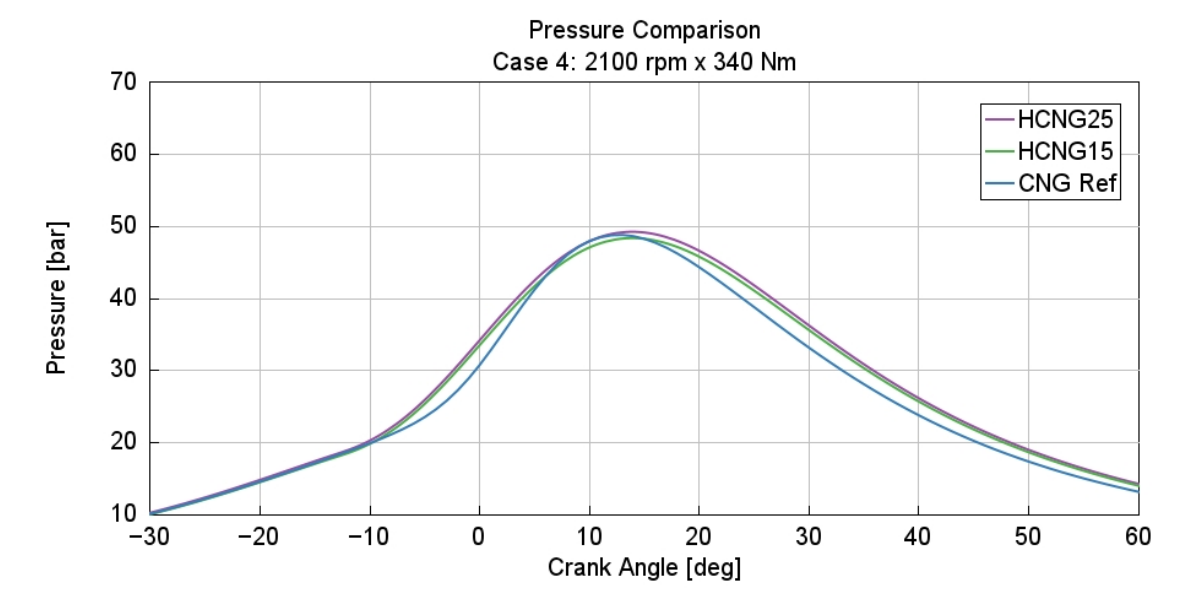


Figure 2.47: HCNG In-cylinder pressure - Wiebe combustion model (C4)

Observing the pressure comparison graphs, similar to the analysis conducted with methane, the simulated pressure traces do not accurately reproduce the reference pressure profiles. Although an overall increase in pressure is expected due to the hydrogen content, which results in slightly higher peak pressures and generally elevated values at all crank angles, the simulated curves fail to capture the shape of the reference profiles. Specifically, deviations are observed in both the rising and falling phases of the pressure trace, with a rightward shift of the pressure peak.

These discrepancies arise because the Wiebe function is a simplified combustion model, originally calibrated for CNG. When the fuel composition is changed, as in the case of HCNG blends, the combustion duration is altered and generally becomes faster. Consequently, the Wiebe function can no longer accurately represent the actual combustion process, resulting in simulated pressure curves that differ in both shape and timing from the experimental data. The tables below report the engine performance parameters obtained from this analysis for the HCNG15 and HCNG25 analyses. These discrepancies arise because the Wiebe function is a simplified combustion model, originally calibrated for CNG. When the fuel composition is changed, as in the case of HCNG blends, the combustion duration is altered and generally becomes faster. Consequently, the Wiebe function can no longer accurately represent the actual combustion process, resulting in simulated pressure curves that differ in both shape and timing from the experimental data.

As observed from the Tables 2.12-2.13, the addition of hydrogen leads to a slightly higher brake torque, particularly in the HCNG25 case, due to the higher hydrogen concentration. This phenomenon is expected, since hydrogen increases the flame speed, accelerating the combustion process and consequently raising the in-cylinder pressure. Moreover, hydrogen has a wider flammability range and requires less ignition energy, which enhances

combustion with fewer unburned residuals. As a result, a greater portion of the chemical energy is converted into mechanical work. Naturally, the higher the hydrogen content in the mixture, the more pronounced these effects become [17][18].

HCNG15									
Parameters	Brake T	orque [Nm]	IMEP	[bar]	BMEP [bar] λ [-]		[-]		
Parameters	Exp	Sim	Exp	Sim	Exp	Sim	Exp	Sim	
C1	290.38	294.58	7.69	7.79	6.08	6.29	1	1.002	
C2	184.72	187.34	5.40	5.60	3.87	4.15	1	1.003	
СЗ	559.08	572.72	13.35	14.57	11.71	12.39	1	1.003	
C4	340.50	347.09	8.57	9.49	7.13	7.47	1	1.007	

Table 2.12: HCNG15 engine performance parameters - Wiebe combustion model

HCNG25									
D	Brake T	orque [Nm]	IMEP	[bar]	BMEP [bar]		λ [-]		
Parameters	Exp	Sim	Exp	Sim	Exp	Sim	Exp	Sim	
C1	290.38	302.66	7.69	7.97	6.08	6.46	1	1.009	
C2	184.72	199.95	5.40	5.72	3.87	4.27	1	1.007	
СЗ	559.08	592.60	13.35	14.85	11.71	12.66	1	1.004	
C4	340.50	357.89	8.57	9.67	7.13	7.64	1	1.008	

Table 2.13: HCNG25 engine performance parameters - Wiebe combustion model

### 2.5.1 Burn rate evaluation for HCNG mixtures with TPA analysis

In this section, as it was performed for the CNG, the burn rate was calculated by performing a TPA analysis. For this analysis, it is necessary to impose the pressure at the intake and exhaust manifold, as well as the in-cylinder pressure. Since for hydrogen, no incylinder pressure experimental data are available, the TPA analysis was carried out only for the HCNG15 case, using the in-cylinder pressure data from the CNG. For HCNG25, instead, the analysis was not performed. In order to evaluate the case with 25% hydrogen using a realistic burn rate, the profile obtained from the TPA analysis of HCNG15 was also applied for the HCNG25 case. This assumption is considered acceptable for the HCNG15, since the deviation from the CNG in-cylinder pressure is limited, whereas for HCNG25, the approximation would introduce larger errors. Utilising the same burn rate for HCNG25, only minor differences are expected. However, in the absence of experimental data, this represents the most reliable strategy to conduct the engine performance parameters analysis. The results obtained are showed in Figures 2.48-2.55.

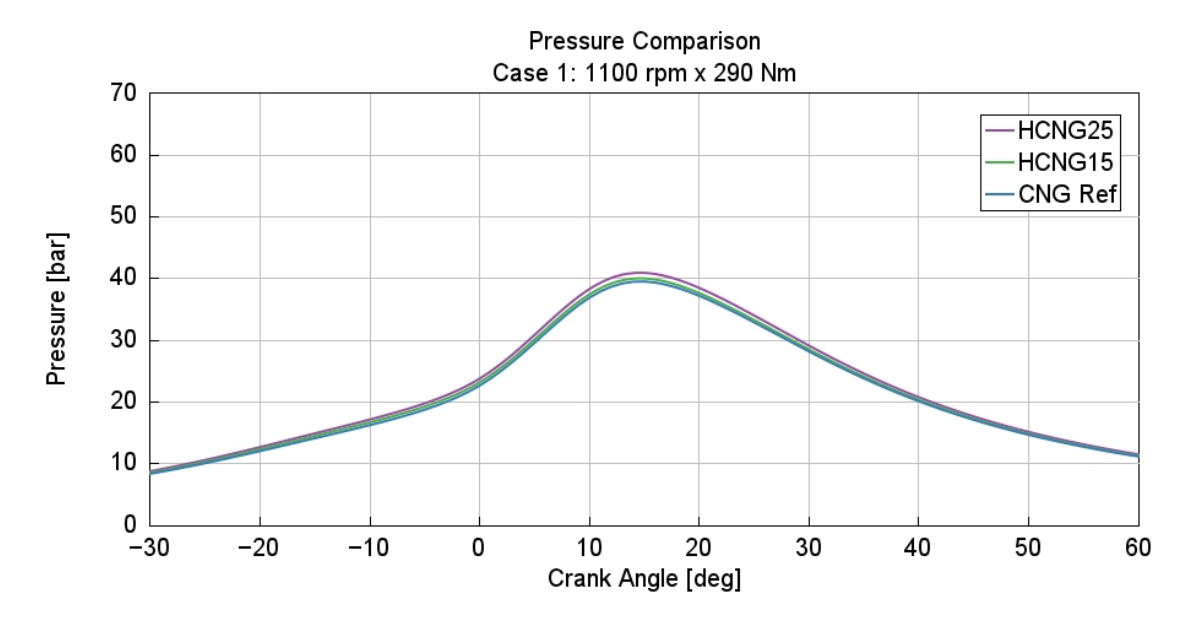


Figure 2.48: HCNG In-cylinder pressure - TPA combustion model (C1)

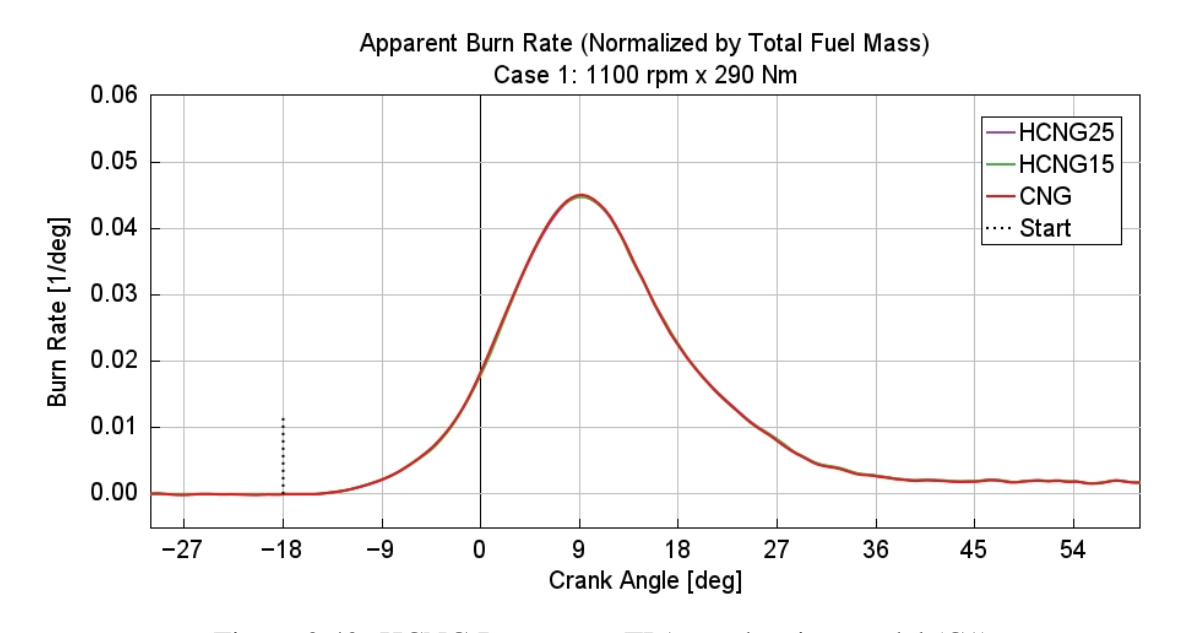


Figure 2.49: HCNG Burn rate - TPA combustion model (C1)

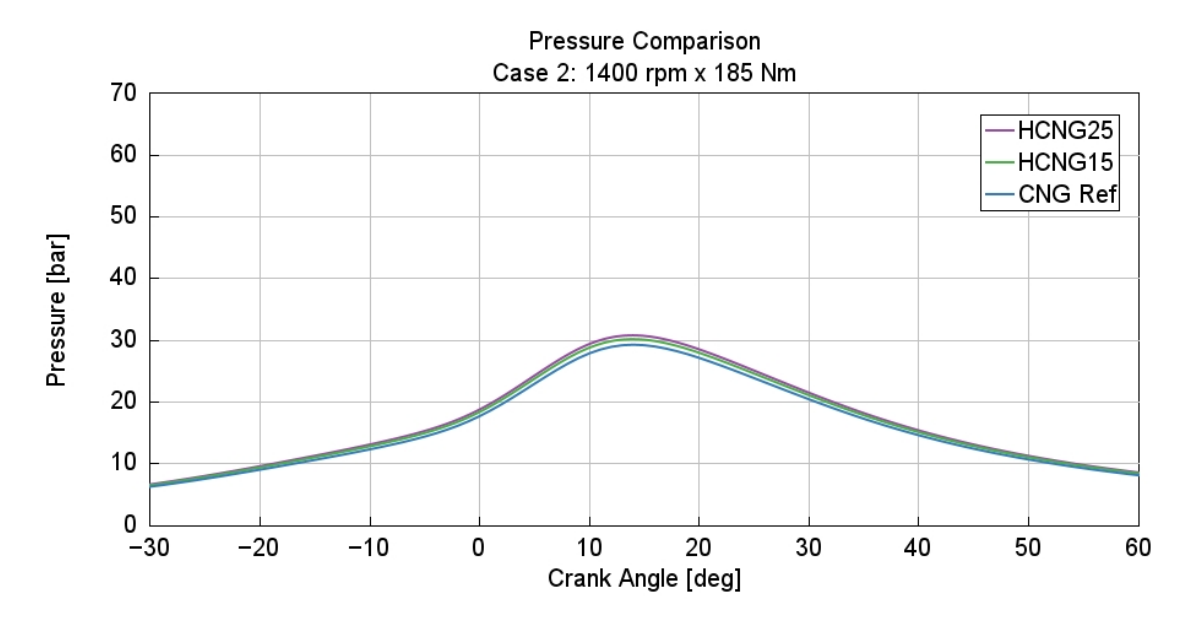


Figure 2.50: HCNG In-cylinder pressure - TPA combustion model (C2)

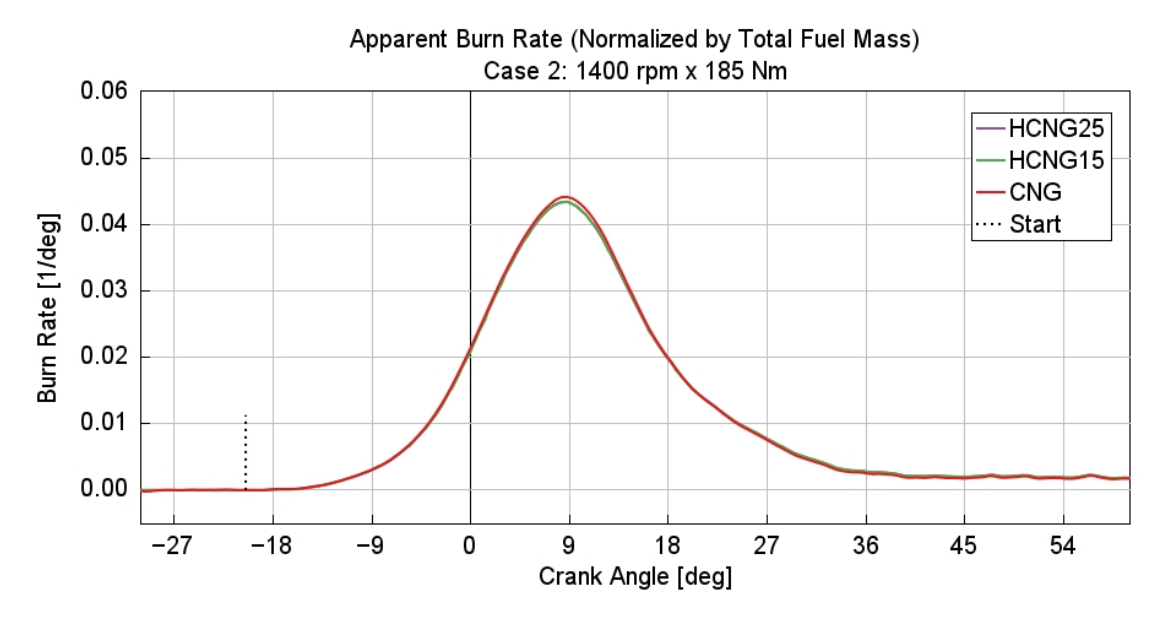


Figure 2.51: HCNG Burn rate - TPA combustion model (C2)

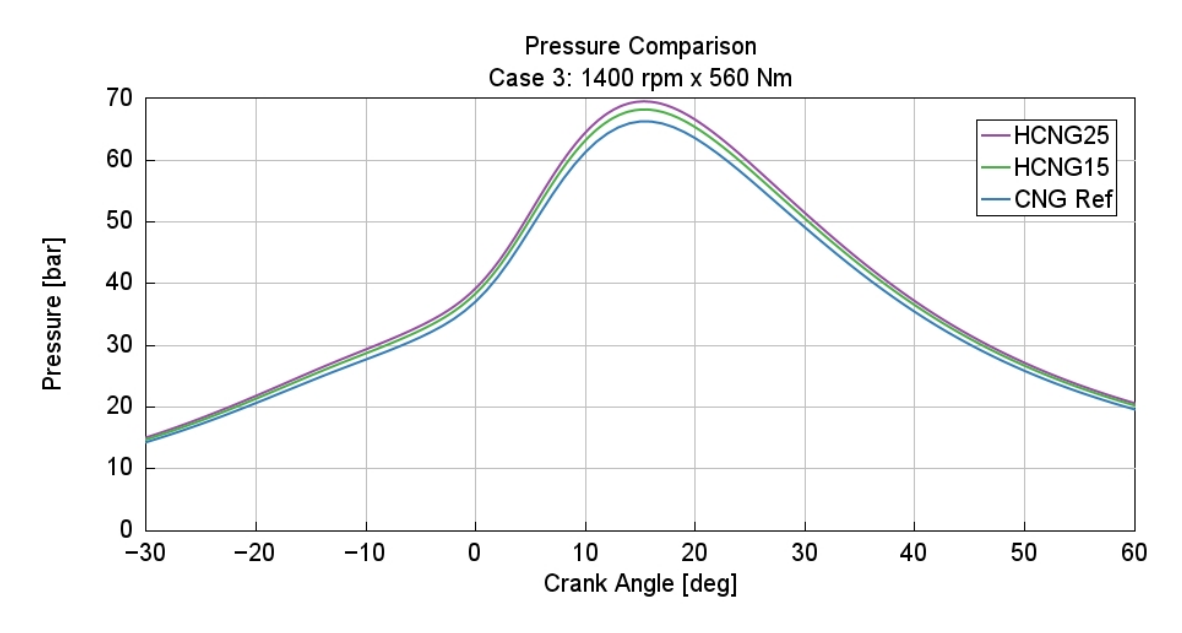


Figure 2.52: HCNG In-cylinder pressure - TPA combustion model (C3)

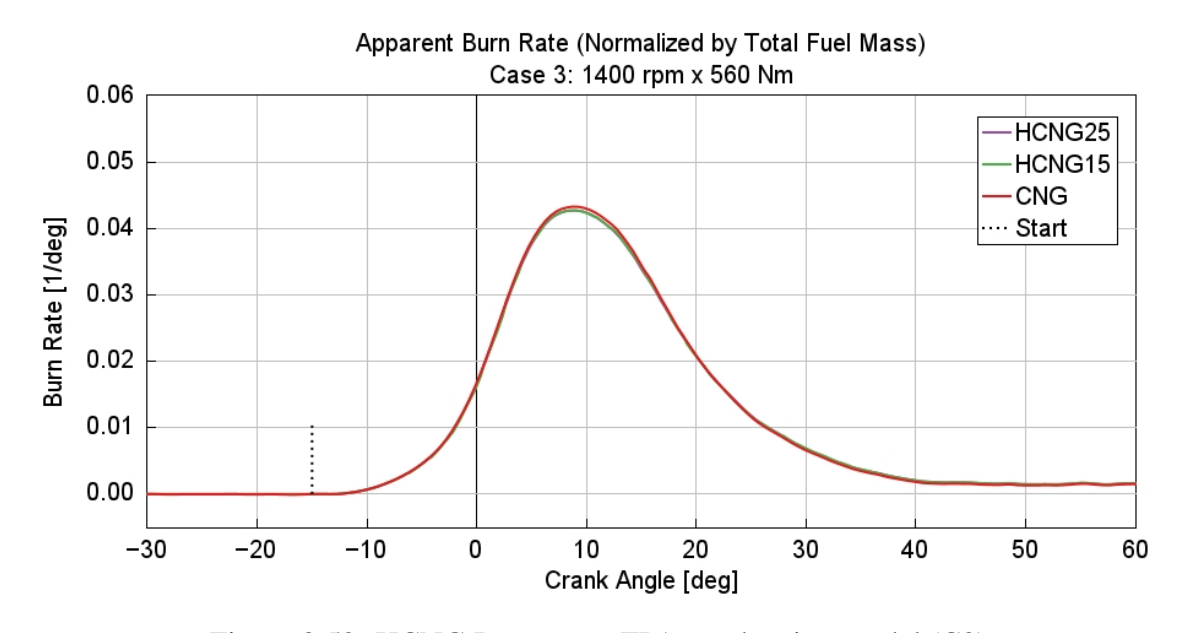


Figure 2.53: HCNG Burn rate - TPA combustion model (C3)

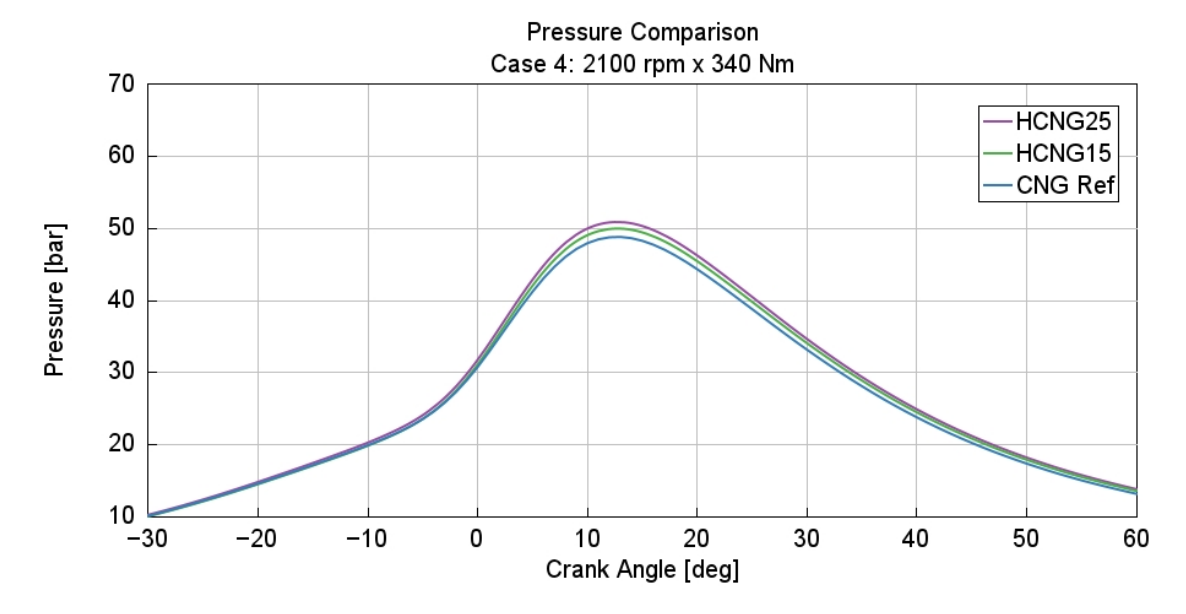


Figure 2.54: HCNG In-cylinder pressure - TPA combustion model (C4)

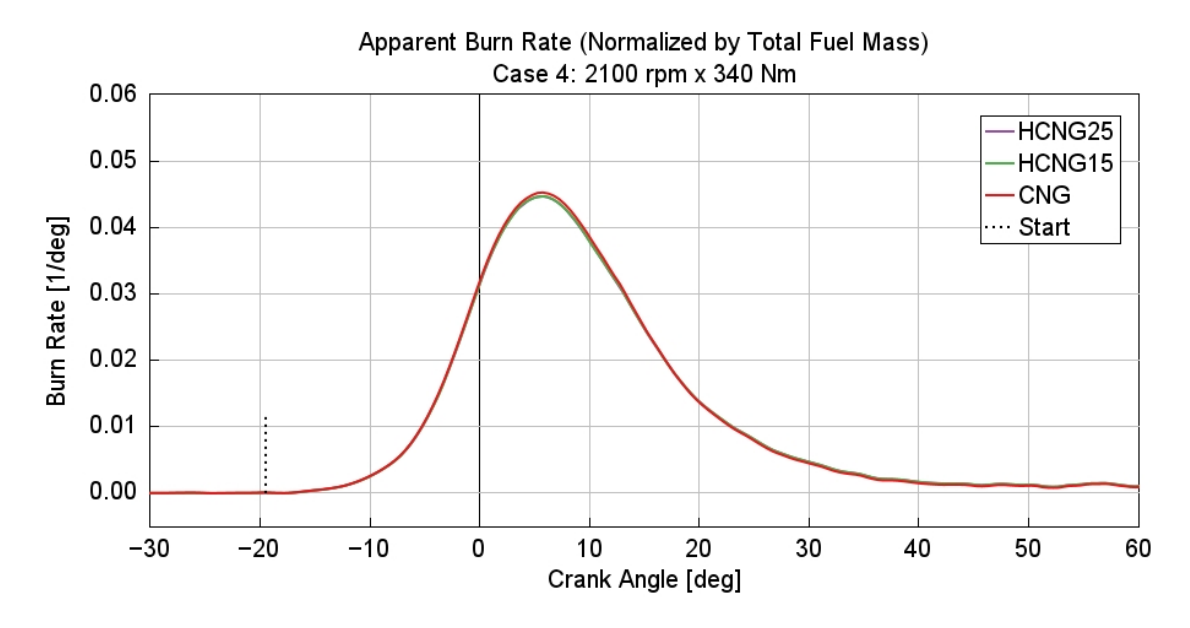


Figure 2.55: HCNG Burn rate - TPA combustion model (C4)

From the analysis of the graphs, a clear improvement can be observed compared to the results obtained using the Wiebe function. Also in this case, the pressure curves present slightly higher peak values. However, the profiles obtained in this case show an excellent agreement with the experimental one.

Observing the burn rate curves, it is noticeable that the profiles are consistent with those obtained through the TPA analysis performed on the CNG case. The peak burn rate appears slightly lower compared to the pure methane case, despite the overall shape of the curves remaining practically identical. The engine performance parameters obtained from this analysis are reported in Tables 2.14-2.15.

HCNG15									
D	Brake T	orque [Nm]	IMEP	[bar]	BMEP [bar]		λ	λ [-]	
Parameters	Exp	Sim	Exp	Sim	Exp	Sim	Exp	Sim	
C1	290.38	294.58	7.69	7.49	6.08	6.29	1	1.004	
C2	184.72	189.68	5.40	5.35	3.87	4.05	1	1.005	
C3	559.08	575.06	13.35	14.17	11.71	12.28	1	1.004	
C4	340.50	349.42	8.57	9.26	7.13	7.46	1	1.007	

Table 2.14: HCNG15 engine performance parameters - TPA combustion model

HCNG25								
Parameters	Brake Torque [Nm]		IMEP [bar]		BMEP [bar]		λ [-]	
	Exp	Sim	Exp	Sim	Exp	Sim	Exp	Sim
C1	290.38	302.06	7.69	7.66	6.08	6.45	1	1.009
C2	184.72	194.84	5.40	5.47	3.87	4.16	1	1.009
C3	559.08	586.95	13.35	14.43	11.71	12.54	1	1.005
C4	340.50	357.29	8.57	9.43	7.13	7.63	1	1.008

Table 2.15: HCNG25 engine performance parameters - TPA combustion model

The considerations drawn from the analysis of the engine performance parameters for the HCNG case with the Wiebe function can also be extended to the present case.

## 2.5.2 Predictive modelling of HCNG combustion with SI-TURB model

The predictive SI-TURB combustion model was also applied to a methane-hydrogen blend in order to assess the validity and robustness of the burn rate multipliers when the fuel composition differs from the one used for calibration. To perform this analysis, it was necessary to modify the combustion object by adjusting the following parameters: dilution effect multiplier, flame kernel growth multiplier, turbulent flame speed multiplier, and Taylor length scale multiplier. In addition, the fuel type had to be specified. Since the software does not allow the direct definition of fuel mixtures for this analysis, methane was imposed as the reference fuel. This assumption introduces only a minor approximation, as reported in [19], where it is shown that up to 40% hydrogen by volume, the laminar flame speed of the mixture can be considered comparable to that of pure methane. The resulting in-cylinder pressure traces and burn rates are presented in the following figures.

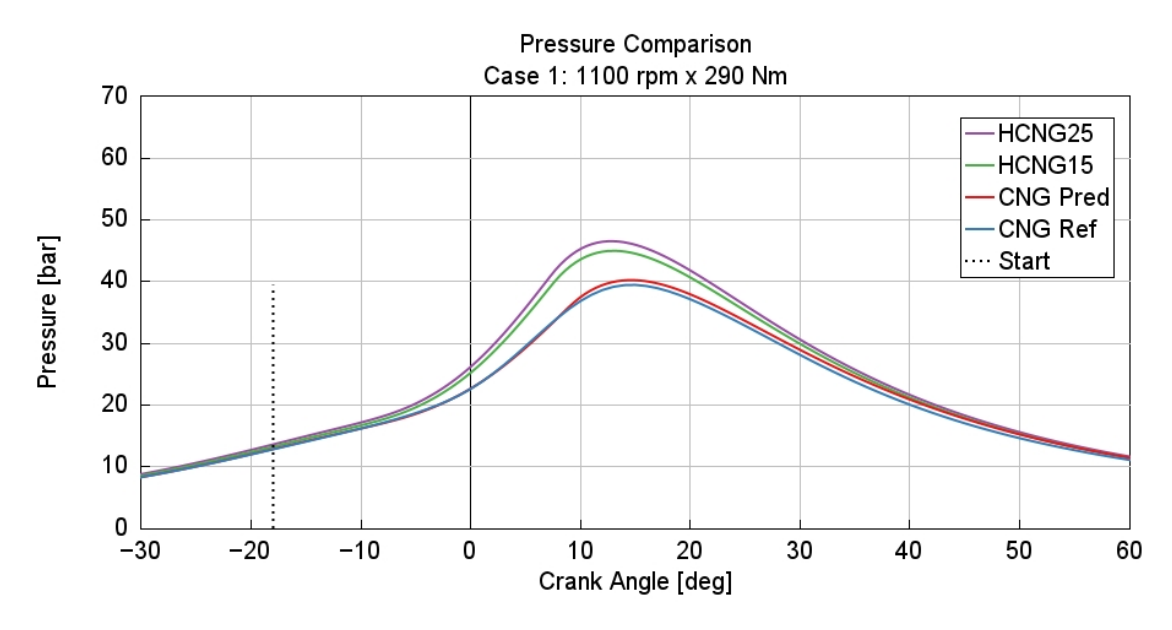


Figure 2.56: HCNG In-cylinder pressure - SI-TURB combustion model (C1)

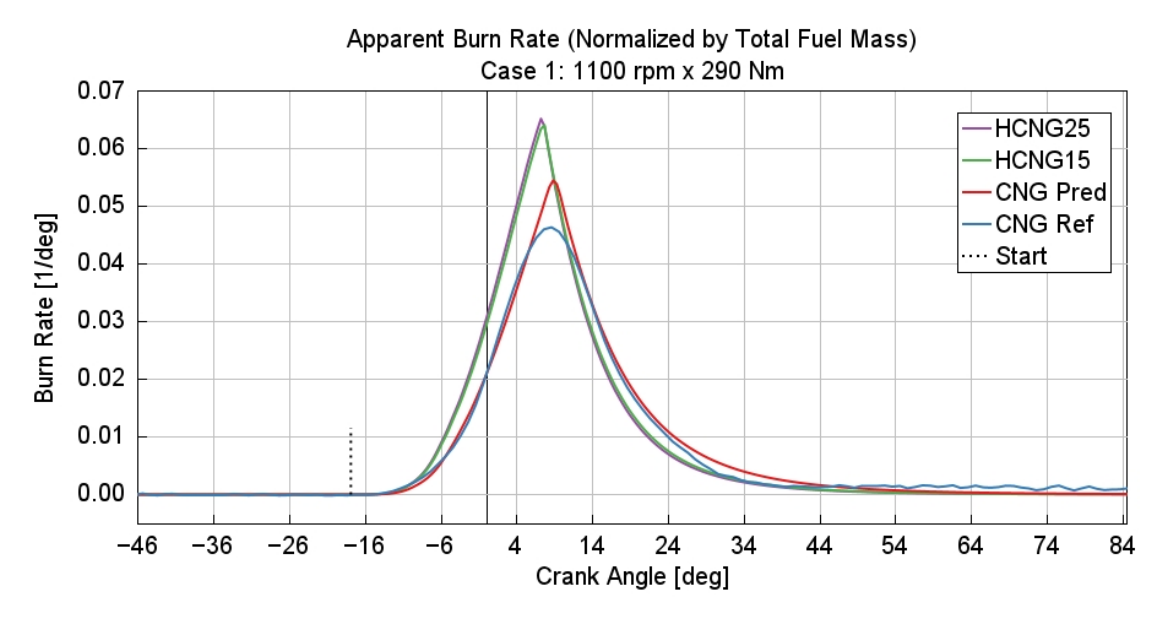


Figure 2.57: HCNG Burn rate - SI-TURB combustion model (C1)

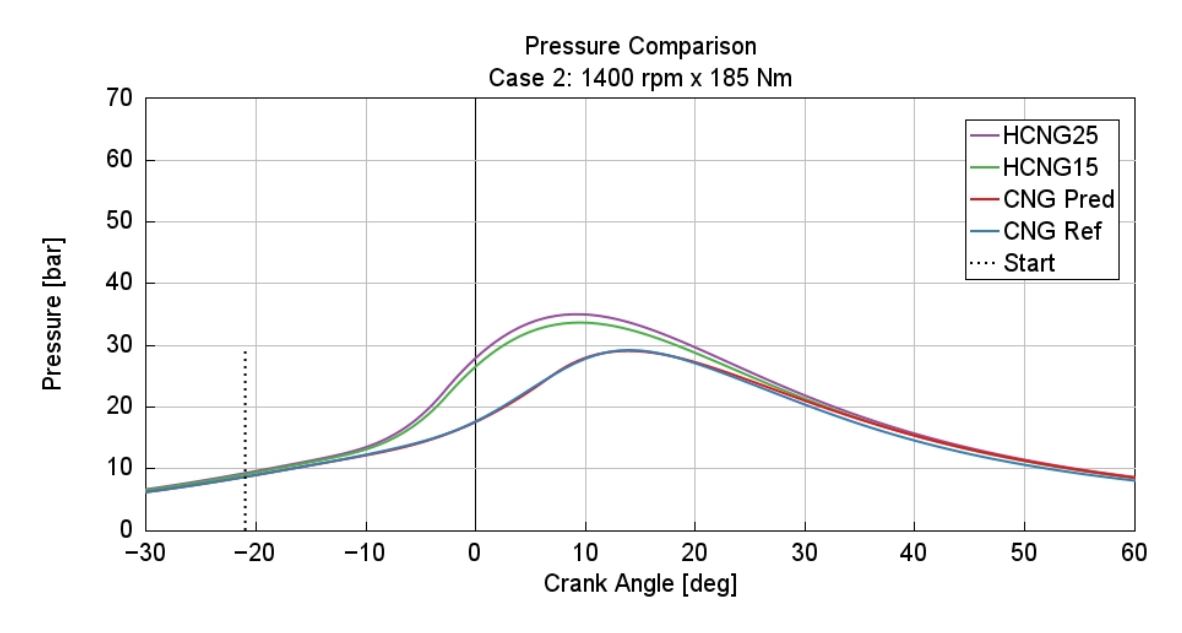


Figure 2.58: HCNG In-cylinder pressure - SI-TURB combustion model (C2)

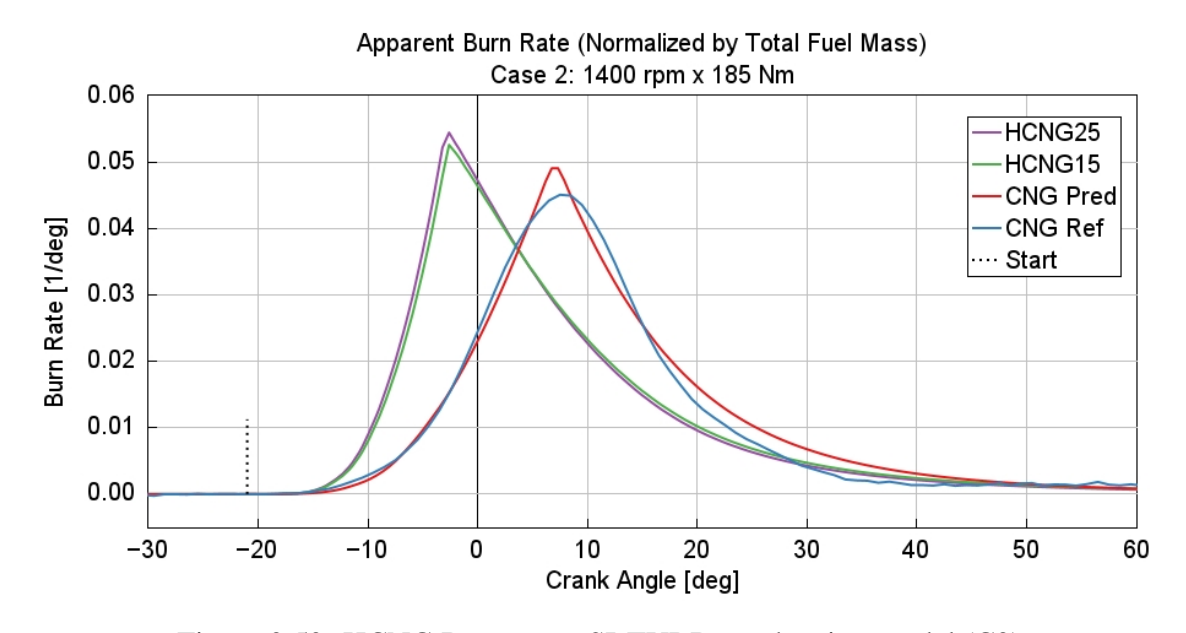


Figure 2.59: HCNG Burn rate - SI-TURB combustion model (C2)

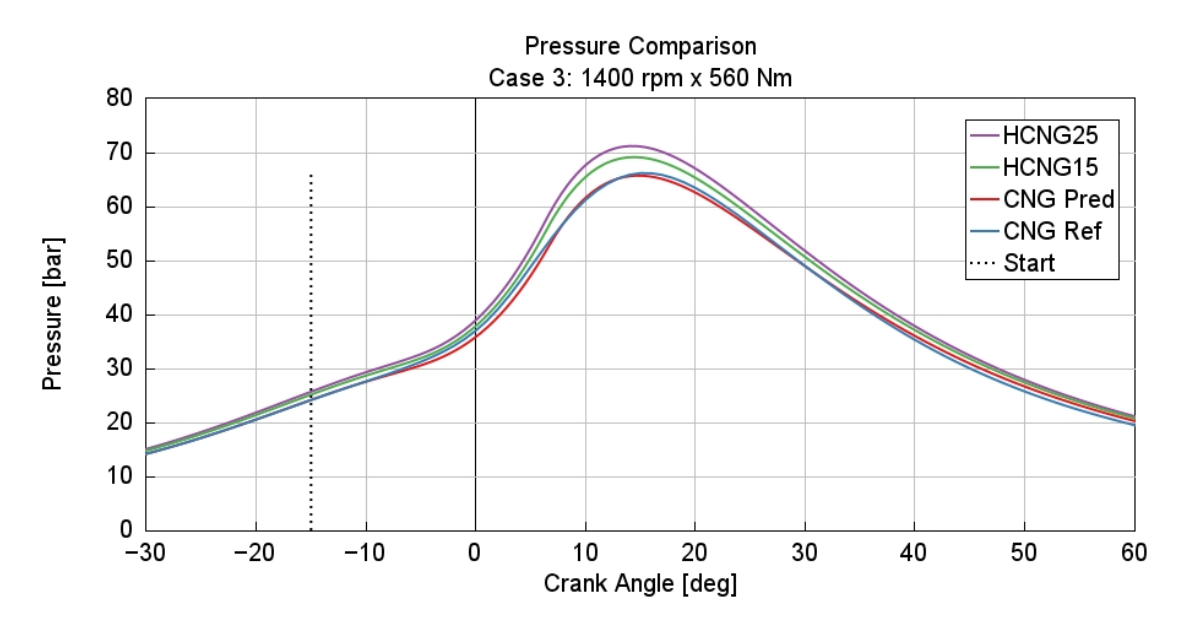


Figure 2.60: HCNG In-cylinder pressure - SI-TURB combustion model (C3)

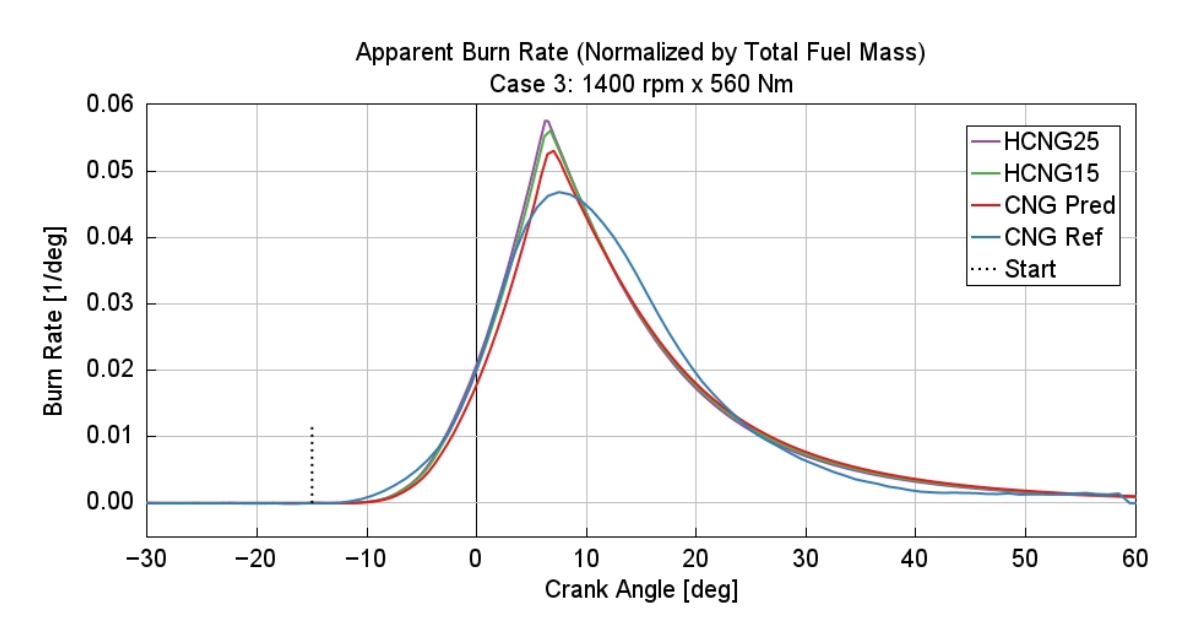


Figure 2.61: HCNG Burn rate - SI-TURB combustion model (C3)

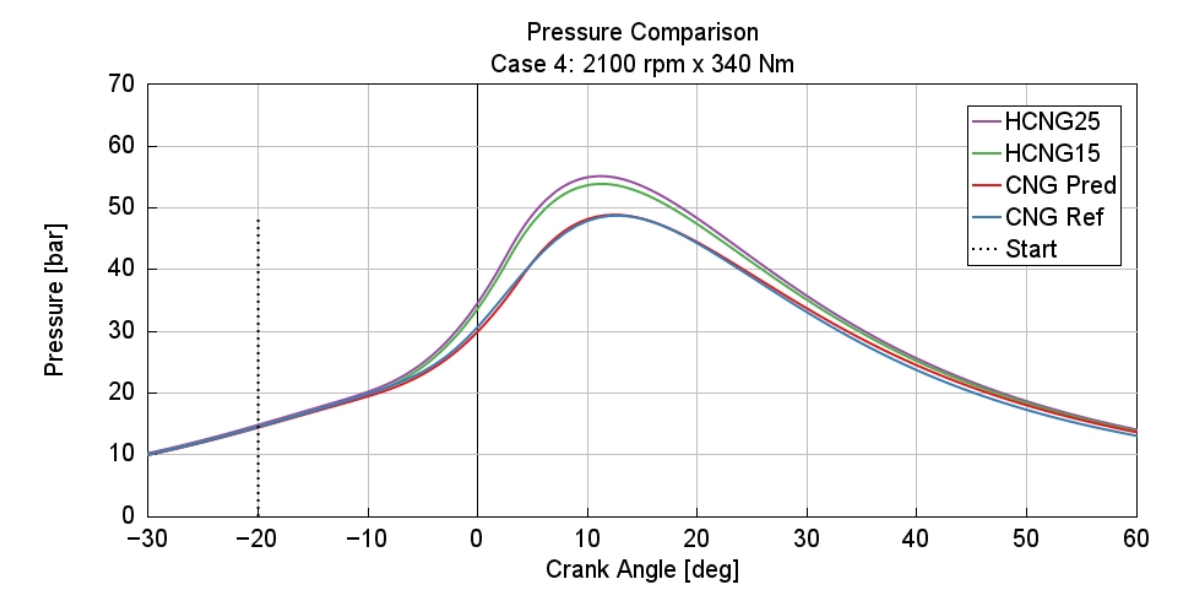


Figure 2.62: HCNG In-cylinder pressure - SI-TURB combustion model (C4)

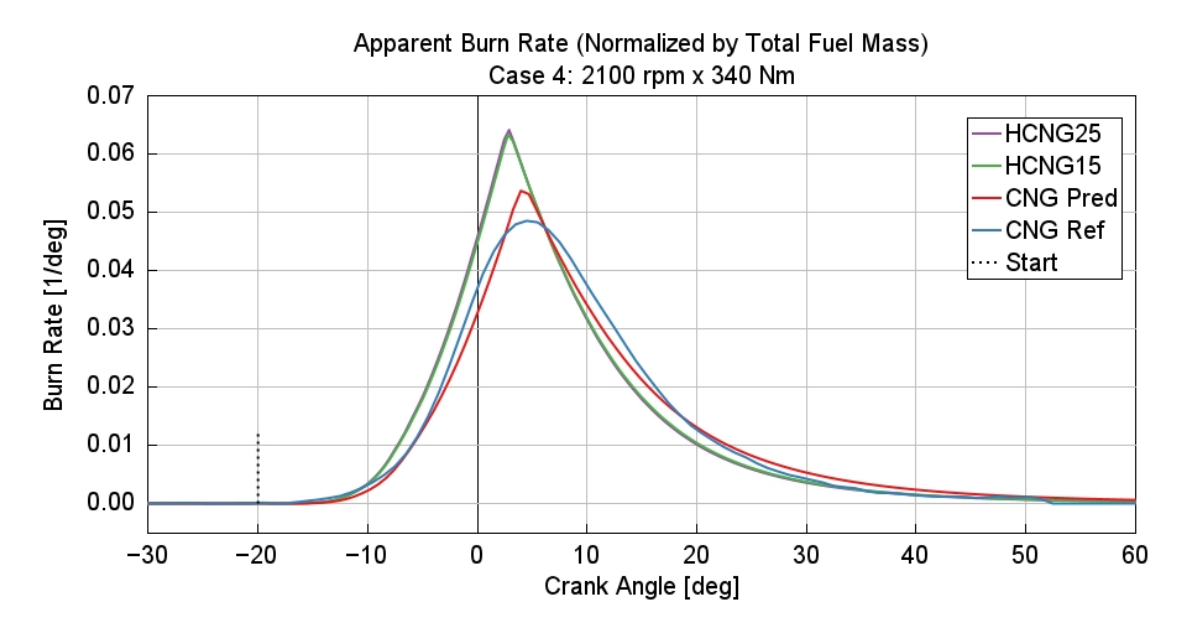


Figure 2.63: HCNG Burn rate - SI-TURB combustion model (C4)

From the burn rate analysis, it is evident that applying the SI-TURB multipliers calibrated and optimised for methane-hydrogen blends does not fully reproduce the reference burn rate behaviour. In all cases, the burn rate peaks are higher, which is expected due to the presence of hydrogen and its higher flame propagation speed, leading to faster combustion and an increased burn rate peak. Furthermore, the burn rates are advanced in time: only slightly in case C3, moderately in cases C1 and C4, and significantly in case C2, where the burn rate peak is clearly out of phase with respect to the reference. This indicates that, at this operating point, the multipliers obtained for methane do not apply to the methane-hydrogen blend. These trends are also reflected in the in-cylinder pressure traces. In general, the pressure peaks are higher in the HCNG cases, consistent with the increased

burn rate, and they also appear advanced in crank angle position, particularly in case **C2**. The engine performance parameters are reported in the Tables 2.16-2.17.

	HCNG15											
Danamatana	Brake T	orque [Nm]	IMEP [bar]		BMEP [bar]		λ [-]					
Parameters	Exp	Sim	Exp	Sim	Exp	Sim	Exp	Sim				
C1	290.38	290.29	7.69	7.78	6.08	6.31	1	0.998				
C2	184.72	154.62	5.40	5.43	3.87	3.30	1	0.998				
С3	559.08	564.99	13.35	14.37	11.71	12.07	1	1.000				
C4	340.50	345.66	8.57	9.55	7.13	7.38	1	1.006				

Table 2.16: HCNG15 engine performance parameters - SI-TURB combustion model

HCNG25											
Parameters	Brake T	orque [Nm]	IMEP [bar]		BMEI	P [bar]	λ [-]				
	Exp	Sim	Exp	Sim	Exp	Sim	Exp	Sim			
C1	290.38	315.21	7.69	7.97	6.08	6.73	1	1.006			
C2	184.72	198.71	5.40	5.57	3.87	4.24	1	1.002			
СЗ	559.08	597.78	13.35	14.67	11.71	12.77	1	1.001			
C4	340.50	370.15	8.57	9.73	7.13	7.91	1	1.004			

Table 2.17: HCNG25 engine performance parameters - SI-TURB combustion model

As can be observed from the tables, the discrepancies previously highlighted are confirmed by the differences between the experimental and simulated values. Overall, it can be concluded that to achieve reliable burn rate predictions, a dedicated optimisation of the SI-TURB multipliers for methane-hydrogen blends is required. The multipliers calibrated only on methane are not sufficient to guarantee accuracy for HCNG mixtures. A possible improvement would be to extend the predictive calibration over a larger set of engine operating conditions, at least 25 points, to derive a unique set of multipliers that can be applied across different fuel compositions. This would enhance the predictive capability of the model, enabling a more accurate reproduction of the reference burn rate for methane-hydrogen mixtures.

### 2.5.3 Engine emissions comparison

This section aims to evaluate the variation in engine emissions resulting from the introduction of hydrogen into the combustion process. Additionally, this analysis is performed to verify if the trends reported in the literature for the blend of the two fuels (Chapter 1.5) are confirmed by the present study. For a clearer comparison of relative increases and decreases, the results are expressed as percentages normalised to CNG emissions. The results obtained are presented in the bar graphs.

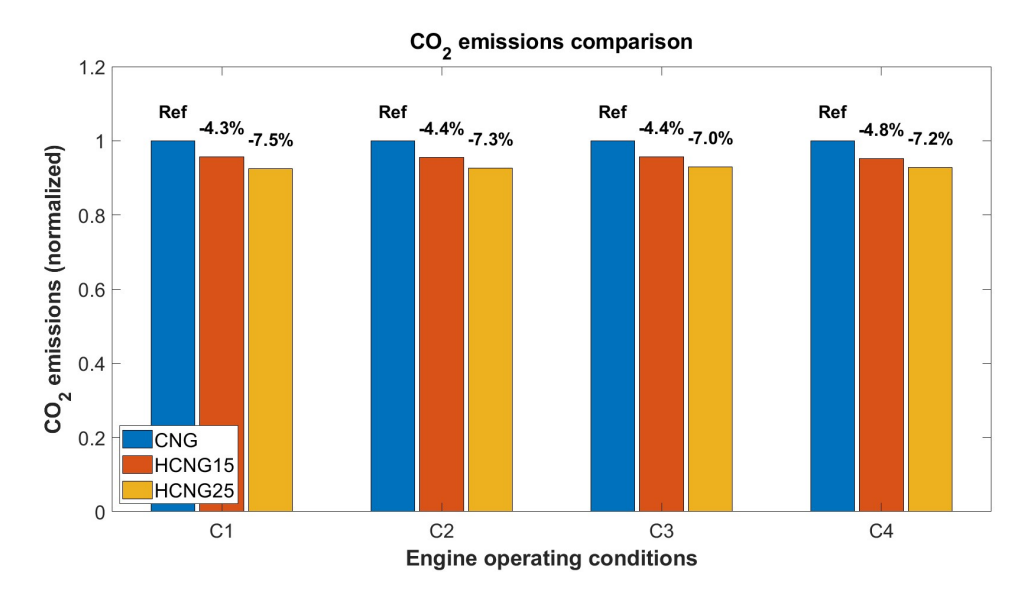


Figure 2.64: CO<sub>2</sub> normalised emissions comparison

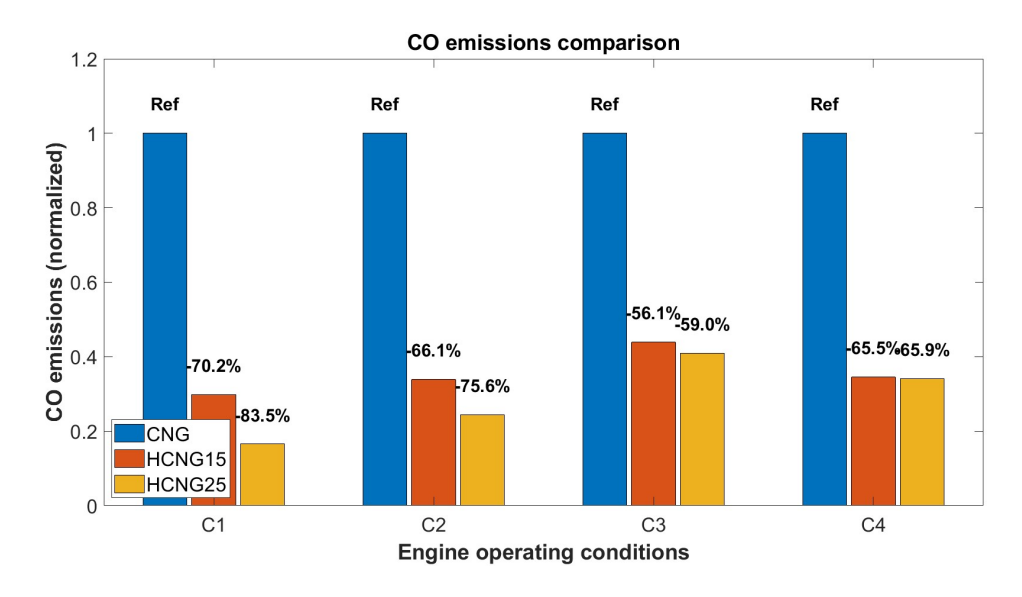


Figure 2.65: CO normalised emissions comparison

As can be observed in Figures 2.64-2.65, the emissions of carbon dioxide and carbon monoxide decrease when hydrogen is added to the combustion process. This reduction is due to the lower carbon content of the blend, as part of the methane is replaced by hydrogen, and to a more complex and faster combustion process. The two pollutants are formed through different mechanisms: CO<sub>2</sub> is the final product of complete combustion, while CO is a partial product of incomplete combustion, occurring when the available oxygen is insufficient or the local temperature is not high enough to fully oxidise carbon into CO<sub>2</sub>. The influence of hydrogen on the combustion process is evident in the charts. The emission of carbon monoxide decreases substantially, whereas the reduction in carbon dioxide is less pronounced. This is also because, although some methane is replaced by hydrogen, the remaining methane content is still high, limiting reductions in CO<sub>2</sub> emissions.

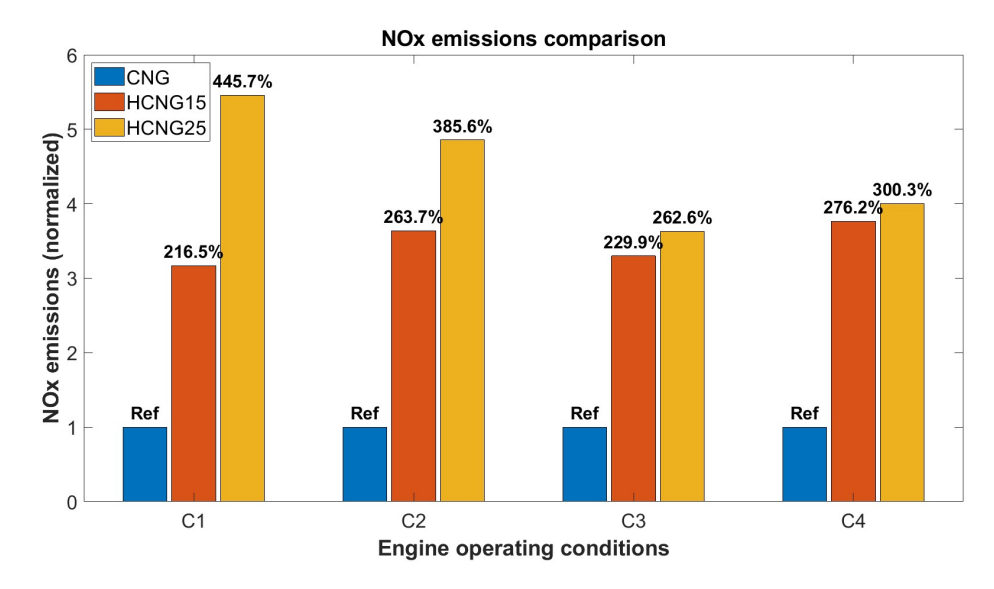


Figure 2.66:  $NO_x$  normalised emissions comparison

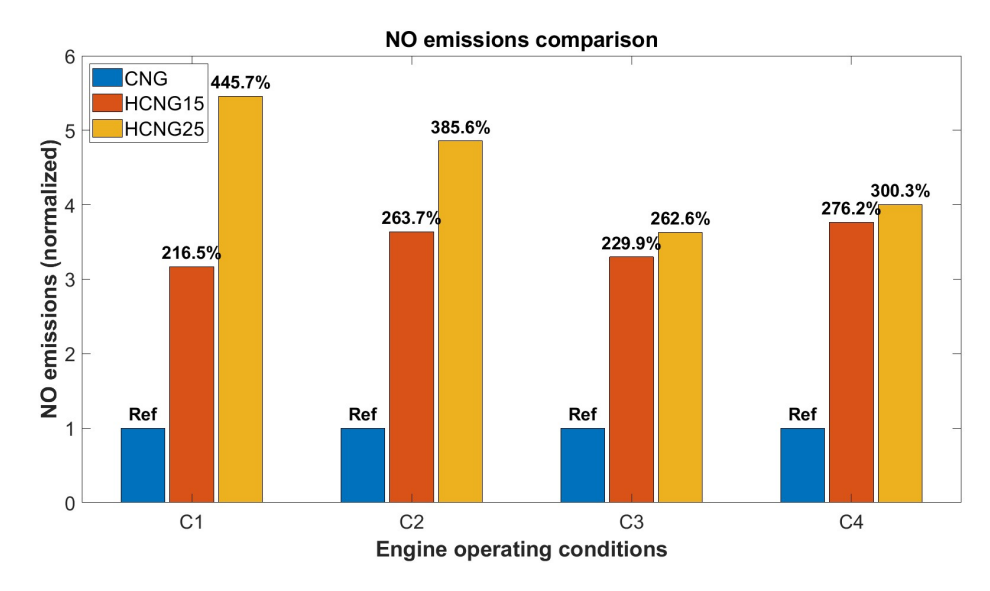


Figure 2.67: NO normalised emissions comparison

In contrast with the previous graphs, as shown in Figure 2.66-2.67, the emissions of nitrogen oxides ( $NO_x$ ) and nitrogen monoxide (NO) increase when the hydrogen is added to the fuel blend. The difference between these pollutants is that  $NO_x$  includes all nitrogen oxides, while NO refers only to the monoxide species. The increase in emissions is caused by the higher flame temperature present in the combustion chamber with the blend. As reported in section 1.4, three conditions must be simultaneously satisfied for  $NO_x$  formation: sufficient time for the reactions to occur, high oxygen concentration, and high combustion temperature. When the last condition increases due to the presence of hydrogen in the blend, the emissions of both nitrogen monoxide and nitrogen oxides consequently increase.

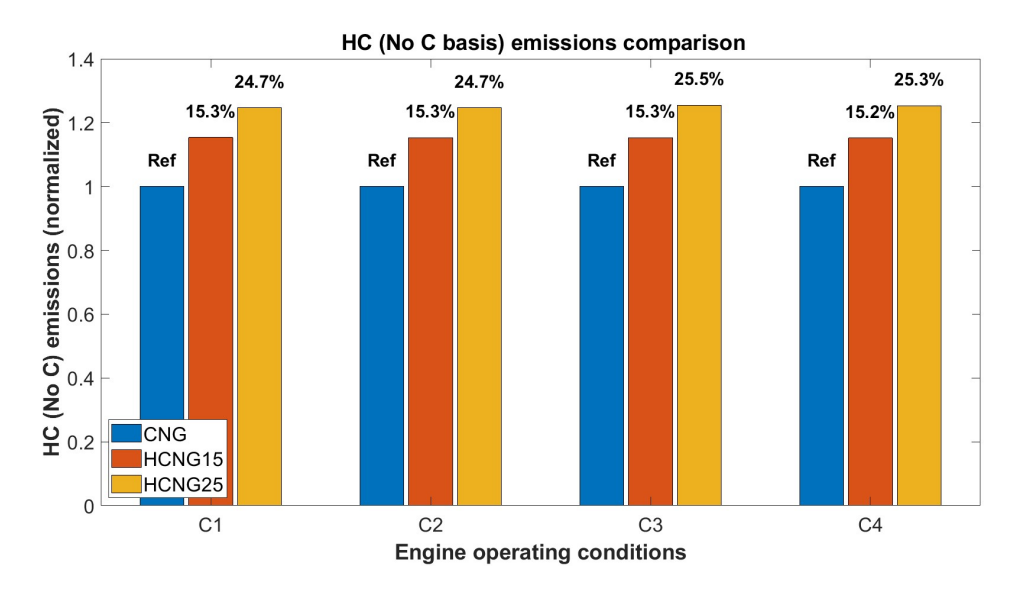


Figure 2.68: HC (No C basis) normalised emissions comparison

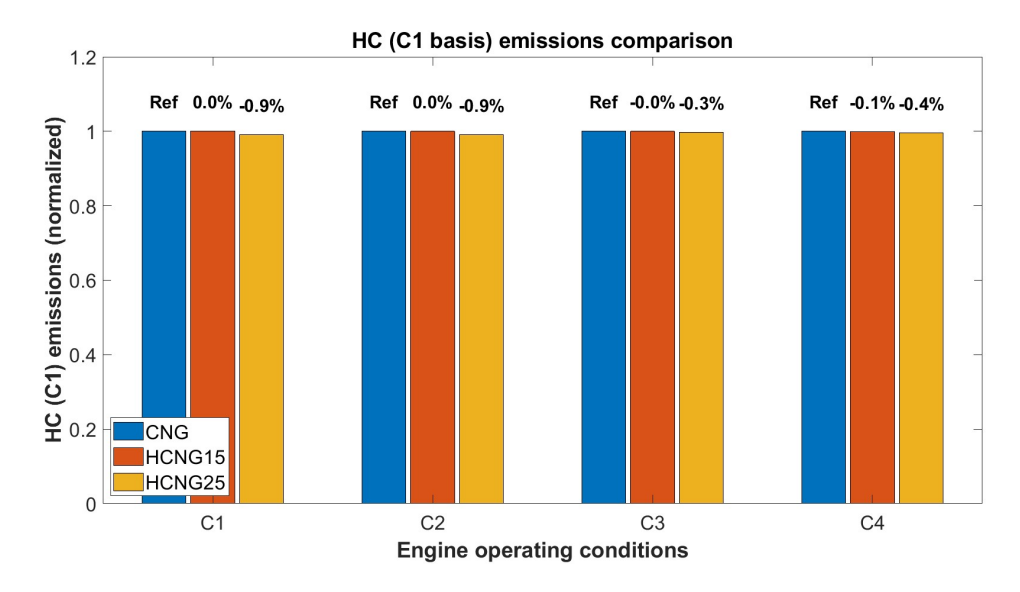


Figure 2.69: HC (C1 basis) normalised emissions comparison

This last Graphs 2.68-2.69 compares the hydrocarbon concentration emitted. The difference between them lies in the way hydrocarbons are expressed. The first one, HC (No C basis), counts each hydrocarbon molecule as a single unit, without considering the number of carbon atoms it contains. In the second one, HC C1, the hydrocarbon molecules are normalised to a methane equivalent molecule. As can be observed, the amount of HC (No C basis) increases when hydrogen is added to the blend. This is because this type of hydrocarbon division includes heavy or intermediate hydrocarbons formed during the combustion process. Since the hydrogen increases the flame speed and modifies the local combustion dynamics, potentially creating microzones with rapid but not uniform combustion, which promotes the formation of intermediate products and leads to higher HC (No C basis) emissions. In contrast, HC C1 emissions remain practically constant

because the methane is highly reactive and is almost completely oxidised even in the presence of hydrogen. Since HC C1 normalises all other hydrocarbons as methane equivalent molecules, it does not include heavy hydrocarbons, and the total amount remains roughly constant.

Overall, observing the graphs of the main pollutants, the trends reported in the literature are confirmed:  $CO_2$  and CO emissions decrease,  $NO_x$  and NO emissions increase.

### 2.5.4 Effect of spark advance on combustion

This study was carried out to analyse the effect of changing the spark advance (SA) in the mixture of methane and hydrogen. The spark advance is retarded to mitigate the risk of pre-ignition caused by the hydrogen. As previously discussed, hydrogen has high flammability, and if the spark advance is high, the mixture may pre-ignite, potentially igniting while the intake valves are still open, which could damage the system. The probability of pre-ignition is intrinsic to hydrogen, as it lowers the ignition temperature and can burn under both rich and lean conditions, increasing the risk that microzones in the mixture reach the critical conditions for pre-ignition before the programmed spark. With low hydrogen concentration, as considered in this study, retarding the spark advance towards the top dead centre (TDC) can reduce this risk. In this analysis, the centre of combustion (CoC) is kept constant, allowing the isolation of the effect of the spark advance without introducing other variables and maintaining conditions consistent with the previous analysis. In the figures below, the burn rate profiles are reported only for the HCNG15 cases, since the real burn rate of the HCNG25 mixture, as described in section 2.5.1, is obtained from the TPA analysis of the 15% hydrogen mixture. Consequently, including the HCNG25 graphs would not provide any additional information.

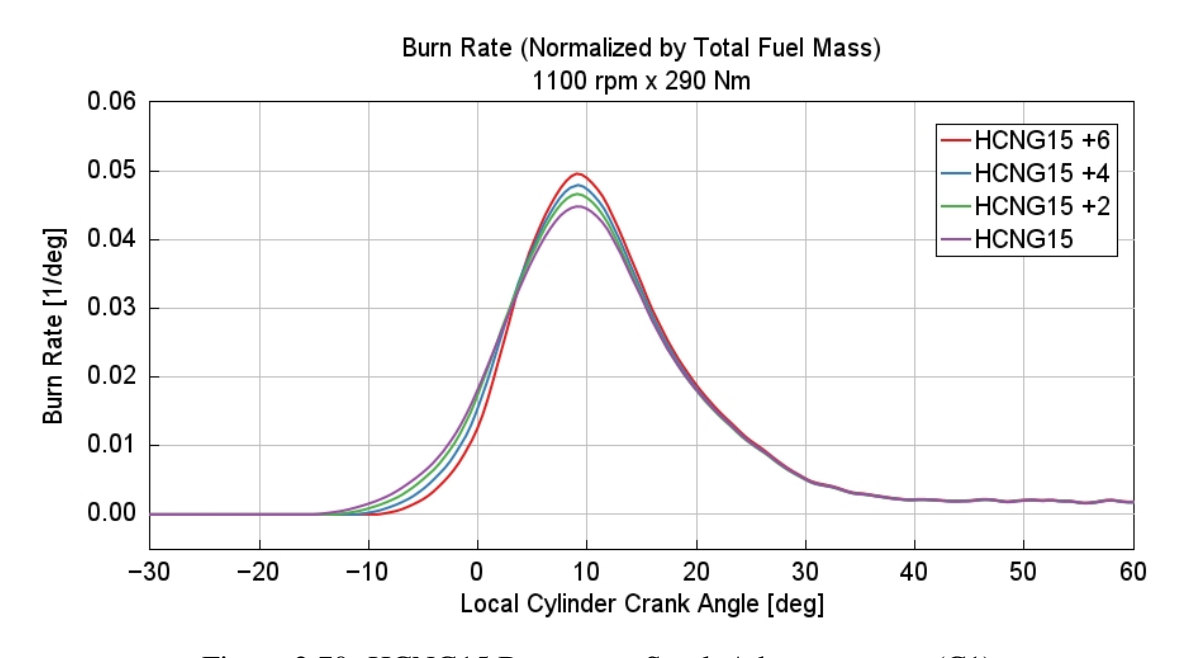


Figure 2.70: HCNG15 Burn rate - Spark Advance sweep (C1)

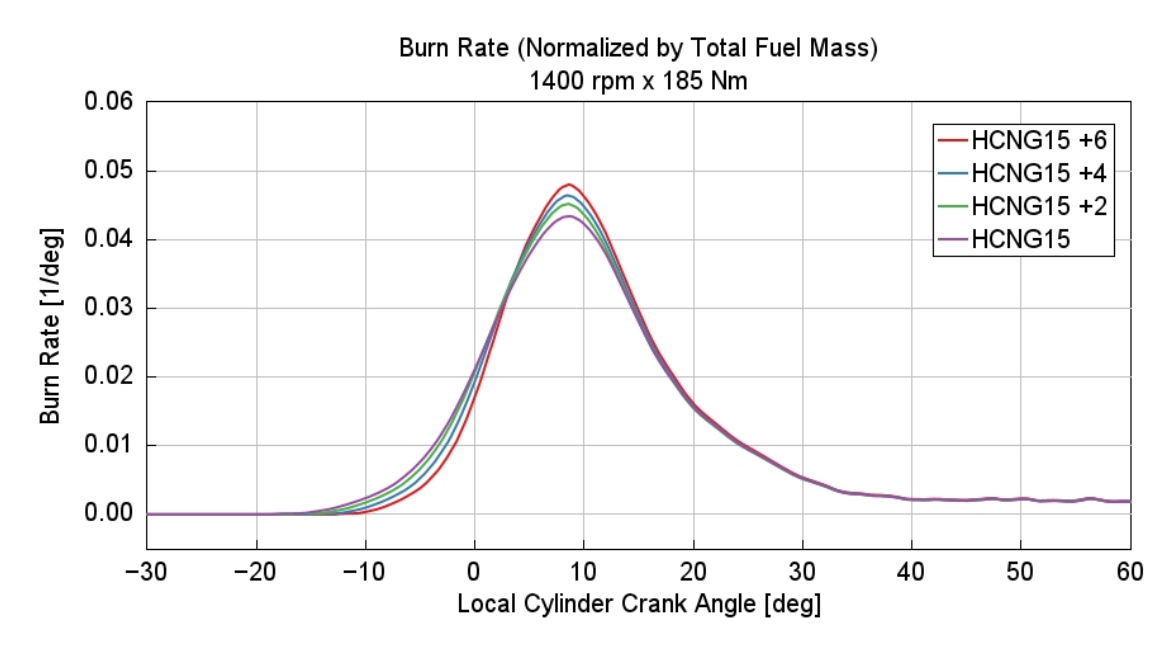


Figure 2.71: HCNG15 Burn rate - Spark Advance sweep (C2)

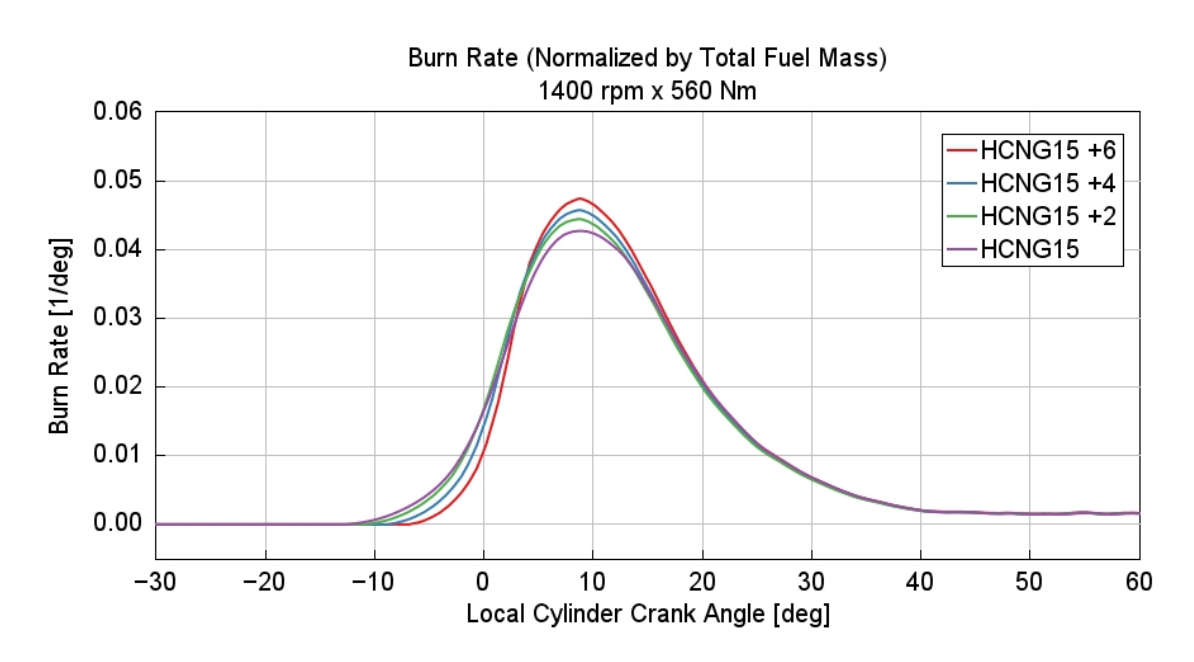


Figure 2.72: HCNG15 Burn rate - Spark Advance sweep (C3)

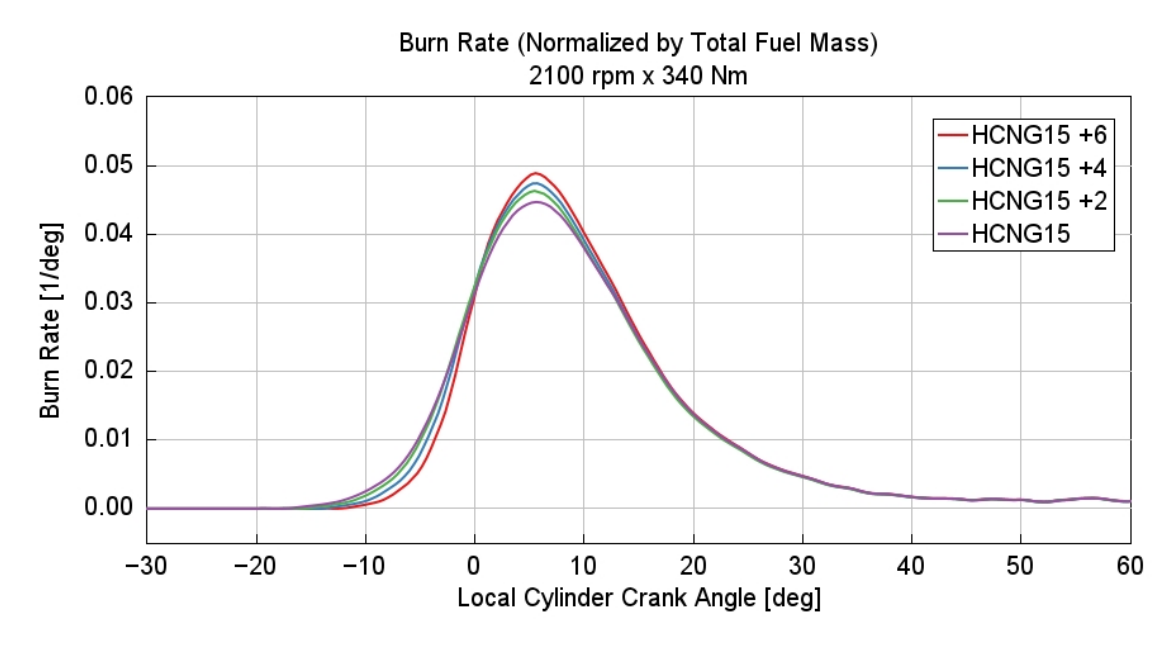


Figure 2.73: HCNG15 Burn rate - Spark Advance sweep (C4)

Observing Figures 2.70–2.73, the effect of changing the spark advance on the burn rate is clearly visible. Moving from the normal spark advance to a value 6 degrees closer to TDC (red curve), it is evident that the start of combustion is delayed, while the peak burn rate is increased. This effect is also reflected in the in-cylinder pressure traces shown below. In the following figures, as in previous sections, only the results for the HCNG15 analysis are reported.

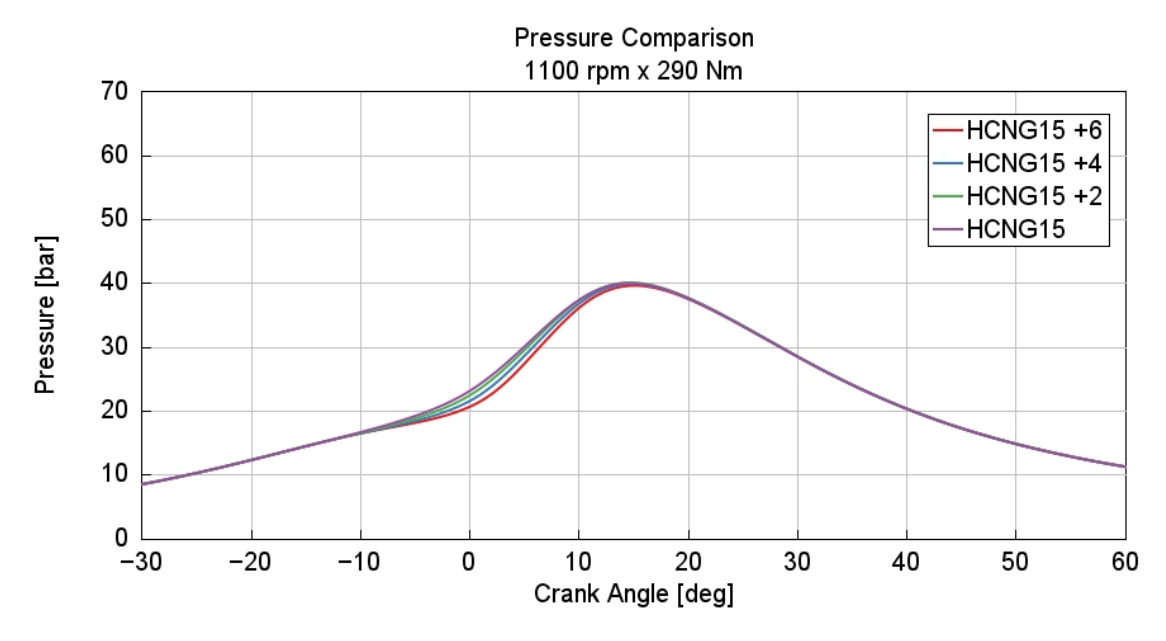


Figure 2.74: HCNG15 In-cylinder pressure - Spark Advance sweep (C1)

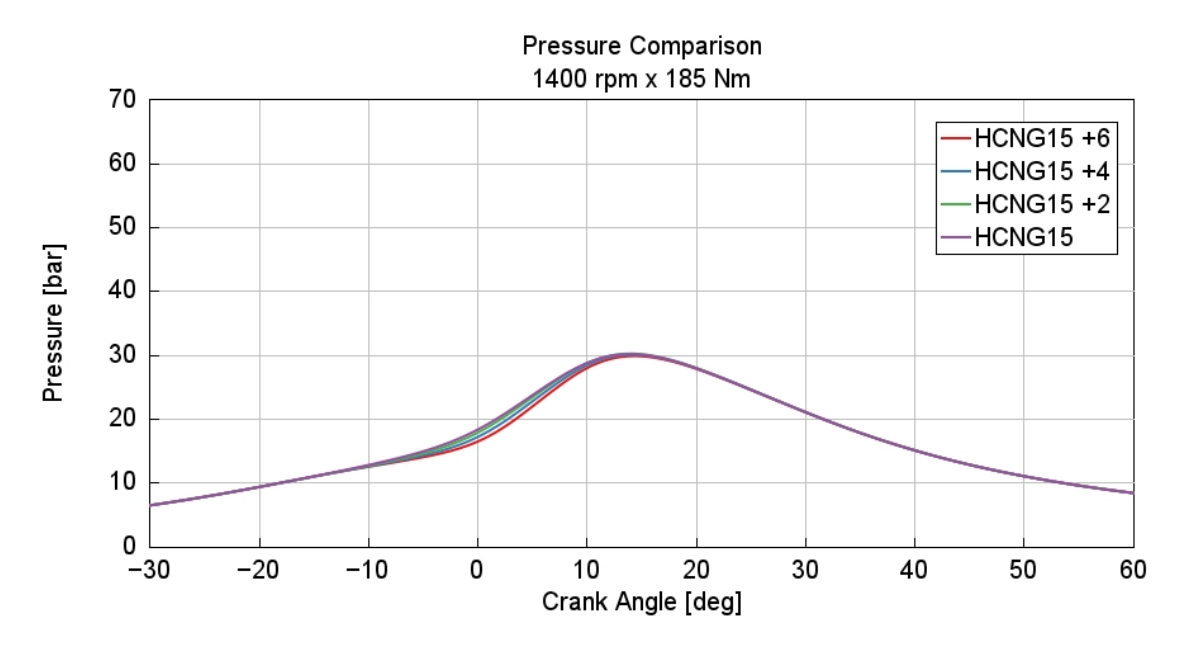


Figure 2.75: HCNG15 In-cylinder pressure - Spark Advance sweep (C2)

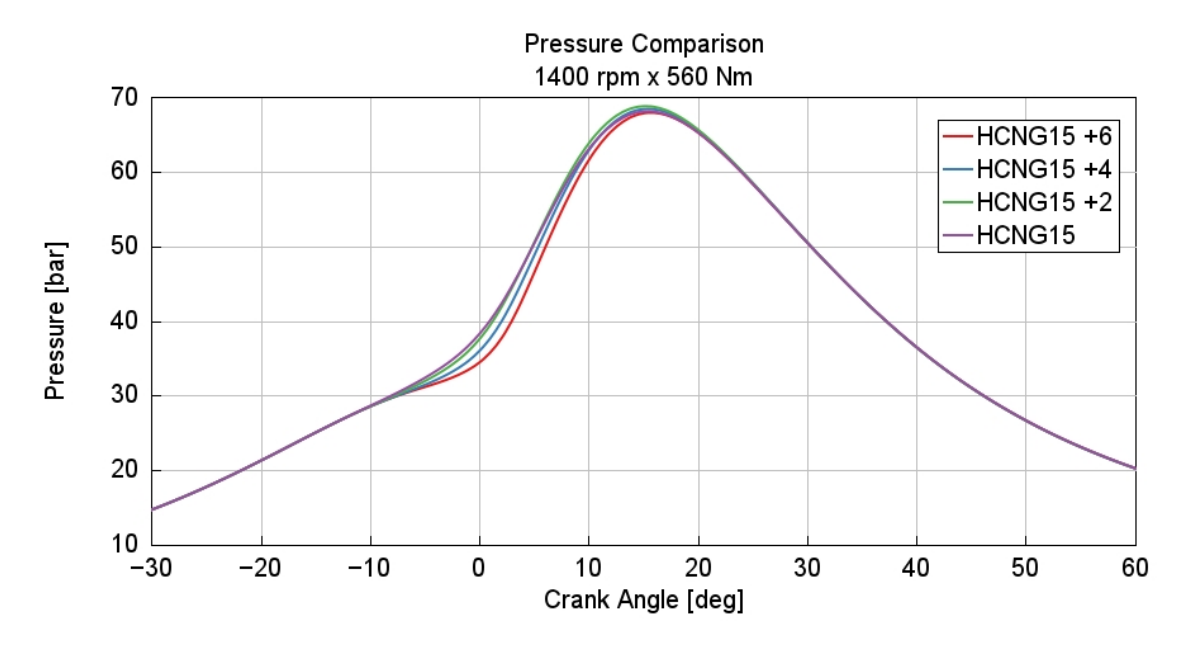


Figure 2.76: HCNG15 In-cylinder pressure - Spark Advance sweep (C3)

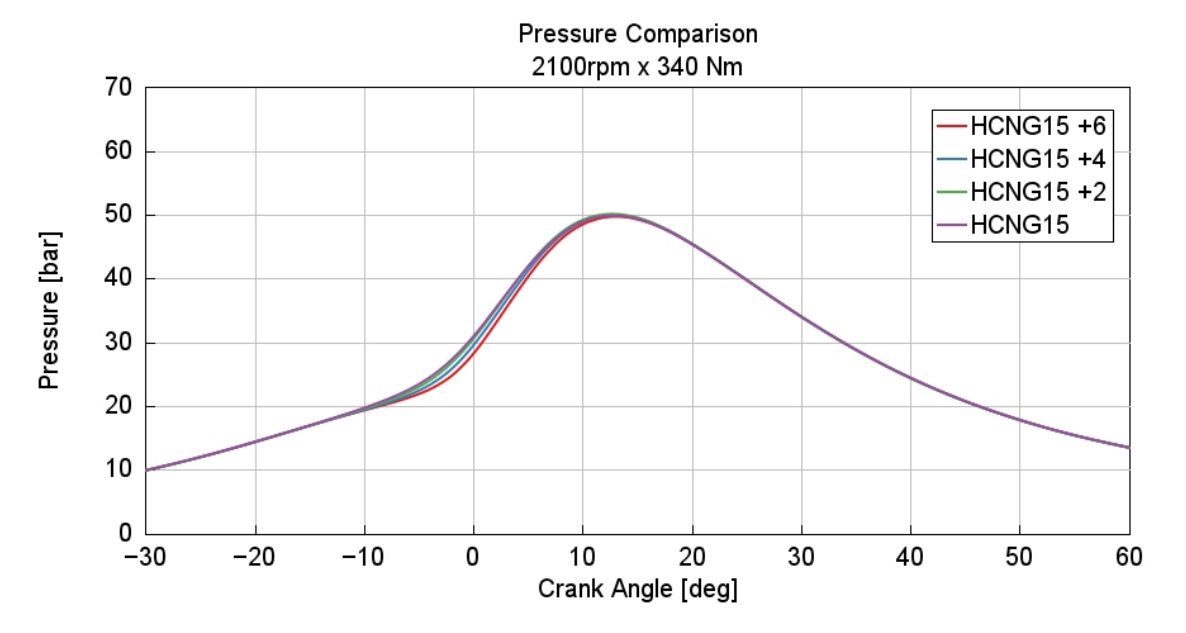


Figure 2.77: HCNG15 In-cylinder pressure - Spark Advance sweep (C4)

Looking at these graphs, the effect of varying the spark advance while keeping the combustion centre constant becomes clearer. When the ignition is retarded, the combustion starts later and therefore evolves slowly during the expansion phase. The in-cylinder pressure does not reach an early peak but is instead distributed over a longer crank angle range. Moreover, since the combustion centre is constrained to remain fixed, the average position of the combustion phasing is always the same. To respect this condition, when the spark advance is retarded, the conversion efficiency decreases and the burn rate profile must be stretched, adapting to a combustion process that develops over a longer duration.

## 2.6 Knock analysis

The last steady-state study focused on abnormal combustion, with particular attention to knock. Knock occurs when the end gas autoignites before the flame front arrives, resulting in an abrupt heat release and a sudden increase in in-cylinder pressure, generating pressure oscillations that propagate at the speed of sound, causing the engine structure to vibrate and produce a characteristic metallic noise. Thus, knock occurrence can be seen as a race between the propagation of the flame front and the autoignition of the end gas. Knock can cause significant engine damage, especially if it is very severe. Repeated knock occurrences can modify the thermal boundary layer close to the walls, favouring the preignition. This is an abnormal ignition phenomenon consisting of an anomalous ignition of the mixture before the spark, typically verified due to surface ignition near the immediate location of the hot spot (such as spark plug and exhaust valves). Due to these considerations, knock must be avoided to prevent partial or permanent damage to the engine. This analysis was performed because the addition of hydrogen increases the knock

tendency, as hydrogen has a higher flame speed and wider flammability limits compared to methane. This can lead to faster pressure rise and earlier auto ignition. Moreover, mixture reactivity increases with the presence of hydrogen, making it more sensitive to temperature and pressure variations, further enhancing the probability of knock. As highlighted in this study, it is crucial to identify the operating conditions that promote knock tendency so that they can be either avoided or properly mitigated.

In this study, the knock tendency is investigated using a Wiebe function as the combustion object of the engine model and two different knock models developed by Gamma Technologies in GT-ISE:

• **Kinetics-Fit-Natural-Gas (KNG)**: This model is based on detailed kinetics simulations. The fuel used for the kinetic reaction mechanism is natural gas or mixtures containing it. Knock occurrence is predicted using empirical induction time correlations. The induction time integral is defined as:

$$I(t) = \int_0^t \frac{1}{\tau} dt \tag{2.14}$$

where I is the induction time integral, t is the elapsed time from the start of the end-gas compression, and  $\tau$  is the induction time, which in this case is given by:

$$\tau = M_1 \cdot 1.9858 \cdot 10^{-9} \cdot \exp\left(\frac{18659}{M_2 \cdot T}\right) \left(\frac{MN}{100}\right)^{0.978} [\text{Fuel}]^{-0.578} [\text{O}_2]^{-0.28} [\text{Diluent}]^{0.03}$$
(2.15)

where  $M_1$  is the Knock Induction Time Multiplier, MN is the Fuel Methane Number,  $M_2$  is the Activation Energy Multiplier, [Fuel],  $[O_2]$ , and [Diluent] are concentrations expressed in mol/m<sup>3</sup>. The diluent concentration is the sum of the concentrations of  $N_2$ ,  $CO_2$ ,  $H_2O$ ,  $SO_2$ , and Ar. Knock is predicted to occur at the crank angle at which the induction time integral (for any end-gas zone) reaches a value of 1.0.

• **Kinetics-Fit-Hydrogen** (**KH**): This model is based on detailed kinetics simulations and uses an artificial network to capture the different chemistry of auto ignition over a wide range of pressures, temperature, and mixture compositions. The fuel used for the kinetic reaction is hydrogen or mixtures containing it.

$$I(\alpha) = \frac{1}{6 \cdot RPM} \int_{SOC}^{\alpha} \frac{1}{M_1 C_1 \left(\frac{ON}{100}\right)^{C_2} p^{-C_3} \exp\left(\frac{C_4}{M_2 T}\right)} d\alpha \qquad (2.16)$$

where SOC is the start of the cycle,  $\alpha$  is the crank angle, RPM is the engine speed, ON is the fuel octane number, p is the instantaneous cylinder pressure (Pa), T is the instantaneous unburned gas temperature (K), and  $C_1$ ,  $C_2$ ,  $C_3$ , and  $C_4$  are coefficients.

As in the previous case, knock is predicted when the induction time integral reaches a value of 1.0.

The analyses were conducted at two different engine operating points:  $1400 \text{ rpm} \times 560 \text{ Nm}$  (corresponding to 75% of full load, previously called C3) and  $1400 \text{ rpm} \times 750 \text{ Nm}$  (full load, from now on referred to as C5). These operating points were selected since knock tendency is generally higher at low engine speeds and high loads.

Typically, the knock tendency is evaluated and becomes visible by observing the incylinder pressure traces, which show pressure oscillations in the cycle phase in which this phenomenon occurs. In the present analysis, such oscillations could not be clearly observed, probably because the knock intensity was very low and the corresponding pressure oscillations were too small. However, knock detection was carried out by monitoring other parameters:

- **Knock Probability:** is equal to 0 when knock is absent and 1 when knock is present.
- Crank Angle at Knock Onset: indicates the crank angle at which the phenomenon occurs.

The latter parameter makes it possible to analyse how the knock onset varies with changing engine operating conditions. The engine parameters investigated through sweeps were: compression ratio, spark advance, and intake pressure. Only the results for the less severe case (C3) are reported here, since knock tendency was already observed under these conditions. The results corresponding to the other operating point are reported in Appendix A.

#### **Compression Ratio sweep analysis**

The effect of increasing the compression ratio (CR) was evaluated. A higher CR results in greater mixture compression, leading to increased end-gas temperature and pressure. This shortens the autoignition delay, raising the knock tendency. In the engine model, the baseline CR was 10.3 and was increased to 11.5. Further increase was not feasible due to the risk of piston-to-head interference.

As shown in Table 2.18, no knock occurrence was observed when the compression ratio was increased up to 11.5. Probably, with further modifications to the engine geometry allowing higher compression ratios, knock phenomena could appear. The analyses performed with the other knock model are not reported, as the results in terms of crank angle at knock onset and knock probability are identical to those already presented. In this analysis, the engine efficiency was also evaluated to assess the variation of this parameter with increasing CR.

	CNO	G	HCNO	G15	HCNO	G25
CR	Crank Angle at Knock Onset [deg]	Knock Probability	Crank Angle at Knock Onset [deg]	Knock Probability	Crank Angle at Knock Onset [deg]	Knock Probability
10.3	_	0	-	0	-	0
10.4	_	0	_	0	-	0
10.5	-	0	-	0	-	0
10.6	-	0	_	0	-	0
10.7	-	0	_	0	-	0
10.8	_	0	_	0	-	0
10.9	-	0	_	0	-	0
11.0	_	0	_	0	-	0
11.1	-	0	_	0	-	0
11.2	-	0	-	0	-	0
11.3	-	0	-	0	-	0
11.4	-	0	-	0	-	0
11.5	-	0	-	0	-	0

Table 2.18: Crank Angle at Knock Onset and Knock Probability - KNG knock model - CR sweep (C3)

As reported in Table 2.19, an increase in compression ratio leads to higher brake efficiency in the CNG case, as the in-cylinder mixture is subjected to higher pressure and temperature conditions. As brake efficiency increases, the bsFC consequently decreases. For the HCNG cases, a slight decrease in brake efficiency can be observed, likely due to model limitations and the relatively small increase in compression ratio. However, in the full load condition, as shown in Table A.1.2, a slight increase in engine efficiency is observed. Overall, this analysis demonstrates that increasing the compression ratio up to 11.5 does not increase the knock probability, while it can improve engine efficiency.

CR	CNG	HCNG15	HCNG25
	Brake Efficiency [%]	Brake Efficiency [%]	Brake Efficiency [%]
10.3	31.522	32.862	33.006
10.4	31.585	32.935	33.047
10.5	31.649	32.988	33.111
10.6	31.712	33.044	33.165
10.7	31.771	33.089	33.228
10.8	31.831	33.154	33.268
10.9	31.890	33.197	33.337
11.0	31.949	33.251	33.366
11.1	32.004	33.290	33.426
11.2	32.059	33.338	33.458
11.3	32.112	33.384	33.516
11.4	32.164	33.428	33.548
11.5	32.216	33.444	33.589

Table 2.19: Brake Efficiency - KNG knock model - CR sweep (C3)

#### Spark Andvance sweep analysis

This analysis was carried out to evaluate the effect of advancing combustion on knock tendency. By anticipating the spark advance, and consequently the ignition timing, combustion is initiated while the piston is still in the compression phase. This leads to an increase in in-cylinder pressure and temperature, which in turn raises the probability of autoignition. To verify whether this theoretical trend is also reflected in the experimental model, an analysis was performed in which the spark advance was increased up to 48° with respect to the reference value. The corresponding results are reported in Table 2.20.

	CNO	G	HCNO	G15	HCNO	G25
SA [deg]	Crank Angle at Knock Onset [deg]	Knock Probability	Crank Angle at Knock Onset [deg]	Knock Probability	Crank Angle at Knock Onset [deg]	Knock Probability
Ref	-	0	-	0	-	0
-4	-	0	-	0	-	0
-8	-	0	-	0	-	0
-12	-	0	-	0	-	0
-16	-	0	-	0	-	1
-20	-	0	-	0	10.55	1
-24	8.45	1	10.64	1	4.02	1
-28	2.58	1	4.17	1	0.28	1
-32	-1.16	1	0.67	1	-2.50	1
-36	-4.00	1	-1.81	1	-4.70	1
-40	-6.29	1	-3.69	1	-6.47	1
-44	-8.16	1	-5.20	1	-7.90	1
-48	-9.69	1	-6.40	1	-9.09	1

Table 2.20: Crank Angle at Knock Onset and Knock Probability - KNG knock model - SA sweep (C3)

Looking at the table above, the previously described trend is confirmed, as the occurrence of knock becomes evident. Knock starts to appear at a spark advance of approximately 24° for the CNG and HCNG15 cases, and at around 22° for the HCNG25 case. This behavior is attributable to the higher hydrogen concentration, which enhances the knock tendency. Furthermore, it is clear that up to a certain spark advance, the crank angle at knock onset exhibits positive values, meaning that knock occurs after Top Dead Center (TDC). However, when the spark advance becomes too high, this value shifts toward negative values, indicating that knock starts to develop before TDC. Instead, the analysis performed with the Kinetic-Fit-Hydrogen model, as reported in Table 2.21, indicates a knock tendency at lower spark advance values compared to those obtained with the Natural-Gas model. With this model, knock occurs at 16° of spark advance for both fuels, whereas higher values were required with the previous model.

	HCNG15		HCNG25	
SA [deg]	Crank Angle at Knock Onset [deg]	Knock Probability	Crank Angle at Knock Onset [deg]	Knock Probability
Ref	-	0	-	0
-4	-	0	-	0
-8	-	0	-	0
-12	-	0	-	0
-16	10.48	1	7.66	1
-20	3.73	1	2.28	1
-24	-0.24	1	-1.39	1
-28	-3.23	1	-4.27	1
-32	-5.66	1	-6.67	1
-36	-7.68	1	-8.71	1
-40	-9.35	1	-10.42	1
-44	-10.77	1	-11.85	1
-48	-11.93	1	-13.07	1

Table 2.21: Crank Angle at Knock Onset and Knock Probability - KH knock model - CR sweep (C3)

In this analysis as well, brake efficiency is evaluated to assess the effect of spark advance on the combustion process.

	CNG	HCNG15	HCNG25
SA [deg]	Brake Efficiency [%]	Brake Efficiency [%]	Brake Efficiency [%]
Ref	31.522	32.862	33.006
-4	31.535	32.832	32.981
-8	31.141	32.332	32.464
-12	30.340	31.381	31.526
-16	29.148	30.044	30.178
-20	27.612	28.345	28.517
-24	25.780	26.353	26.566
-28	23.720	24.150	24.376
-32	21.489	21.813	22.007
-36	19.147	19.370	19.611
-40	16.737	16.887	17.132
-44	14.307	14.427	14.626
-48	11.889	11.965	12.181

Table 2.22: Brake Efficiency - KNG knock model - SA sweep (C3)

The results obtained from this analysis show a decrease in brake thermal efficiency and, consequently, an increase in fuel consumption as the spark advance increases. This phenomenon occurs because advancing the spark shifts the combustion phasing away from the Maximum Brake Torque (MBT) crank angle, where efficiency is highest, thus reducing overall efficiency. Moreover, when combustion starts while the piston is still in the compression stroke and moving upward, part of the energy released by combustion opposes the piston's motion instead of contributing to useful work, further decreasing efficiency. Therefore, increasing the spark advance does not provide significant benefits,

since it leads to lower combustion efficiency, higher fuel consumption, and an increased knock tendency. In addition, since the analysis was initially carried out with a reference compression ratio of 10.3, a further evaluation was conducted by increasing the compression ratio up to the limit value of 11.5, in order to assess potential differences. The study showed that the results were identical to those obtained with the reference compression ratio, with no variation in the crank angle of knock onset, and identical values of brake efficiency and brake specific fuel consumption.

#### **Intake Pressure sweep analysis**

The intake pressure was increased to enhance the knock tendency of the mixture. This occurs because a higher intake pressure increases the mass of fresh charge inside the cylinder, which results in a higher effective compression ratio as well as higher in-cylinder pressure and temperature. For this analysis, the intake pressure was raised up to 150% of the reference value.

		CNG			HCNG15			HCNG25	
	Pint [bar]	Crank Angle	Knock	Pint [bar]	Crank Angle	Knock	Pint [bar]	Crank Angle	Knock
	riii [bar]	at Knock Onset [deg]	Probability	riii [bar]	at Knock Onset [deg]	Probability	riii (bar)	at Knock Onset [deg]	Probability
Ref	1.33	-	0	1.37	-	0	1.40	-	0
+10%	1.47	-	0	1.51	-	0	1.54	-	0
+20%	1.60	-	0	1.65	-	0	1.68	-	0
+30%	1.73	-	0	1.79	-	0	1.82	-	0
+40%	1.87	-	0	1.92	_	0	1.96	_	0
+50%	2.00	-	0	2.06	-	0	2.10	-	0
+60%	2.13	-	0	2.20	-	0	2.24	23.73	0
+70%	2.27	_	0	2.33	23.46	0	2.38	19.09	0
+80%	2.40	-	0	2.47	19.34	0	2.52	16.73	0
+90%	2.53	-	0	2.61	17.03	0	2.66	15.16	0
+100%	2.67	_	0	2.75	15.51	0	2.80	13.99	0
+110%	2.80	-	0	2.88	14.41	0	2.94	13.10	0
+120%	2.93	-	0	3.02	13.55	0	3.08	12.48	0
+130%	3.07	_	0	3.16	13.02	0	3.22	12.07	0
+140%	3.20	-	0	3.30	12.79	0	3.36	12.30	0
+150%	3.33	-	0	3.43	13.26	0	3.50	12.90	0

Table 2.23: Crank Angle at Knock Onset and Knock Probability - KNG knock model - Intake Pressure sweep (C3)

Table 2.23 shows that knock appears for the hydrogen-methane mixtures as the intake pressure increases, specifically at 2.33 bar for HCNG15 and 2.24 bar for HCNG25. In contrast, no knock tendency is observed in the CNG case. When using the Kinetic-Fit-Hydrogen model, the intake pressure required for knock onset, and consequently the corresponding crank angle, differ from those obtained with the Kinetic-Fit-Natural-Gas model, as reported in Table 2.24. In this case, knock is triggered by a 50% intake pressure increase from the reference value, compared to 70% for HCNG15 and 60% for HCNG25 with the Natural-Gas model. Although the crank angle of knock onset remains positive in all cases, it shifts progressively closer to TDC as intake pressure increases.

		HCNG15			HCNG25	
	Pint [bar]	Crank Angle at Knock Onset [deg]	Knock Probability	Pint [bar]	Crank Angle at Knock Onset [deg]	Knock Probability
Ref	1.37	_	0	1.40	-	0
+10%	1.51	_	0	1.54	-	0
+20%	1.65	-	0	1.68	-	0
+30%	1.79	_	0	1.82	_	0
+40%	1.92	-	0	1.96	-	0
+50%	2.06	27.30	0	2.10	23.83	0
+60%	2.20	19.57	0	2.24	18.67	0
+70%	2.33	16.86	0	2.38	16.33	0
+80%	2.47	15.20	0	2.52	14.81	0
+90%	2.61	13.95	0	2.66	13.71	0
+100%	2.75	13.02	0	2.80	12.85	0
+110%	2.88	12.31	0	2.94	12.18	0
+120%	3.02	11.74	0	3.08	11.74	0
+130%	3.16	11.42	0	3.22	11.48	0
+140%	3.30	11.34	0	3.36	11.87	0
+150%	3.43	11.91	0	3.50	12.64	0

Table 2.24: Crank Angle at Knock Onset and Knock Probability - KH knock model - Intake Pressure sweep (C3)

The efficiency parameter is reported in Table 2.25.

		CNG		HCNG15		HCNG25
	Pint [bar]	Brake Efficiency [%]	Pint [bar]	Brake Efficiency [%]	Pint [bar]	Brake Efficiency [%]
Ref	1.33	31.522	1.37	32.862	1.40	33.006
+10%	1.47	32.434	1.51	34.213	1.54	34.321
+20%	1.60	33.195	1.65	35.257	1.68	35.374
+30%	1.73	33.834	1.79	36.180	1.82	36.309
+40%	1.87	34.399	1.92	37.017	1.96	37.146
+50%	2.00	34.872	2.06	37.781	2.10	37.906
+60%	2.13	35.301	2.20	38.493	2.24	38.615
+70%	2.27	35.678	2.33	39.154	2.38	39.270
+80%	2.40	36.013	2.47	39.765	2.52	39.885
+90%	2.53	36.310	2.61	40.338	2.66	40.462
+100%	2.67	36.583	2.75	40.880	2.80	41.007
+110%	2.80	36.843	2.88	41.392	2.94	41.521
+120%	2.93	37.089	3.02	41.878	3.08	42.008
+130%	3.07	37.319	3.16	42.341	3.22	42.473
+140%	3.20	37.519	3.30	42.784	3.36	42.916
+150%	3.33	37.722	3.43	43.208	3.50	43.340

Table 2.25: Brake Efficiency - KNG knock model - Intake Pressure sweep (C3)

Increasing the intake pressure leads to an increase in the engine's brake efficiency. This occurs because, as previously explained, the mass of fresh charge trapped in the cylinder increases. When the stoichiometric condition is maintained, more fuel is injected, providing additional energy for combustion. From this analysis, it was observed that increasing the intake pressure improves engine efficiency and reduces fuel consumption, while simultaneously enhancing the knock tendency. As explained for the spark advance sweep, this analysis was performed using the reference compression ratio. When the compression ratio is increased to its limit value, the intake pressure required to induce knock decreases, as shown in Table A.3.4, indicating a higher knock tendency. This occurs be-

cause a higher compression ratio increases the in-cylinder pressure, thereby reducing the additional intake pressure needed to trigger knock.

### **Combined Spark Advance and Intake Pressure Sweep Analysis**

In this study, a combined analysis was performed by keeping the compression ratio constant at 11.5 while simultaneously varying the intake pressure and spark advance within the previously described intervals to investigate the effect of their combined values on the knock tendency of the mixture. To keep the discussion concise, only the case at 1400 rpm × 560 Nm with the HCNG25 mixture using the Kinetic-Fit-Natural-Gas knock model is presented here, as the same considerations apply to all operating conditions. The only differences lie in the specific values of the crank angle at knock onset, which can be directly compared in the Tables reported in Appendix A.

As shown in Table 2.26, performing combustion with the compression ratio increased to 11.5 leads to knock occurring at lower operating parameter values, resulting in a higher number of knocking conditions. It can be observed that the relationship between intake pressure and spark advance is reciprocal: when intake pressure increases, the spark advance required to induce knock decreases, and vice versa. Furthermore, beyond a certain spark advance, all crank angles of knock onset become negative, as explained in the previous analyses.

							SA	[deg]						
		-48	-44	-40	-36	-32	-28	-24	-20	-16	-12	-8	-4	Ref
	Ref	-9.08	-7.91	-6.46	-4.70	-2.50	0.27	4.04	10.56	-	-	_	-	-
	+10%	-13.84	-12.54	-11.02	-9.20	-7.11	-4.65	-1.75	1.83	6.72	17.34	_	-	_
	+20%	-16.87	-15.41	-13.74	-11.84	-9.68	-7.25	-4.49	-1.28	2.62	7.86	19.02	-	-
	+30%	-19.04	-17.47	-15.68	-13.68	-11.46	-9.00	-6.26	-3.17	0.42	4.85	11.17	-	_
	+40%	-20.71	-19.01	-17.11	-15.04	-12.76	-10.29	-7.56	-4.53	-1.08	3.00	8.31	17.28	-
	+50%	-21.99	-20.21	-18.25	-16.11	-13.79	-11.27	-8.54	-5.54	-2.18	1.72	6.55	13.49	-
7	+60%	-23.05	-21.19	-19.17	-16.97	-14.61	-12.07	-9.34	-6.35	-3.04	0.74	5.29	11.38	23.74
[bar]	+70%	-23.92	-21.99	-19.91	-17.68	-15.29	-12.74	-9.98	-7.01	-3.73	-0.04	4.32	9.95	19.08
Pint	+80%	-24.66	-22.68	-20.55	-18.28	-15.86	-13.29	-10.54	-7.57	-4.32	-0.69	3.56	8.87	16.74
"	+90%	-25.30	-23.28	-21.13	-18.82	-16.38	-13.78	-11.01	-8.04	-4.82	-1.23	2.91	8.01	15.16
	+100%	-25.84	-23.79	-21.59	-19.26	-16.80	-14.20	-11.44	-8.48	-5.27	-1.72	2.34	7.30	14.00
	+110%	-26.29	-24.20	-21.98	-19.62	-17.14	-14.53	-11.77	-8.81	-5.62	-2.11	1.90	6.72	13.10
	+120%	-26.66	-24.56	-22.32	-19.95	-17.45	-14.83	-12.05	-9.10	-5.92	-2.42	1.55	6.29	12.48
	+130%	-26.92	-24.79	-22.53	-20.14	-17.63	-15.00	-12.22	-9.27	-6.09	-2.59	1.34	6.01	12.05
	+140%	-27.09	-24.94	-22.68	-20.30	-17.78	-15.13	-12.33	-9.35	-6.16	-2.64	1.35	6.09	12.30
	+150%	-27.10	-24.94	-22.64	-20.22	-17.67	-15.00	-12.18	-9.18	-5.95	-2.42	1.61	6.45	12.88

Table 2.26: HCNG25 Crank Angle at Knock Onset and Knock Probability - KNG knock model - Intake Pressure and SA sweep (C3)

The knock analysis showed that the engine model does not exhibit knock at the reference operating condition for any of the three tested mixtures, which is an important result since knock must be avoided. Knock only occurs when the intake pressure and spark advance are varied from their reference values. Increasing the compression ratio up to

11.5 does not lead to a higher knock risk, as this value is still relatively low, whereas increasing the intake pressure and spark advance clearly increases knock tendency. It is observed that the Kinetic-Fit-Hydrogen knock model is more sensitive to knock for the methane—hydrogen mixtures compared to the Natural-Gas model, exhibiting overall less severe operating conditions required to trigger it. Analysis of engine efficiency shows that efficiency improves when the compression ratio is increased, without significantly affecting knock tendency at this value. Increasing the intake pressure also improves engine efficiency but leads to a higher knock probability. Conversely, advancing the spark increases knock probability but does not improve engine efficiency.

In summary, these results indicate that engine calibration involves a careful trade-off to achieve the optimal compromise between engine efficiency, fuel consumption, and knock risk.

# Chapter 3

## Transient analysis

In the following section, the methodology used to analyse combustion with a methane and hydrogen blend under transient conditions is presented. The objective of these analyses is to verify if the model, calibrated in steady-state conditions, can be applied to a transient cycle. For this purpose, a portion of the World Harmonised Transient Cycle (WHTC) for heavy-duty was analysed.

### 3.1 WHTC description and model setup

The World Harmonised Transient Cycle (WHTC), introduced in section 1.2, is a transient test cycle carried out over 1800 seconds, including urban, extra-urban and highway segments. It is defined by an engine speed profile and a normalised load pattern (normalised to the rated power), as shown in Figure 3.1.

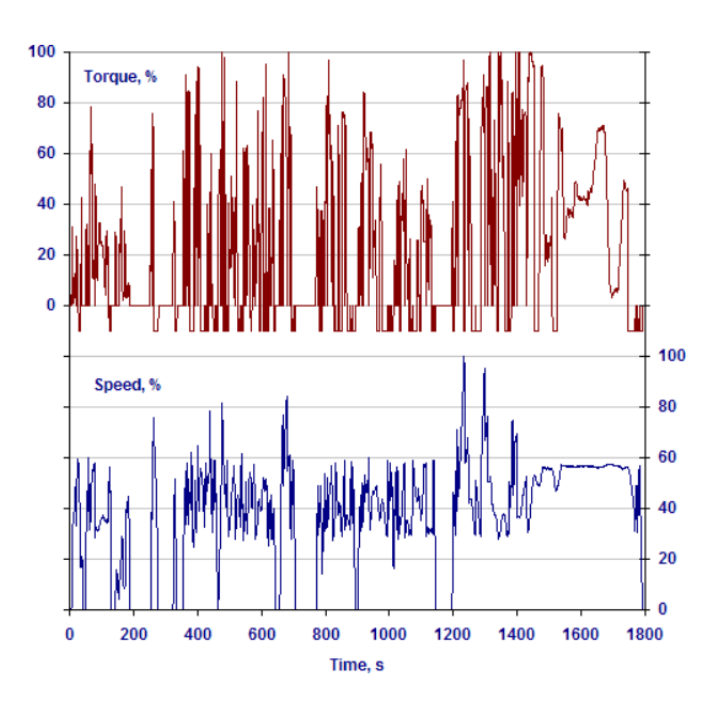


Figure 3.1: WHTC speed and load profiles [20]

To perform the analysis under transient conditions, the mono-cylinder model was replaced with the six-cylinder engine model (Figure 2.1). This choice is necessary because model control requires acting on the throttle, and consequently, the full engine model, including the turbocharging system, must be considered. Since for the control of the model, it is necessary to act on the throttle and consequently the entire engine model, comprising also the turbocompressor system, is necessary. In this configuration, the intake and exhaust pressures are no longer imposed externally but are instead determined by the corresponding operating points in the turbocharger model. The WHTC requires the imposition of both the engine speed and torque profiles. The first one is directly imposed as a function of the crank angle within the Engine block of the model. To track the torque profile during transient operations, two different controllers were implemented:

- Throttle Controller: takes engine speed and torque profile as input and compares the target torque imposed with the actual one.
- Mass Flow Controller: takes the intake air mass flow as input and compares it with the target one.

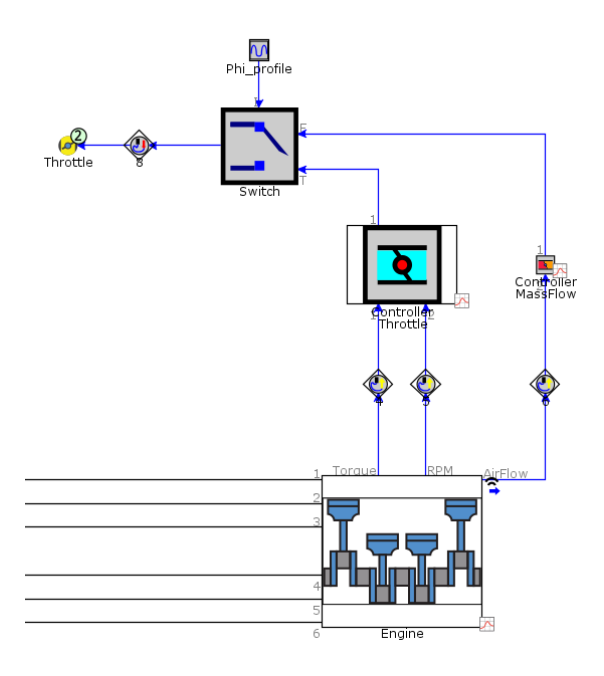


Figure 3.2: Six-cylinder engine model controller implementation

Both controllers, as illustrated in Figure 3.2, provide throttle commands to modulate the valve opening in order to reach the required engine operating conditions, according to the difference between the actual and the target value. A switching logic, based on the equivalence ratio  $(\phi)$  profile of the operating points, determines which controller is active at each time. During the transient cycle, several cut-off phases occur, phases where fuel injection is interrupted due to the absence of a positive torque demand. In these conditions, only the Mass Flow Controller can ensure correct behaviour, since the injected fuel

must be set to zero, whereas with the other controller, this condition cannot be guaranteed. Experimentally, during cut-off, the brake torque measured on the dynamometer appears negative, but from a mechanical perspective, negative torque has no physical meaning. To address this, a  $\varphi$  profile was defined: under normal operations, stochiometric conditions are imposed ( $\varphi = 1$ ), while during cut-off, no fuel is injected, corresponding to very lean conditions, hence  $\varphi = 0$ . This strategy was preferred over using  $\lambda$  profile since it tends to infinity under lean conditions, while  $\varphi$  simply drops to zero, making it easier to implement. Consequently, when  $\varphi = 1$ , the Throttle Controller is active and regulates the throttle to follow the torque profile, while when  $\varphi = 0$ , the Mass Flow Controller becomes active.

In order to verify the validity of the model, a preliminary verification was carried out on the four steady-state operating points with CNG as a fuel before performing the transient analysis. As a combustion object, the profile obtained from the TPA analysis on CNG was adopted. The results are reported in Table 3.1.

Parameters	Brake T	orque [Nm]	IMEP [bar]		BMEI	P [bar]	λ [-]		
	Exp	Sim	Exp	Sim	Exp	Sim	Exp	Sim	
C1	290.38	290.00	7.69	7.11	6.08	6.19	1	1.005	
C2	184.72	185.02	5.40	4.91	3.87	3.95	1	1.005	
C3	559.08	560.01	13.35	13.10	11.71	11.96	1	1.005	
C4	340.50	340.00	8.57	8.61	7.13	7.26	1	1.005	

Table 3.1: CNG engine performance parameters - TPA combustion model - Six-cylinder engine model

As shown in the table, the six-cylinder model is well calibrated and accurately reproduces the experimental engine performance parameters.

## 3.2 Methodology description and results

The transient analysis follows the same logic and approach as the steady-state investigations. Initially, simulations are carried out with methane as the only fuel, after the mixture blend is introduced. For the transient analysis, two different approaches are considered:

- The first relies on using a single engine operating condition as a combustion object for the entire transient analysis.
- The second is based on the implementation of a Look-Up Table (LUT), in which the four burn rates derived from the different engine operating conditions are inserted.

### 3.2.1 Single operating point combustion modelling approach

Before applying the first method, preliminary analyses are necessary. The objective is to identify the most recurrent engine operating condition within the WHTC and then select the model operating point closest to it. Specifically, the engine speed was divided into buckets of 100 rpm, while the torque was discretised into buckets of 10 Nm. This procedure enables the identification of the most frequent operating condition. In addition, the analysis was performed on the WHTC split into two phases: the first 900 seconds and the subsequent 900. Figure 3.3 shows the results obtained.

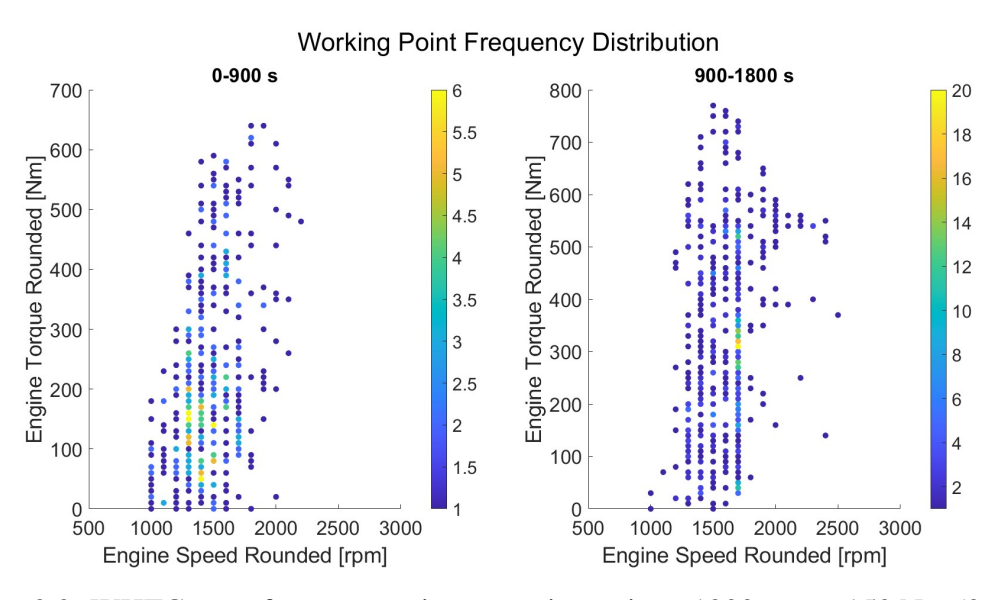


Figure 3.3: WHTC most frequent engine operating points: 1300 rpm - 150 Nm (0-900 s) and 1700 rpm - 310 Nm (900-1800 s).

In the first interval, the most frequent engine operating condition is found at 1300 rpm x 150 Nm, whereas in the second interval, it is 1700 rpm x 310 Nm. The first interval was chosen for further investigation, since its most frequent engine operating condition exhibits a similar ratio between engine speed and torque compared with the second experimental operating point (1400 rpm x 185 Nm). Consequently, for the analyses conducted with a single burn rate profile, the one obtained from the SI-TURB analysis on CNG for case C2 was adopted.

The second step was to identify an interval of 100 seconds within the first phase of the WHTC where the most frequent operating condition occurs more often. This selected interval is illustrated in Figure 3.4

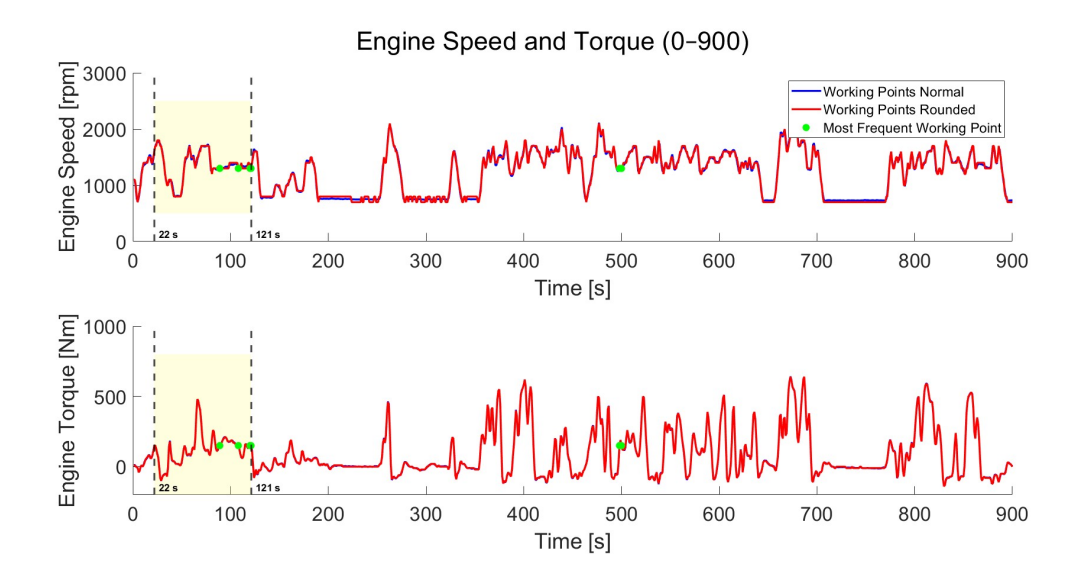


Figure 3.4: WHTC interval of the most frequent engine operating point

The analysis highlights that the time window between 22 and 121 seconds contains the highest occurrence of the target operating condition. Consequently, this interval has been selected as the reference for all subsequent analyses on the WHTC, including the ones performed with the LUT. Before the analysis, the  $\varphi$  profile must be defined in order to account for the cut-off phases within the cycle. For this purpose, a profile was implemented where  $\varphi$  is set to unity, except during the points in which the engine torque becomes negative. Figure 3.5 illustrates the imposed profile. A cut-off phase can be observed between 8 and 16 seconds.

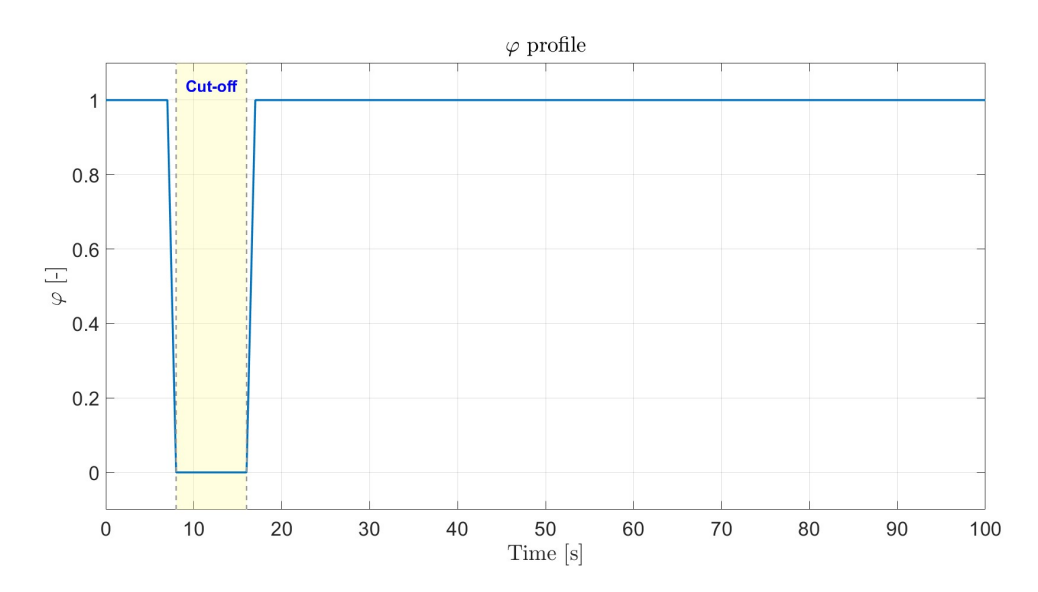


Figure 3.5:  $\varphi$  profile for the throttle controller

The resulting brake torque, fuel flow rate, and lambda profiles obtained with this analysis are reported below.

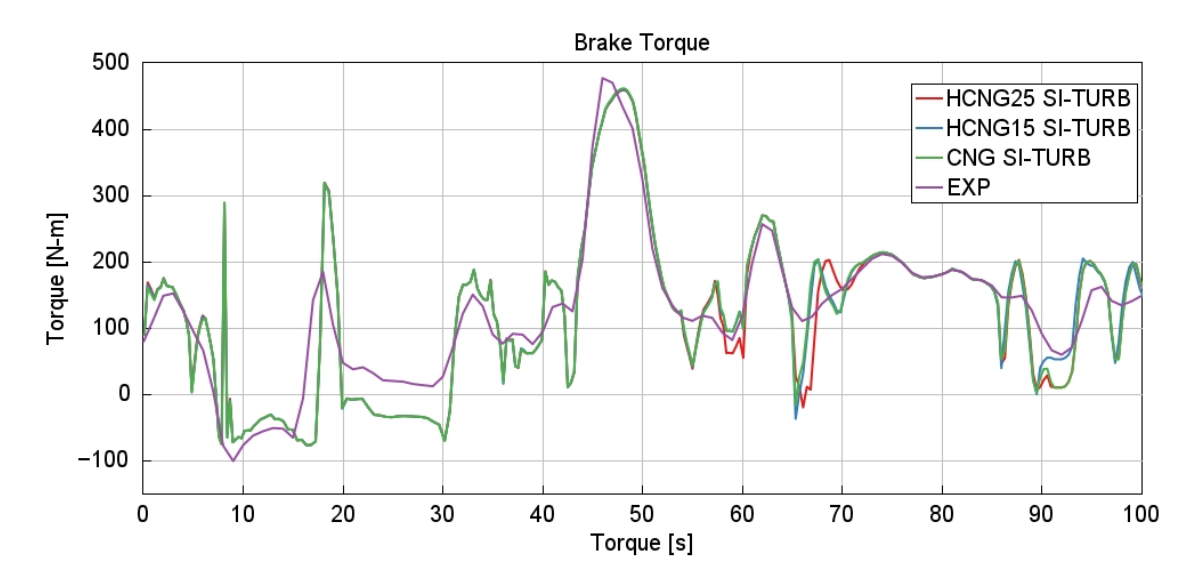


Figure 3.6: WHTC brake torque profiles - Single operating point combustion model (C2)

Looking at Figure 3.6, it is evident that the simulated brake torque profiles for all the fuels examined exhibit a marked variability and noticeable discrepancies with respect to the experimental trace (purple curve). These deviations are particularly significant in the transient phases and at torque peaks, where the simulated response is locally overestimated or underestimated. Moreover, no substantial differences can be observed between the case with pure methane and the HCNG mixtures, which overall show a very similar trend.

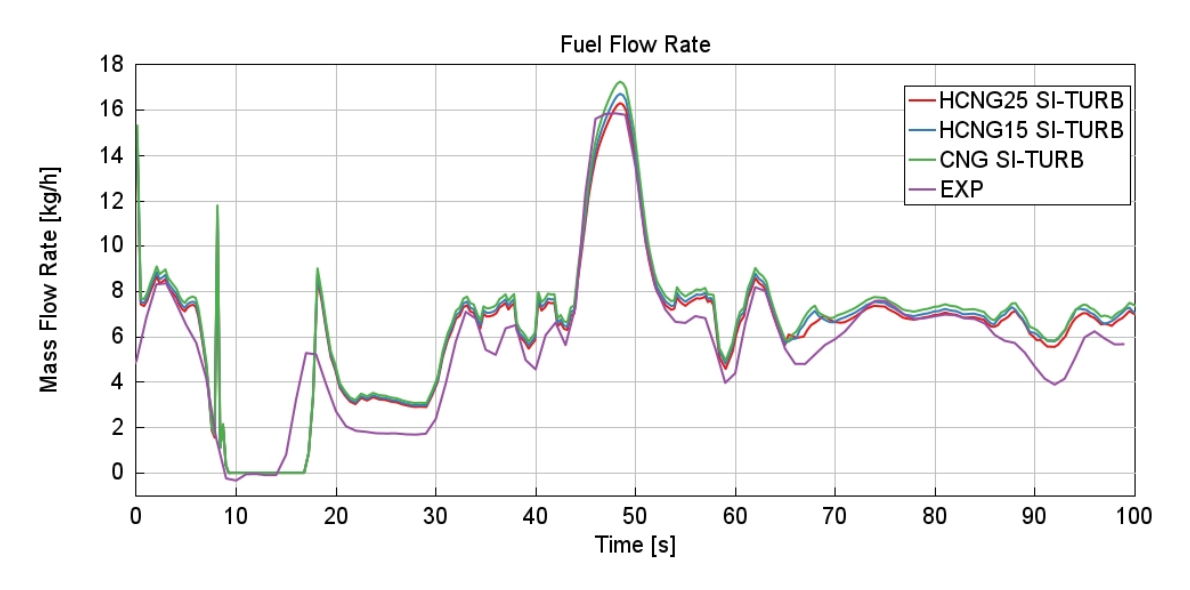


Figure 3.7: WHTC fuel flow rate profiles - Single operating point combustion model (C2)

Analysing Figure 3.7, it emerges that the simulations reproduce the general trend of the experimental trace, capturing the main peaks and transition phases. However, the predicted fuel flow rate is systematically overestimated, particularly during acceleration phases, where the simulated peaks are higher and remain elevated for longer. In the more stable phases, after about 70 seconds, the discrepancy is less pronounced, leading to a

closer reproduction of the experimental profile. Despite these differences, the simulated curves obtained with the different fuels are very similar to each other.

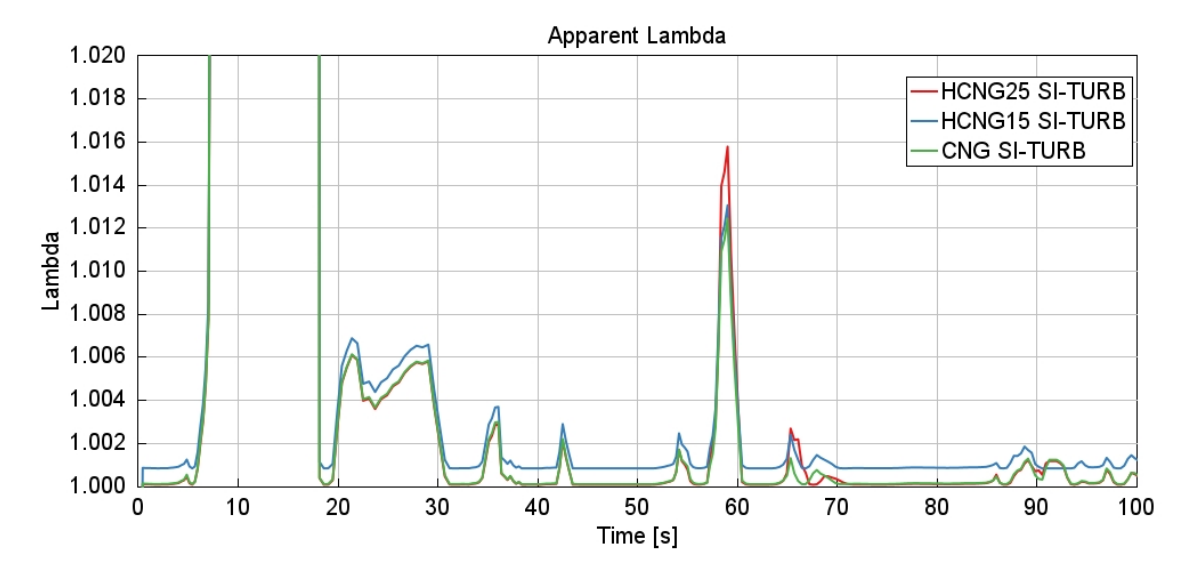


Figure 3.8: WHTC Lambda profiles - Single operating point combustion model (C2)

Observing the  $\lambda$  profiles Graph 3.8, it is evident that stoichiometric combustion conditions are maintained throughout the simulation. Two exceptions can be noted: first, a transient lean peak occurs around 60 seconds, but since it appears only once within a limited interval, it does not affect the overall stoichiometric behaviour. Second, during the cut-off phase, as expected, combustion ceases and  $\lambda$  tends toward infinity due to the presence of air only. Overall, stoichiometric conditions can be considered verified for the analysed portion of the cycle. The results obtained are acceptable, but can be further improved by adopting the alternative approach, specifically using a Look-Up Table that incorporates burn rates for additional operating points as the combustion object.

### 3.2.2 Look-Up Table (LUT) combustion modelling approach

These analyses are carried out using a Look-Up Table (LUT) as the combustion object, which incorporates the burn rates of four engine operating points. Two approaches are considered:

- The burn rates are derived from the Three Pressure Analysis performed with methane,
- The burn rates are obtained from the predictive SI-TURB analysis performed with methane.

### **Look-Up Table with TPA analysis burn rates**

The figure below shows the brake torque, fuel flow rate, and  $\lambda$  profile resulting from this analysis.

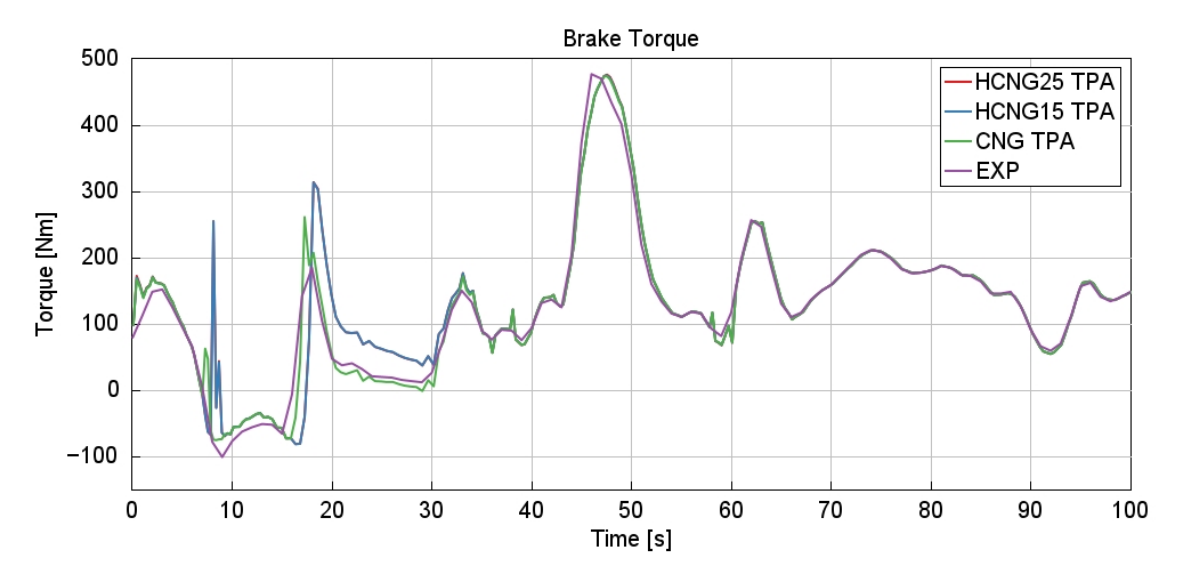


Figure 3.9: WHTC brake torque profiles - LUT with TPA combustion model

Looking at Figure 3.9, it is evident that the simulated brake torque profiles are significantly improved and better replicate the experimental ones compared to the previous analysis using only the C2 burn rate. Despite some discrepancies, with slight overestimation, during the first thirty seconds, the simulated profiles match the required torque very well for the remainder of the cycle. Moreover, the largest peaks in the middle of the cycle are accurately reproduced for all fuels.

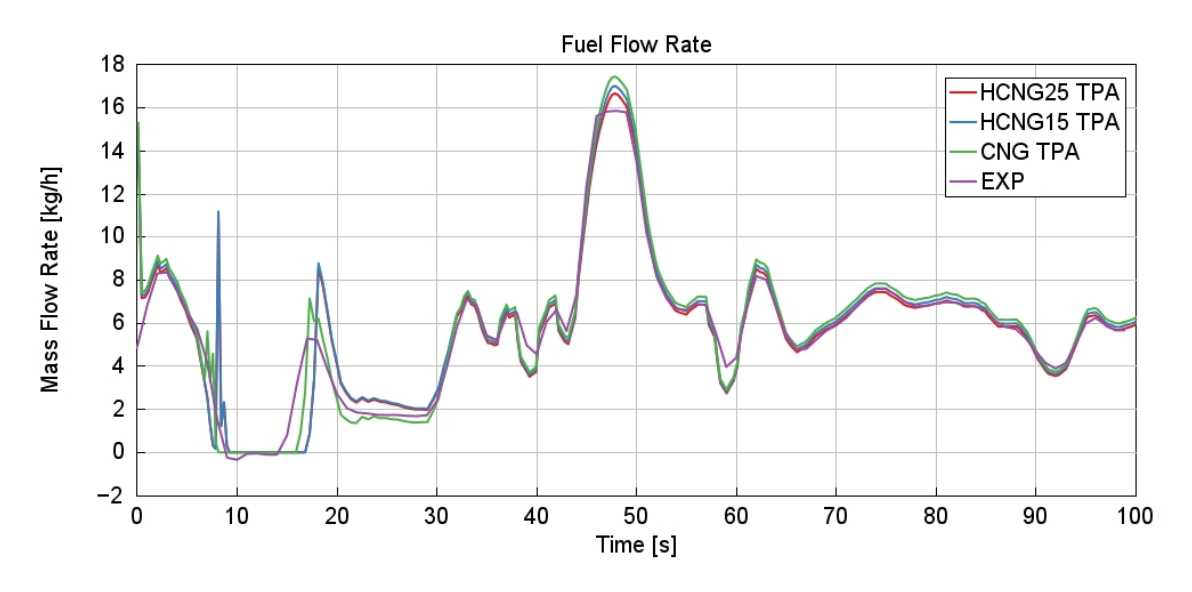


Figure 3.10: WHTC fuel flow rate profiles - LUT with TPA combustion model

The graphs in Figure 3.10 depict the positive effect of using LUTs derived from TPA burn rate profiles, which improve the agreement between simulation and experiment. Although the first transient phase presents some unrealistic peaks, the overall profiles appear smoother and more coherent with the experimental behaviour. From 30 seconds in poi, the correspondence becomes very close, with simulated values almost overlapping the experimental curve.

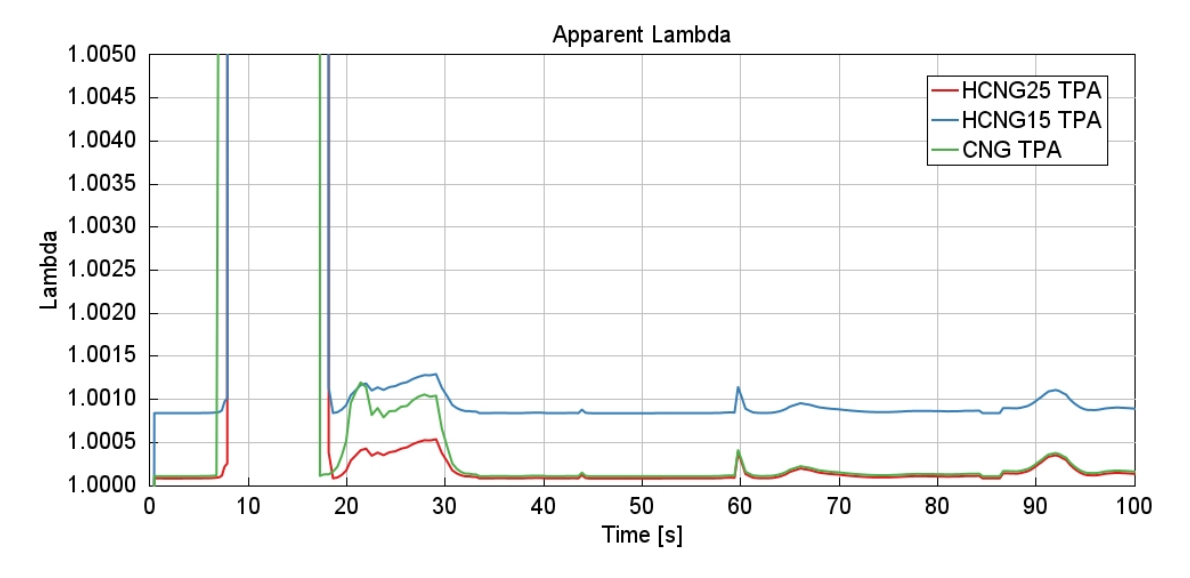


Figure 3.11: WHTC lambda profiles - LUT with TPA combustion model

The Graph 3.11 shows the lambda profiles obtained with this analysis. A clear improvement can be observed in maintaining stoichiometric conditions throughout the cycle. The three fuels exhibit very low fluctuations, indicating that the combustion process is stable and well controlled across the entire operating range.

### Look-Up Table with SI-TURB analysis burn rates

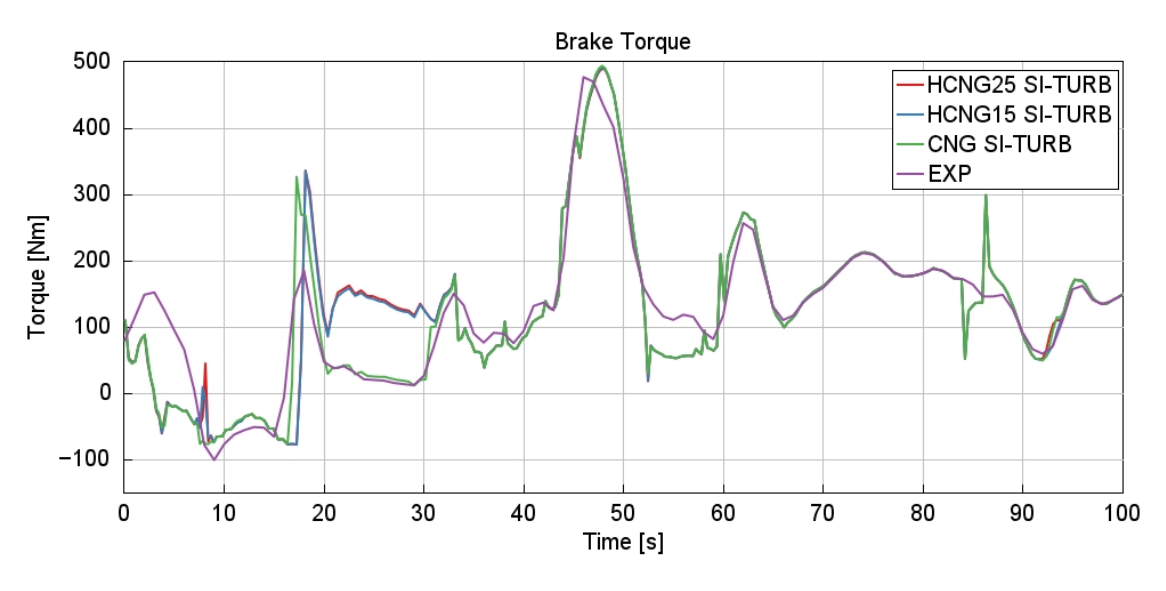


Figure 3.12: WHTC brake torque profiles - LUT with SI-TURB combustion model

Figure 3.12 shows the brake torque profiles obtained using the burn rates from the SI-TURB analysis. During the first forty seconds, significant discrepancies are observed, with peaks higher than the experimental values and a general understimation of the torque. After this initial phase, the simulated profiles improve their agreement with the experimental curve. However, they still present more discrepancies and fluctuations compared

to the results obtained using the TPA burn rates.

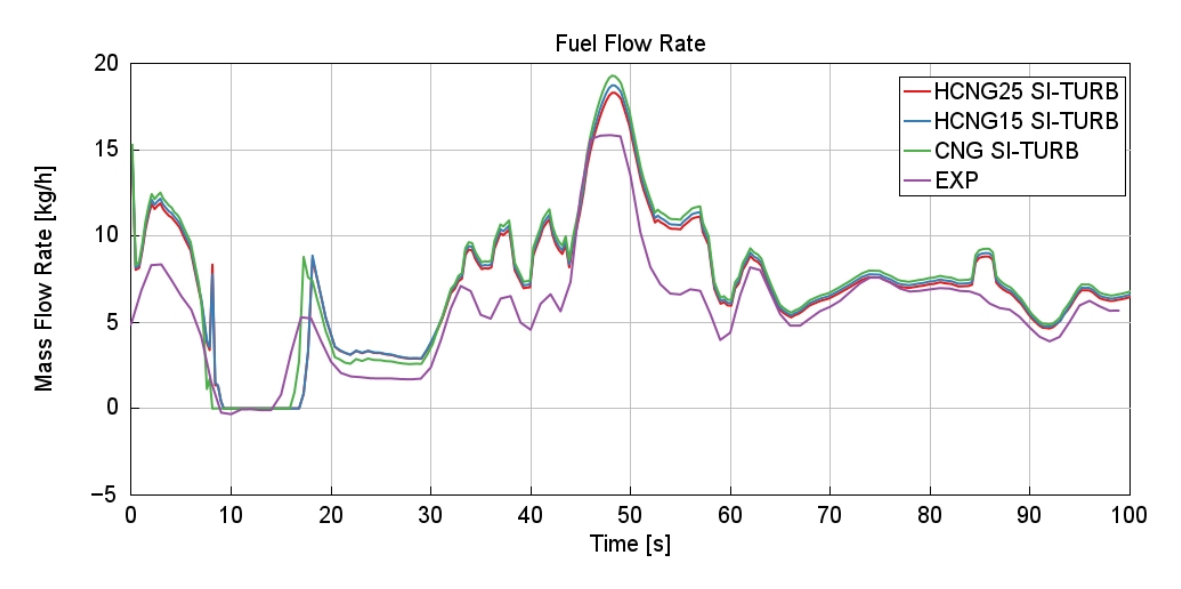


Figure 3.13: WHTC fuel flow rate profiles - LUT with SI-TURB combustion model

From the profiles shown in Figure 3.13, it can be seen that the simulated curves follow the shape and oscillations of the experimental trace. However, the predicted fuel flow rate remains consistently higher for the entire cycle. The discrepancy is particularly evident around the 50-second peak, where all fuels, despite showing similar behaviour, present a clear overestimation of the flow rate. This systematic deviation highlights the limitations of the SI-TURB approach in achieving quantitative accuracy, despite correctly capturing the qualitative trend.

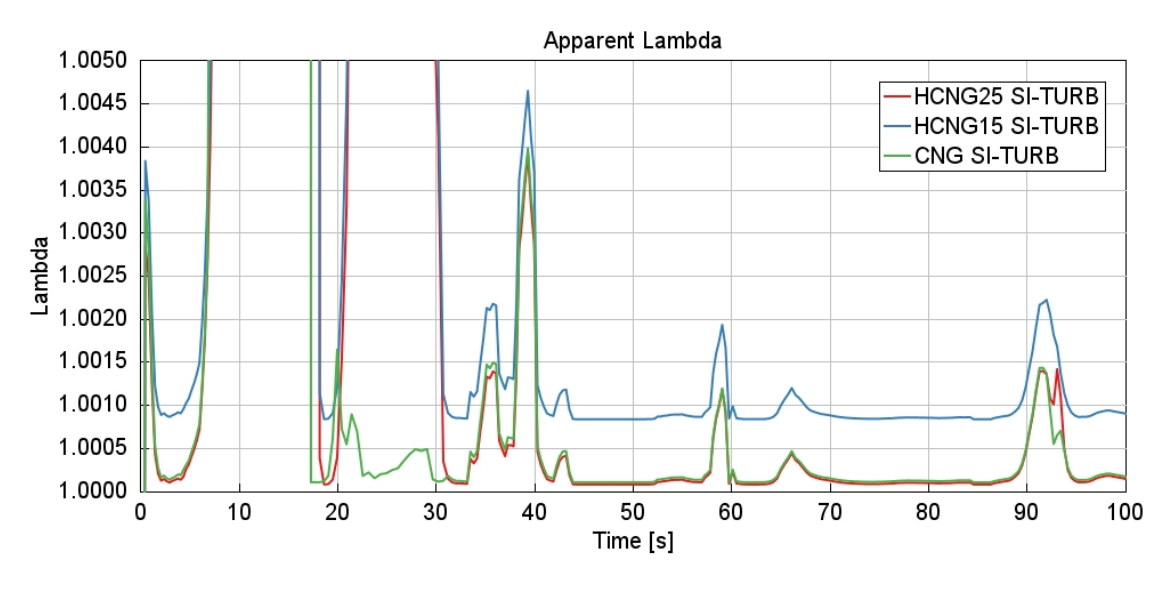


Figure 3.14: WHTC lambda profiles - LUT with SI-TURB combustion model

The  $\lambda$  profiles shown in Figure 3.14 exhibit greater fluctuations compared to the TPA analysis, although stoichiometric conditions are maintained under all operating points.

In general, the analyses performed using a Look-Up Table as a combustion object show improved accuracy in reproducing the WHTC cycle compared to the single C2 case. Moreover, the results obtained with burn rates derived from the TPA analysis provide a better match with the experimental data than those obtained with the SI-TURB burn rates. This behaviour can be explained by the different implementations of the two approaches. With the TPA Look-Up Table, the burn rate profiles are directly inserted into the cylinder combustion model. In contrast, the SI-TURB approach relies on multipliers obtained from the previous analysis, which are applied to each engine operating point, while the actual burn rate profiles are generated by the software. By leaving the interpolation process to the software and providing more accurate profiles through the TPA, the resulting simulations achieve higher accuracy and precision.

# **Chapter 4**

## **Conclusions**

This thesis focused on the development and calibration of a 0D-1D digital model of a heavy-duty engine fuelled with methane-hydrogen blends, adopting GT-SUITE as the simulation environment. The objectives were dual. The first was to analyse the engine behaviour under both steady-state and transient conditions. The second was to assess the impact of hydrogen additions as a transition strategy towards cleaned fuels, with particular attention to combustion stability and efficiency.

The first step involved calibrating the model. To reduce computation effort without losing fundamental information on the combustion and thermodynamic cycle, the six-cylinder model was simplified into an equivalent mono-cylinder configuration. The first calibration was carried out using the Wiebe function as a combustion object, which provided acceptable results but still showed discrepancies in the in-cylinder pressure traces. A significant improvement was obtained with the Three Pressure Analysis (TPA), which enabled the reconstruction of burn rate profiles from experimental pressure data. By adopting this technique, the combustion process calibration improves, and the simulated pressure traces match the experimental ones with high accuracy. Consequently, the burn rates derived from this analysis were used as a reference for all the subsequent simulations. The predictive SI-TURB model, although trickier to calibrate, demonstrated good capability in reproducing the real engine behaviour. However, the global optimisation to apply a single set of parameters to describe the combustion process produced unsatisfactory results. Reliable and consistent burn rate profiles and in-cylinder pressure traces were obtained only when calibration was performed individually for each engine operating point. This outcome highlights a limitation of the present work, since achieving a robust and generalisable calibration would require a broader experimental dataset to cover a wider range of operating conditions.

The introduction of hydrogen provided clear benefits in terms of CO and  $CO_2$  reduction, but it also led to higher NO and  $NO_x$  formation as well as increased knock tendency. The

simulations carried out with the Wiebe function as a combustion object were declared for the methane-hydrogen cases, since this approach was not capable of accurately reproducing the combustion process. Similarly, the results obtained with the individual SI-TURB optimisation, calibrated only on methane, showed clear limitations, with advanced and phase-shifted burn rate peaks. This outcome underlines the challenges in developing a predictive model capable of accurately reproducing combustion behaviour when key parameters, such as the injected fuel mixture, are modified. Conversely, better results were achieved for HCNG mixtures by adopting the burn rates derived from the TPA analysis, as these are directly based on real in-cylinder pressure data.

The knock analysis confirmed that, under reference conditions, the engine operated safely without any signs of knock. Increasing the compression ratio up to 11.5 improves the engine efficiency without promoting abnormal combustion phenomena. On the contrary, advancing the spark timing and increasing the intake pressure both showed a correlation with higher knock tendency, especially in the presence of hydrogen blends. The combined variation of these parameters highlighted how delicate and challenging the trade-off is between performance optimisation and combustion stability.

The transient validation on the WHTC demonstrated that the model can also be applied under dynamic conditions. The approach based on the imposition of a Look-Up Table containing different burn rate profiles for the various operating points, instead of relying on a single representative point for the entire cycle, showed clear improvements and provided a more coherent and stable response. The burn rates derived from the TPA proved to be superior to those obtained with SI-TURB, confirming that the accuracy of the combustion profile is crucial for reliable transient simulations.

In conclusion, the objectives of this thesis have been achieved. Methane-hydrogen blends represent a promising transitional pathway towards decarbonised transportation, but require accurate calibration to mitigate knock and pollutant formation while maximising their potential benefits. The developed model is consistent and flexible, providing a solid foundation for future studies on alternative fuels and advanced engine control strategies.

# **Bibliography**

- [1] K. Calvin et al., "IPCC, 2023: Climate Change 2023: Synthesis Report. Contribution of Working Groups I, II and III to the Sixth Assessment Report of the Intergovernmental Panel on Climate Change [Core Writing Team, H. Lee and J. Romero (eds.)]. IPCC, Geneva, Switzerland.," en, Intergovernmental Panel on Climate Change, Tech. Rep., Jul. 2023. DOI: 10.59327/ipcc/ar6-9789291691647. Accessed: Jul. 8, 2025. [Online]. Available: https://www.ipcc.ch/report/ar6/syr/.
- [2] P. Friedlingstein et al., "Global Carbon Budget 2024," English, Earth System Science Data, vol. 17, no. 3, pp. 965–1039, Mar. 2025, Publisher: Copernicus GmbH, ISSN: 1866-3508. DOI: 10.5194/essd-17-965-2025. Accessed: Jul. 10, 2025. [Online]. Available: https://essd.copernicus.org/articles/17/965/2025/.
- [3] European Parliament, *Greenhouse gas emissions by country and sector (infographic)*, Infographic, European Parliament News, Accessed: 2025-07-16, Dec. 2024. [Online]. Available: https://www.europarl.europa.eu/topics/en/article/20180301ST098928/greenhouse-gas-emissions-by-country-and-sector-infographic.
- [4] The Paris Agreement | UNFCCC. Accessed: Jul. 11, 2025. [Online]. Available: https://unfccc.int/process-and-meetings/the-paris-agreement.
- [5] European Commission, Delivering on our targets: The european green deal brochure, PDF brochure, Commission Press Corner, Accessed: 2025-07-16, 2021. [Online]. Available: https://ec.europa.eu/commission/presscorner/api/files/attachment/869807/EGD\_brochure\_EN.pdf.
- [6] Air pollution in Europe 2025 reporting status under the National Emission reduction Commitments Directive | European Environment Agency's home page. Accessed: Jul. 11, 2025. [Online]. Available: https://www.eea.europa.eu/en/analysis/publications/air-pollution-in-europe-2025-reporting-status-under-the-national-emission-reduction-commitments-directive?utm\_source=chatgpt.com.

- [7] I. E. Agency, "World Energy Outlook 2022," en, International Energy Agency, Paris, France, Tech. Rep., 2022. [Online]. Available: https://www.iea.org/reports/world-energy-outlook-2022.
- [8] European Commission, *Hydrogen factsheet*, Accessed: 2025-07-16, Jul. 2021. [Online]. Available: https://ec.europa.eu/commission/presscorner/detail/en/fs\_21\_3676.
- [9] J. Dornoff and F. Rodríguez, "Euro 7: The new emission standard for light- and heavy-duty vehicles in the European Union," en,
- [10] M. I. Khan, T. Yasmin, and A. Shakoor, "Technical overview of compressed natural gas (CNG) as a transportation fuel," en, *Renewable and Sustainable Energy Reviews*, vol. 51, pp. 785–797, Nov. 2015, Publisher: Elsevier BV, ISSN: 1364-0321. DOI: 10.1016/j.rser.2015.06.053. Accessed: Jul. 15, 2025. [Online]. Available: https://linkinghub.elsevier.com/retrieve/pii/S1364032115006255.
- [11] Y. H. Teoh et al., "A review on production and implementation of hydrogen as a green fuel in internal combustion engines," en, *Fuel*, vol. 333, p. 126525, Feb. 2023, Publisher: Elsevier BV, ISSN: 0016-2361. DOI: 10.1016/j.fuel.2022. 126525. Accessed: Jul. 15, 2025. [Online]. Available: https://linkinghub.elsevier.com/retrieve/pii/S001623612203349X.
- [12] A. D. Prithu, K. M. Rahman, M. Islam, D. H. Saharaj, and M. S. Hossain, "Effects of hydrogen enrichment in Methane/Air combustion with different inlet arrangements: A numerical approach," en, *International Journal of Thermofluids*, vol. 26, p. 101 112, Mar. 2025, ISSN: 26662027. DOI: 10.1016/j.ijft.2025.101112. Accessed: Jun. 9, 2025. [Online]. Available: https://linkinghub.elsevier.com/retrieve/pii/S2666202725000606.
- [13] R. Michikawauchi, S. Tanno, Y. Ito, M. Kanda, and M. Kawauchi, "Combustion Improvement of CNG Engines by Hydrogen Addition," en, Aug. 2011, pp. 2011–01–1996. DOI: 10.4271/2011-01-1996. Accessed: Jun. 9, 2025. [Online]. Available: https://www.sae.org/content/2011-01-1996/.
- [14] N. I. Gurakov et al., "Stability Limits of the Methane–Hydrogen Mixture Combustion," en, *Bulletin of the Lebedev Physics Institute*, vol. 50, no. 4, pp. 150–157, Apr. 2023, ISSN: 1068-3356, 1934-838X. DOI: 10.3103/S1068335623040061. Accessed: Jun. 9, 2025. [Online]. Available: https://link.springer.com/10.3103/S1068335623040061.
- [15] GT-SUITE, en. Accessed: Jul. 16, 2025. [Online]. Available: https://www.gtisoft.com/gt-suite/.
- [16] Gamma Technologies, *Gt-suite*, *engine performance application manual*, Gamma Technologies, 2016.

- [17] K. Haghighi and G. P. McTaggart-Cowan, "Modelling the Impacts of Hydrogen–Methane Blend Fuels on a Stationary Power Generation Engine," en, *Energies*, vol. 16, no. 5, p. 2420, Mar. 2023, ISSN: 1996-1073. DOI: 10.3390/en16052420. Accessed: Aug. 26, 2025. [Online]. Available: https://www.mdpi.com/1996-1073/16/5/2420.
- [18] D. Minic, Ed., *Hydrogen Energy Challenges and Perspectives*, en. InTech, Oct. 2012, ISBN: 978-953-51-0812-2. DOI: 10.5772/2824. Accessed: Aug. 26, 2025. [Online]. Available: http://www.intechopen.com/books/hydrogen-energy-challenges-and-perspectives.
- [19] S. Bougrine, S. Richard, A. Nicolle, and D. Veynante, "Numerical study of laminar flame properties of diluted methane-hydrogen-air flames at high pressure and temperature using detailed chemistry," en, *International Journal of Hydrogen Energy*, vol. 36, no. 18, pp. 12 035–12 047, Sep. 2011, Publisher: Elsevier BV, ISSN: 0360-3199. DOI: 10.1016/j.ijhydene.2011.06.053. Accessed: Jul. 15, 2025. [Online]. Available: https://linkinghub.elsevier.com/retrieve/pii/S0360319911015254.
- [20] Emission Test Cycles: World Harmonized Transient Cycle (WHTC). Accessed: Sep. 13, 2025. [Online]. Available: https://dieselnet.com/standards/cycles/whtc.php.

# Appendix A

## **Knock analysis**

This appendix presents the results of the knock analysis for the 1400 rpm  $\times$  750 Nm operating point (full load, C5), as well as those obtained using the Kinetic-Fit-Hydrogen knock model. Specifically:

- Section A.1 refers to the Compression Ratio sweep,
- Section A.2 refers to the Spark Advance sweep,
- Section A.3 refers to the Intake Pressure sweep,
- Section A.4 refers to the combined Spark Advance and Intake Pressure sweep case.

	CNO	G	HCNO	G15	HCNO	G25
CR	Crank Angle at Knock Onset [deg]	Knock Probability	Crank Angle at Knock Onset [deg]	Knock Probability	Crank Angle at Knock Onset [deg]	Knock Probability
10.3	_	0	-	0	-	0
10.4	_	0	-	0	-	0
10.5	_	0	-	0	-	0
10.6	-	0	-	0	-	0
10.7	_	0	-	0	_	0
10.8	_	0	-	0	_	0
10.9	_	0	-	0	-	0
11.0	_	0	-	0	_	0
11.1	_	0	-	0	_	0
11.2	_	0	-	0	-	0
11.3	_	0	-	0	-	0
11.4	_	0	-	0	-	0
11.5	_	0	-	0	-	0

Table A.1.1: Crank Angle at Knock Onset and Knock Probability - KNG knock model - CR sweep (C5)

CR	CNG	HCNG15	HCNG25
	Brake Efficiency [%]	Brake Efficiency [%]	Brake Efficiency [%]
10.3	33.733	34.432	35.069
10.4	33.804	34.494	35.101
10.5	33.871	34.546	35.193
10.6	33.942	34.595	35.227
10.7	34.010	34.689	35.315
10.8	34.075	34.711	35.343
10.9	34.140	34.797	35.435
11.0	34.206	34.813	35.458
11.1	34.262	34.889	35.544
11.2	34.333	34.929	35.564
11.3	34.393	34.952	35.642
11.4	34.451	35.057	35.661
11.5	34.510	35.038	35.748

Table A.1.2: Brake Efficiency - KNG knock model - CR sweep (C5)

	CNC	G	HCNO	G15	HCNO	G25
SA [deg]	Crank Angle at Knock Onset [deg]	Knock Probability	Crank Angle at Knock Onset [deg]	Knock Probability	Crank Angle at Knock Onset [deg]	Knock Probability
Ref	-	0	_	0	_	0
-4	-	0	-	0	-	0
-8	-	0	-	0	-	0
-12	-	0	-	0	-	0
-16	-	0	16.44	1	13.10	1
-20	8.45	1	6.58	1	5.47	1
-24	2.64	1	1.35	1	0.60	1
-28	-1.44	1	-2.44	1	-3.14	1
-32	-4.73	1	-5.68	1	-6.21	1
-36	-7.48	1	-8.39	1	-8.99	1
-40	-9.83	1	-10.78	1	-11.31	1
-44	-11.85	1	-12.83	1	-13.35	1
-48	-13.58	1	-14.54	1	-15.13	1

Table A.2.1: Crank Angle at Knock Onset and Knock Probability - KNG knock model - SA sweep (C3)

	HCNG15		HCNG25	
SA [deg]	Crank Angle at Knock Onset [deg]	Knock Probability	Crank Angle at Knock Onset [deg]	Knock Probability
Ref	-	0	-	0
-4	_	0	_	0
-8	-	0	-	0
-12	-	0	-	0
-16	14.42	1	15.10	1
-20	5.45	1	5.72	1
-24	0.38	1	0.59	1
-28	-3.36	1	-3.25	1
-32	-6.58	1	-6.36	1
-36	-9.29	1	-9.18	1
-40	-11.70	1	-11.52	1
-44	-13.78	1	-13.57	1
-48	-15.52	1	-15.36	1

Table A.2.2: Crank Angle at Knock Onset and Knock Probability - KH knock model - SA sweep (C3)

SA [deg]	CNG	HCNG15	HCNG25
	Brake Efficiency [%]	Brake Efficiency [%]	Brake Efficiency [%]
Ref	33.733	34.432	35.069
-4	34.042	34.674	35.327
-8	33.947	34.487	35.141
-12	33.425	33.750	34.473
-16	32.492	32.665	33.324
-20	31.173	31.169	31.862
-24	29.522	29.250	29.965
-28	27.598	27.202	27.851
-32	25.456	24.868	25.625
-36	23.179	22.480	23.136
-40	20.825	19.983	20.698
-44	18.412	17.498	18.227
-48	15.995	15.072	15.748

Table A.2.3: Brake Efficiency - KNG knock model - SA sweep (C3)

		CNG			HCNG15			HCNG25	
	Pint [bar]	Crank Angle at Knock Onset [deg]	Knock Probability	Pint [bar]	Crank Angle at Knock Onset [deg]	Knock Probability	Pint [bar]	Crank Angle at Knock Onset [deg]	Knock Probability
Ref	1.72	-	0	1.70	-	0	1.68	-	0
+10%	1.89	-	0	1.87	-	0	1.85	-	0
+20%	2.07	-	0	2.04	-	0	2.02	-	0
+30%	2.24	-	0	2.21	-	0	2.18	-	0
+40%	2.41	-	0	2.38	-	0	2.35	-	0
+50%	2.58	-	0	2.55	-	0	2.52	-	0
+60%	2.76	-	0	2.71	-	0	2.69	-	0
+70%	2.93	-	0	2.88	-	0	2.86	-	0
+80%	3.10	-	0	3.05	-	0	3.02	-	0
+90%	3.27	-	0	3.22	-	0	3.19	-	0
+100%	3.45	-	0	3.39	-	0	3.36	-	0
+110%	3.62	-	0	3.56	-	0	3.53	-	0
+120%	3.79	-	0	3.73	-	0	3.69	-	0
+130%	3.96	-	0	3.90	-	0	3.86	-	0
+140%	4.13	_	0	4.07	_	0	4.03	_	0
+150%	4.31	-	0	4.24	-	0	4.20	-	0

Table A.3.1: Crank Angle at Knock Onset and Knock Probability - KNG knock model - Intake Pressure sweep (C5)

		HCNG15			HCNG25	
	Pint [bar]	Crank Angle at Knock Onset [deg]	Knock Probability	Pint [bar]	Crank Angle at Knock Onset [deg]	Knock Probability
Ref	1.70	-	0	1.68	_	0
+10%	1.87	_	0	1.85	_	0
+20%	2.04	_	0	2.02	_	0
+30%	2.21	_	0	2.18	_	0
+40%	2.38	_	0	2.35	_	0
+50%	2.55	-	0	2.52	_	0
+60%	2.71	_	0	2.69	_	0
+70%	2.88	_	0	2.86	_	0
+80%	3.05	_	0	3.02	_	0
+90%	3.22	_	0	3.19	_	0
+100%	3.39	_	0	3.36	_	0
+110%	3.56	-	0	3.53	_	0
+120%	3.73	-	0	3.69	-	0
+130%	3.90	_	0	3.86	_	0
+140%	4.07	_	0	4.03	_	0
+150%	4.24	-	0	4.20	_	0

Table A.3.2: Crank Angle at Knock Onset and Knock Probability - KH knock model - Intake Pressure sweep (C5)

		CNG		HCNG15		HCNG25
	Pint [bar]	Brake Efficiency [%]	Pint [bar]	Brake Efficiency [%]	Pint [bar]	Brake Efficiency [%]
Ref	1.72	33.733	1.70	34.432	1.68	35.069
+10%	1.89	34.433	1.87	35.773	1.85	36.343
+20%	2.07	35.023	2.04	36.789	2.02	37.370
+30%	2.24	35.525	2.21	37.692	2.18	38.286
+40%	2.41	35.949	2.38	38.521	2.35	39.111
+50%	2.58	36.327	2.55	39.278	2.52	39.870
+60%	2.76	36.673	2.71	39.974	2.69	40.563
+70%	2.93	36.972	2.88	40.628	2.86	41.210
+80%	3.10	37.249	3.05	41.230	3.02	41.815
+90%	3.27	37.497	3.22	41.798	3.19	42.384
+100%	3.45	37.720	3.39	42.335	3.36	42.920
+110%	3.62	37.929	3.56	42.843	3.53	43.427
+120%	3.79	38.122	3.73	43.325	3.69	43.910
+130%	3.96	38.312	3.90	43.784	3.86	44.370
+140%	4.13	38.448	4.07	44.225	4.03	44.812
+150%	4.31	38.625	4.24	44.646	4.20	45.233

Table A.3.3: Brake Efficiency - KNG knock model - Intake Pressure sweep (C5)

		CNG			HCNG15			HCNG25	
	Pint [bar]	Crank Angle at Knock Onset [deg]	Knock Probability	Pint [bar]	Crank Angle at Knock Onset [deg]	Knock Probability	Pint [bar]	Crank Angle at Knock Onset [deg]	Knock Probability
Ref	1.33	-	0	1.37	-	0	1.40	-	0
+10%	1.47	_	0	1.51	_	0	1.54	_	0
+20%	1.60	-	0	1.65	-	0	1.68	-	0
+30%	1.73	-	0	1.79	-	0	1.82	-	0
+40%	1.87	-	0	1.92	_	0	1.96	21.15	1
+50%	2.00	-	0	2.06	19.54	1	2.10	16.12	1
+60%	2.13	-	0	2.20	15.77	1	2.24	13.67	1
+70%	2.27	-	0	2.33	13.65	1	2.38	12.06	1
+80%	2.40	-	0	2.47	12.19	1	2.52	10.86	1
+90%	2.53	_	0	2.61	11.04	1	2.66	9.92	1
+100%	2.67	-	0	2.75	10.12	1	2.80	9.13	1
+110%	2.80	-	0	2.88	9.41	1	2.94	8.47	1
+120%	2.93	_	0	3.02	8.77	1	3.08	7.96	1
+130%	3.07	-	0	3.16	8.36	1	3.22	7.58	1
+140%	3.20	-	0	3.30	8.02	1	3.36	7.59	1
+150%	3.33	_	0	3.43	8.27	1	3.50	7.93	1

Table A.3.4: Crank Angle at Knock Onset and Knock Probability - KNG knock model - Intake Pressure sweep with CR=11.5 (C3)

		HCNG15		HCNG25				
	Pint [bar]	Crank Angle at Knock Onset [deg]	Knock Probability	Pint [bar]	Crank Angle at Knock Onset [deg]	Knock Probability		
Ref	1.37	_	0	1.40	-	0		
+10%	1.51	_	0	1.54	-	0		
+20%	1.65	-	0	1.68	-	0		
+30%	1.79	24.21	1	1.82	20.81	1		
+40%	1.92	16.18	1	1.96	15.42	1		
+50%	2.06	13.47	1	2.10	13.04	1		
+60%	2.20	11.82	1	2.24	11.50	1		
+70%	2.33	10.63	1	2.38	10.39	1		
+80%	2.47	9.71	1	2.52	9.52	1		
+90%	2.61	8.94	1	2.66	8.83	1		
+100%	2.75	8.31	1	2.80	8.22	1		
+110%	2.88	7.81	1	2.94	7.71	1		
+120%	3.02	7.34	1	3.08	7.34	1		
+130%	3.16	7.07	1	3.22	7.08	1		
+140%	3.30	6.86	1	3.36	7.19	1		
+150%	3.43	7.19	1	3.50	7.66	1		

Table A.3.5: Crank Angle at Knock Onset and Knock Probability - KH knock model - Intake Pressure sweep with CR=11.5 (C3)

		CNG		HCNG15		HCNG25
	Pint [bar]	Brake Efficiency [%]	Pint [bar]	Brake Efficiency [%]	Pint [bar]	Brake Efficiency [%]
Ref	1.33	32.216	1.37	33.444	1.40	33.589
+10%	1.47	33.140	1.51	34.898	1.54	35.002
+20%	1.60	33.922	1.65	35.938	1.68	36.051
+30%	1.73	34.570	1.79	36.872	1.82	36.993
+40%	1.87	35.145	1.92	37.708	1.96	37.837
+50%	2.00	35.630	2.06	38.480	2.10	38.596
+60%	2.13	36.067	2.20	39.186	2.24	39.305
+70%	2.27	36.454	2.33	39.842	2.38	39.961
+80%	2.40	36.798	2.47	40.456	2.52	40.574
+90%	2.53	37.102	2.61	41.027	2.66	41.149
+100%	2.67	37.384	2.75	41.568	2.80	41.691
+110%	2.80	37.654	2.88	42.075	2.94	42.204
+120%	2.93	37.911	3.02	42.558	3.08	42.687
+130%	3.07	38.142	3.16	43.016	3.22	43.147
+140%	3.20	38.356	3.30	43.455	3.36	43.586
+150%	3.33	38.554	3.43	43.873	3.50	44.005

Table A.3.6: Brake Efficiency - KNG knock model - Intake Pressure sweep with CR=11.5 (C3)

		CNG			HCNG15			HCNG25	
	Pint [bar]	Crank Angle at Knock Onset [deg]	Knock Probability	Pint [bar]	Crank Angle at Knock Onset [deg]	Knock Probability	Pint [bar]	Crank Angle at Knock Onset [deg]	Knock Probability
Ref	1.72	_	0	1.70	-	0	1.68	_	0
+10%	1.89	-	0	1.87	-	0	1.85	_	0
+20%	2.07	_	0	2.04	-	0	2.02	_	0
+30%	2.24	-	0	2.21	-	0	2.18	-	0
+40%	2.41	-	0	2.38	-	0	2.35	-	0
+50%	2.58	-	0	2.55	-	0	2.52	-	0
+60%	2.76	-	0	2.71	-	0	2.69	-	0
+70%	2.93	-	0	2.88	-	0	2.86	-	0
+80%	3.10	-	0	3.05	-	0	3.02	-	0
+90%	3.27	-	0	3.22	-	0	3.19	-	0
+100%	3.45	-	0	3.39	-	0	3.36	-	0
+110%	3.62	-	0	3.56	-	0	3.53	-	0
+120%	3.79	-	0	3.73	-	0	3.69	-	0
+130%	3.96	_	0	3.90	-	0	3.86	_	0
+140%	4.13	-	0	4.07	-	0	4.03	_	0
+150%	4.31	-	0	4.24	-	0	4.20	-	0

Table A.3.7: Crank Angle at Knock Onset and Knock Probability - KNG knock model - Intake Pressure sweep with  $CR=11.5\ (C5)$ 

		HCNG15			HCNG25	
	Pint [bar]	Crank Angle at Knock Onset [deg]	Knock Probability	Pint [bar]	Crank Angle at Knock Onset [deg]	Knock Probability
Ref	1.70	-	0	1.68	_	0
+10%	1.87	_	0	1.85	_	0
+20%	2.04	_	0	2.02	_	0
+30%	2.21	_	0	2.18	_	0
+40%	2.38	_	0	2.35	_	0
+50%	2.55	_	0	2.52	_	0
+60%	2.71	_	0	2.69	_	0
+70%	2.88	_	0	2.86	_	0
+80%	3.05	_	0	3.02	_	0
+90%	3.22	_	0	3.19	_	0
+100%	3.39	_	0	3.36	_	0
+110%	3.56	_	0	3.53	-	0
+120%	3.73	_	0	3.69	_	0
+130%	3.90	_	0	3.86	-	0
+140%	4.07	_	0	4.03	_	0
+150%	4.24	_	0	4.20	_	0

Table A.3.8: Crank Angle at Knock Onset and Knock Probability - KH knock model - Intake Pressure sweep with CR=11.5 (C5)

		CNG		HCNG15		HCNG25
	Pint [bar]	Brake Efficiency [%]	Pint [bar]	Brake Efficiency [%]	Pint [bar]	Brake Efficiency [%]
Ref	1.72	34.510	1.70	35.038	1.68	35.748
+10%	1.89	35.216	1.87	36.496	1.85	37.090
+20%	2.07	35.818	2.04	37.532	2.02	38.124
+30%	2.24	36.335	2.21	38.451	2.18	39.042
+40%	2.41	36.762	2.38	39.283	2.35	39.872
+50%	2.58	37.167	2.55	40.041	2.52	40.635
+60%	2.76	37.517	2.71	40.747	2.69	41.330
+70%	2.93	37.826	2.88	41.395	2.86	41.977
+80%	3.10	38.107	3.05	41.999	3.02	42.583
+90%	3.27	38.361	3.22	42.569	3.19	43.149
+100%	3.45	38.596	3.39	43.101	3.36	43.686
+110%	3.62	38.816	3.56	43.610	3.53	44.192
+120%	3.79	39.009	3.73	44.088	3.69	44.672
+130%	3.96	39.180	3.90	44.544	3.86	45.128
+140%	4.13	39.386	4.07	44.982	4.03	45.566
+150%	4.31	39.517	4.24	45.399	4.20	45.983

Table A.3.9: Brake Efficiency - KNG knock model - Intake Pressure sweep with CR=11.5 (C5)

							SA	[deg]						
		-48	-44	-40	-36	-32	-28	-24	-20	-16	-12	-8	-4	Ref
	Ref	-6.39	-5.20	-3.70	-1.81	0.67	4.16	10.63	-	-	-	-	-	-
	+10%	-12.11	-10.86	-9.37	-7.58	-5.47	-2.93	0.17	4.23	10.90	-	_	-	-
	+20%	-15.53	-14.14	-12.51	-10.63	-8.50	-6.06	-3.24	0.11	4.35	10.75	-	-	ı
	+30%	-17.92	-16.39	-14.66	-12.70	-10.51	-8.05	-5.29	-2.12	1.63	6.46	14.40	-	_
	+40%	-19.70	-18.07	-16.24	-14.20	-11.95	-9.48	-6.73	-3.65	-0.11	4.20	10.09	25.31	-
	+50%	-21.12	-19.39	-17.47	-15.36	-13.06	-10.56	-7.82	-4.78	-1.35	2.69	7.86	16.19	_
핕	+60%	-22.24	-20.43	-18.44	-16.29	-13.95	-11.42	-8.68	-5.67	-2.30	1.59	6.37	13.18	-
[bar]	+70%	-23.17	-21.30	-19.26	-17.05	-14.68	-12.13	-9.38	-6.39	-3.07	0.71	5.28	11.36	23.43
Pint	+80%	-23.98	-22.04	-19.95	-17.70	-15.30	-12.73	-9.97	-6.98	-3.70	0.01	4.40	10.06	19.31
"	+90%	-24.64	-22.66	-20.54	-18.27	-15.84	-13.25	-10.49	-7.51	-4.25	-0.60	3.66	9.03	17.04
	+100%	-25.20	-23.19	-21.04	-18.74	-16.29	-13.69	-10.92	-7.95	-4.72	-1.12	3.05	8.20	15.50
	+110%	-25.70	-23.66	-21.46	-19.14	-16.67	-14.07	-11.30	-8.33	-5.11	-1.54	2.56	7.56	14.41
	+120%	-26.11	-24.04	-21.84	-19.49	-17.01	-14.39	-11.62	-8.65	-5.45	-1.91	2.13	7.01	13.55
	+130%	-26.43	-24.34	-22.10	-19.74	-17.25	-14.61	-11.84	-8.88	-5.68	-2.16	1.85	6.67	13.04
	+140%	-26.67	-24.54	-22.30	-19.94	-17.45	-14.81	-12.02	-9.05	-5.86	-2.34	1.64	6.44	12.79
	+150%	-26.80	-24.66	-22.40	-20.02	-17.50	-14.83	-12.01	-9.01	-5.78	-2.22	1.84	6.72	13.29

Table A.4.1: HCNG15 Crank Angle at Knock Onset and Knock Probability - KNG knock model - Intake Pressure and SA sweep with CR=11.5 (C3)

			SA [deg]											
		-48	-44	-40	-36	-32	-28	-24	-20	-16	-12	-8	-4	Ref
	Ref	-18.25	-16.53	-14.65	-12.46	-10.11	-7.42	-4.35	-0.88	3.44	9.20	_	_	_
	+10%	-18.68	-16.94	-14.98	-12.80	-10.33	-7.64	-4.58	-1.04	3.25	9.19	_	_	_
	+20%	-18.30	-16.57	-14.62	-12.45	-10.01	-7.25	-4.19	-0.59	3.84	10.36	_	_	_
	+30%	-17.75	-16.05	-14.10	-11.93	-9.47	-6.77	-3.65	-0.02	4.61	11.85	_	_	_
	+40%	-17.11	-15.43	-13.52	-11.33	-8.96	-6.25	-3.08	0.61	5.50	14.41	_	_	_
	+50%	-16.43	-14.77	-12.94	-10.82	-8.41	-5.69	-2.50	1.25	6.40	18.15	_	_	_
ī	+60%	-15.77	-14.15	-12.32	-10.24	-7.87	-5.16	-1.96	1.93	7.42	_	_	_	_
Pint [bar]	+70%	-15.09	-13.54	-11.72	-9.66	-7.32	-4.60	-1.40	2.62	8.58	-	_	_	_
int	+80%	-14.46	-12.93	-11.15	-9.12	-6.78	-4.06	-0.82	3.33	9.93	_	_	_	_
1	+90%	-13.84	-12.34	-10.59	-8.58	-6.26	-3.53	-0.23	4.09	11.64	_	_	_	_
	+100%	-13.26	-11.76	-10.04	-8.07	-5.76	-3.02	0.34	4.87	14.02	-	_	_	_
	+110%	-12.67	-11.22	-9.53	-7.56	-5.26	-2.50	0.93	5.71	19.00	-	_	_	_
	+120%	-12.12	-10.68	-9.02	-7.06	-4.76	-1.97	1.53	6.62	_	_	_	_	_
	+130%	-11.58	-10.17	-8.51	-6.57	-4.27	-1.47	2.15	7.64	_	_	_	_	_
	+140%	-11.07	-9.67	-8.03	-6.10	-3.78	-0.95	2.77	8.79	_	_	_	_	_
	+150%	-10.57	-9.17	-7.55	-5.63	-3.30	-0.43	3.42	10.23	_	_	_	_	_

Table A.4.2: HCNG25 Crank Angle at Knock Onset and Knock Probability - KNG knock model - Intake Pressure and SA sweep with  $CR=11.5\ (C5)$ 

							SA [de	g]						
		-48	-44	-40	-36	-32	-28	-24	-20	-16	-12	-8	-4	Ref
	Ref	-18.14	-16.49	-14.62	-12.50	-10.12	-7.41	-4.34	-0.73	3.65	10.06	_	_	_
	+10%	-18.65	-16.84	-15.01	-12.84	-10.33	-7.56	-4.49	-0.93	3.63	10.03	_	_	_
	+20%	-18.25	-16.57	-14.56	-12.42	-10.00	-7.24	-4.13	-0.42	4.24	11.47	_	_	_
	+30%	-17.65	-15.96	-14.06	-11.93	-9.52	-6.76	-3.60	0.19	4.97	13.10	_	_	_
	+40%	-17.06	-15.40	-13.51	-11.36	-8.99	-6.22	-3.03	0.77	5.83	16.00	_	_	_
	+50%	-16.37	-14.72	-12.90	-10.80	-8.40	-5.66	-2.44	1.47	6.84	28.55	_	_	_
-	+60%	-15.66	-14.07	-12.22	-10.13	-7.81	-5.03	-1.84	2.26	8.04	_	_	_	_
[ba	+70%	-14.93	-13.45	-11.59	-9.58	-7.22	-4.49	-1.20	3.00	9.51	-	_	_	_
Pint [bar]	+80%	-14.29	-12.78	-11.01	-8.99	-6.68	-3.92	-0.59	3.75	11.09	_	_	_	_
	+90%	-13.65	-12.17	-10.46	-8.44	-6.14	-3.38	0.01	4.55	13.60	_	_	_	_
	+100%	-13.07	-11.59	-9.90	-7.92	-5.60	-2.83	0.64	5.41	18.17	_	_	_	_
	+110%	-12.47	-11.03	-9.36	-7.39	-5.08	-2.28	1.26	6.38	_	_	_	_	_
	+120%	-11.91	-10.49	-8.83	-6.89	-4.55	-1.74	1.92	7.43	_	-	_	_	_
	+130%	-11.36	-9.96	-8.32	-6.38	-4.05	-1.19	2.56	8.66	_	_	_	_	_
	+140%	-10.84	-9.46	-7.82	-5.89	-3.56	-0.65	3.24	10.07	_	-	_	_	_
	+150%	-10.33	-8.95	-7.34	-5.40	-3.06	-0.11	3.95	11.98	ı	_	_	ı	ı

Table A.4.3: HCNG15 Crank Angle at Knock Onset and Knock Probability - KNG knock model - Intake Pressure and SA sweep with CR=11.5 (C5)

							SA	[deg]						
		-48	-44	-40	-36	-32	-28	-24	-20	-16	-12	-8	-4	Ref
	Ref	-13.06	-11.87	-10.42	-8.71	-6.67	-4.27	-1.38	2.29	7.63	-	-	-	-
	+10%	-16.78	-15.41	-13.81	-11.95	-9.86	-7.48	-4.76	-1.60	2.28	7.61	24.18	-	_
	+20%	-19.28	-17.73	-15.98	-14.01	-11.83	-9.41	-6.73	-3.68	-0.15	4.21	10.54	-	_
	+30%	-21.10	-19.43	-17.56	-15.50	-13.25	-10.78	-8.08	-5.07	-1.67	2.35	7.57	16.56	_
	+40%	-22.51	-20.72	-18.75	-16.61	-14.30	-11.81	-9.10	-6.12	-2.79	1.06	5.83	12.72	_
	+50%	-23.59	-21.73	-19.70	-17.50	-15.14	-12.60	-9.87	-6.90	-3.62	0.12	4.63	10.69	23.82
ㅁ	+60%	-24.49	-22.55	-20.46	-18.21	-15.82	-13.25	-10.51	-7.54	-4.29	-0.62	3.72	9.32	18.67
[pa	+70%	-25.22	-23.22	-21.08	-18.80	-16.38	-13.80	-11.03	-8.07	-4.83	-1.21	3.01	8.32	16.33
Pint [bar]	+80%	-25.84	-23.80	-21.62	-19.30	-16.84	-14.24	-11.48	-8.52	-5.30	-1.71	2.43	7.54	14.82
=	+90%	-26.39	-24.31	-22.10	-19.75	-17.28	-14.65	-11.87	-8.90	-5.69	-2.14	1.93	6.89	13.71
	+100%	-26.84	-24.73	-22.49	-20.12	-17.62	-15.00	-12.22	-9.25	-6.05	-2.53	1.49	6.35	12.86
	+110%	-27.21	-25.07	-22.80	-20.40	-17.89	-15.26	-12.48	-9.52	-6.33	-2.82	1.15	5.91	12.19
	+120%	-27.51	-25.37	-23.08	-20.67	-18.15	-15.49	-12.70	-9.74	-6.56	-3.07	0.88	5.60	11.74
	+130%	-27.71	-25.54	-23.23	-20.81	-18.27	-15.61	-12.82	-9.85	-6.66	-3.16	0.77	5.42	11.47
	+140%	-27.82	-25.62	-23.33	-20.91	-18.37	-15.69	-12.87	-9.88	-6.67	-3.15	0.85	5.60	11.87
	+150%	-27.77	-25.57	-23.23	-20.78	-18.20	-15.51	-12.66	-9.65	-6.41	-2.86	1.19	6.07	12.63

Table A.4.4: HCNG25 Crank Angle at Knock Onset and Knock Probability - KH knock model - Intake Pressure and SA sweep with CR=11.5 (C3)

							SA	[deg]						
		-48	-44	-40	-36	-32	-28	-24	-20	-16	-12	-8	-4	Ref
	Ref	-11.91	-10.77	-9.36	-7.68	-5.66	-3.24	-0.24	3.73	10.46	-	-	-	_
	+10%	-16.05	-14.70	-13.14	-11.32	-9.25	-6.88	-4.15	-0.94	3.06	8.87	-	-	_
	+20%	-18.73	-17.22	-15.49	-13.55	-11.40	-9.00	-6.32	-3.29	0.28	4.77	11.52	I	_
	+30%	-20.66	-19.02	-17.19	-15.15	-12.92	-10.47	-7.78	-4.78	-1.36	2.71	8.10	18.37	_
	+40%	-22.13	-20.38	-18.45	-16.34	-14.05	-11.56	-8.85	-5.87	-2.54	1.34	6.17	13.37	_
	+50%	-23.30	-21.46	-19.45	-17.27	-14.92	-12.40	-9.68	-6.71	-3.43	0.33	4.88	11.12	27.39
급	+60%	-24.22	-22.31	-20.24	-18.02	-15.63	-13.07	-10.34	-7.38	-4.12	-0.44	3.93	9.63	19.57
Pint [bar]	+70%	-25.00	-23.03	-20.91	-18.63	-16.22	-13.64	-10.89	-7.93	-4.69	-1.07	3.19	8.56	16.84
,iit	+80%	-25.67	-23.64	-21.47	-19.16	-16.71	-14.11	-11.35	-8.39	-5.17	-1.58	2.57	7.73	15.19
"	+90%	-26.21	-24.16	-21.96	-19.63	-17.15	-14.53	-11.76	-8.80	-5.59	-2.04	2.03	7.03	13.96
	+100%	-26.67	-24.58	-22.36	-20.01	-17.51	-14.89	-12.10	-9.15	-5.96	-2.43	1.59	6.45	13.01
	+110%	-27.08	-24.96	-22.71	-20.33	-17.82	-15.19	-12.40	-9.44	-6.25	-2.75	1.23	6.00	12.31
	+120%	-27.42	-25.27	-23.01	-20.61	-18.09	-15.45	-12.65	-9.69	-6.52	-3.03	0.91	5.60	11.73
	+130%	-27.66	-25.51	-23.21	-20.80	-18.27	-15.61	-12.82	-9.86	-6.68	-3.20	0.73	5.39	11.43
	+140%	-27.84	-25.64	-23.35	-20.94	-18.41	-15.75	-12.94	-9.97	-6.79	-3.31	0.60	5.26	11.33
	+150%	-27.90	-25.70	-23.39	-20.96	-18.41	-15.72	-12.88	-9.88	-6.66	-3.13	0.86	5.63	11.94

Table A.4.5: HCNG15 Crank Angle at Knock Onset and Knock Probability - KH knock model - Intake Pressure and SA sweep with CR=11.5 (C3)

							SA [de	g]						
		-48	-44	-40	-36	-32	-28	-24	-20	-16	-12	-8	-4	Ref
	Ref	-18.54	-16.80	-14.91	-12.70	-10.33	-7.61	-4.50	-0.97	3.50	9.71	_	_	-
	+10%	-18.80	-17.06	-15.08	-12.89	-10.39	-7.68	-4.55	-0.92	3.57	10.26	_	_	_
	+20%	-18.23	-16.50	-14.54	-12.35	-9.89	-7.09	-3.94	-0.20	4.56	12.78	_	1	-
	+30%	-17.47	-15.78	-13.82	-11.63	-9.13	-6.39	-3.15	0.69	5.90	18.49	_	_	_
	+40%	-16.62	-14.95	-13.03	-10.82	-8.40	-5.61	-2.29	1.72	7.61	_	_	_	_
	+50%	-15.71	-14.06	-12.22	-10.07	-7.61	-4.79	-1.37	2.85	9.83	-	_	1	-
급	+60%	-14.80	-13.19	-11.35	-9.23	-6.79	-3.92	-0.42	4.20	13.76	_	_	_	_
Pint [bar]	+70%	-13.84	-12.29	-10.44	-8.34	-5.89	-2.97	0.66	5.84	_	_	_	_	_
\int	+80%	-12.87	-11.33	-9.51	-7.40	-4.92	-1.91	1.98	8.15	-	-	_	-	-
1	+90%	-11.81	-10.27	-8.44	-6.31	-3.77	-0.60	3.72	12.81	_	_	_	_	-
	+100%	-10.51	-8.91	-7.05	-4.87	-2.19	1.28	6.58	_	_	-	_	1	-
	+110%	-8.30	-6.56	-4.51	-2.02	1.12	5.59	_	_	_	-	_	_	-
	+120%	2.61	5.17	8.43	15.95	_	_	-	_	_	-	_	_	-
	+130%	_	_	_	_	_	-	-	_		-	_	_	-
	+140%	_	_	_	_	_	_	-	_	_	_	_	_	_
	+150%	_	_	_	_	_	_	_	_	_	_	_	_	_

Table A.4.6: HCNG25 Crank Angle at Knock Onset and Knock Probability - KH knock model - Intake Pressure and SA sweep with CR=11.5 (C5)

							SA [de	g]						
		-48	-44	-40	-36	-32	-28	-24	-20	-16	-12	-8	-4	Ref
	Ref	-19.07	-17.39	-15.47	-13.32	-10.92	-8.19	-5.11	-1.52	2.79	8.99	_	_	_
	+10%	-19.40	-17.55	-15.69	-13.49	-10.95	-8.15	-5.07	-1.51	3.05	9.47	_	_	_
	+20%	-18.80	-17.10	-15.05	-12.89	-10.45	-7.66	-4.52	-0.77	3.97	11.66	_	_	-
	+30%	-18.00	-16.29	-14.37	-12.23	-9.79	-6.99	-3.78	0.10	5.08	14.95	_	_	_
	+40%	-17.22	-15.55	-13.63	-11.46	-9.06	-6.24	-2.97	0.97	6.46	_	_	_	_
	+50%	-16.32	-14.66	-12.82	-10.70	-8.25	-5.44	-2.11	2.05	8.30	_	_	_	_
=	+60%	-15.38	-13.77	-11.90	-9.78	-7.41	-4.53	-1.17	3.37	11.10	_	_	_	_
[bar]	+70%	-14.38	-12.89	-11.00	-8.96	-6.51	-3.65	-0.10	4.83	19.31	_	_	_	_
Pint	+80%	-13.42	-11.90	-10.09	-8.01	-5.60	-2.64	1.11	6.71	_	_	_	_	_
1	+90%	-12.37	-10.85	-9.09	-6.97	-4.51	-1.44	2.63	9.79	_	-	_	_	_
	+100%	-11.14	-9.57	-7.77	-5.61	-3.01	0.28	5.06	_	_	_	_	_	_
	+110%	-9.11	-7.41	-5.44	-3.05	-0.10	3.92	11.85	_	_	_	_	_	_
	+120%	-0.08	2.38	5.21	9.12	-	-	-	_	_	-	_	_	_
	+130%	_	_	_	_	_	_	_	_	_	_	_	_	_
	+140%	_	-	_	_	_	-	-	_	_	-	_	_	_
	+150%	_	_	_	_	_	-	_	_	_	-	_	_	_

Table A.4.7: HCNG15 Crank Angle at Knock Onset and Knock Probability - KH knock model - Intake Pressure and SA sweep with  $CR=11.5\ (C5)$